Overview of the Chemistry-Aerosol Mediterranean Experiment/Aerosol direct radiative forcing on the Mediterranean Climate (ChArMEx/ADRIMED) summer 2013 campaign

M. Mallet, F. Dulac, P. Formenti, P. Nabat, J. Sciare, G. Roberts, Jacques Pelon, Gérard Ancellet, D. Tanré, F. Parol, et al.

Atmos. Chem. Phys. Discuss., 15, 19615–19727, 2015
www.atmos-chem-phys-discuss.net/15/19615/2015/
doi:10.5194/acpd-15-19615-2015

Atmospheric Chemistry and Physics Discussions

Overview of the Chemistry-Aerosol Mediterranean Experiment/Aerosol Direct Radiative Forcing on the Mediterranean Climate (ChArMEx/ADRIMED) summer 2013 campaign

M. Mallet[1], F. Dulac[2], P. Formenti[3], P. Nabat[4], J. Sciare[2,5], G. Roberts[4], J. Pelon[6], G. Ancellet[6], D. Tanré[7], F. Parol[7], A. di Sarra[8], L. Alados[9], J. Arndt[10], F. Auriol[7], L. Blarel[7], T. Bourrianne[5], G. Brogniez[7], P. Chazette[2], S. Chevaillier[3], M. Claeys[5], B. D'Anna[11], C. Denjean[3,12], Y. Derimian[7], K. Desboeufs[3], T. Di Iorio[8], J.-F. Doussin[3], P. Durand[1], A. Féron[3], E. Freney[13], C. Gaimoz[3], P. Goloub[7], J. L. Gómez-Amo[8], M. J. Granados-Muñoz[9], N. Grand[3], E. Hamonou[2], I. Jankowiak[7], M. Jeannot[14], J.-F. Léon[1], M. Maillé[3], S. Mailler[15], D. Meloni[8], L. Menut[15], G. Momboisse[5], J. Nicolas[11], J. Podvin[7], V. Pont[1], G. Rea[15], J.-B. Renard[14], L. Roblou[1], K. Schepanski[12], A. Schwarzenboeck[13], K. Sellegri[13], M. Sicard[16], F. Solmon[17], S. Somot[5], B. Torres[7], J. Totems[1], S. Triquet[3], N. Verdier[18], C. Verwaerde[7], J. Wenger[10], and P. Zapf[3]

[1]Laboratoire d'Aérologie, Observatoire Midi-Pyrénées, 14 Avenue Edouard Belin, 31400 Toulouse, France
[2]LSCE-CEA/IPSL, CEA Saclay 701, 91191 Gif-sur-Yvette, France
[3]Laboratoire Inter-Universitaire des Systèmes Atmosphériques (LISA), UMR CNRS 7583, Université Paris Est Créteil et Université Paris Diderot, Institut Pierre Simon Laplace, Créteil, France
[4]Météo-France, CNRM-GAME, Centre national de recherches météorologiques, UMR3589, Toulouse, France
[5]The Cyprus Institute, Energy Environment and Water Research Center, Nicosia, Cyprus
[6]LATMOS-ISPL, UPMC Univ. Paris 06, Université Versailles St-Quentin, CNRS/INSU, Paris, France
[7]LOA, Université Lille 1, Villeneuve d'Ascq, France
[8]ENEA, Laboratory for Earth Observations and Analyses, Via Anguillarese 301, 00123 Roma, Italy
[9]Department of Applied Physic, University of Granada, 18071, Granada, Spain
[10]Department of Chemistry and Environmental Research Institute, University College Cork, Cork, Ireland
[11]Institute de recherches sur la catalyse et l'environnement de Lyon (IRCE Lyon), University of Lyon, 69100 Villeurbanne, France
[12]Leibniz Institute for Tropospheric Research (TROPOS), Permoserstraße 15, 04318 Leipzig, Germany
[13]Laboratoire de Météorologie Physique CNRS UMR6016, Observatoire de Physique du Globe de Clermont-Ferrand, Université Blaise Pascal, 63171 Aubière, France
[14]LPC2E-CNRS/Université d'Orléans, 3A avenue de la recherche scientifique, 45071 Orléans, France
[15]LMD, IPSL, CNRS, Ecole Polytechnique, École Normale Supérieure, Université Paris 6, UMR8539, 91128 Palaiseau CEDEX, France
[16]RSLab/IEEC-CRAE, Universitat Politècnica de Catalunya, Barcelona, Spain
[17]The Abdus Salam International Center for Theoretical Physics, Strada Costiera 11, 34100 Trieste, Italy
[18]Centre National d'Etudes Spatiales (CNES), DCT/BL/NB, 18 avenue Edouard Belin, 31401 Toulouse CEDEX 9, France

ACPD
15, 19615–19727, 2015

Received: 19 June 2015 – Accepted: 23 June 2015 – Published: 17 July 2015

Correspondence to: M. Mallet (malm@aero.obs-mip.fr)

Published by Copernicus Publications on behalf of the European Geosciences Union.

ACPD
15, 19615–19727, 2015

Abstract

The Chemistry-Aerosol Mediterranean Experiment (ChArMEx; http://charmex.lsce.ipsl.fr) is a collaborative research program federating international activities to investigate Mediterranean regional chemistry-climate interactions. A special observing period (SOP-1a) including intensive airborne measurements was performed in the framework of the Aerosol Direct Radiative Forcing on the Mediterranean Climate (ADRIMED) project during the Mediterranean dry season over the western and central Mediterranean basins, with a focus on aerosol-radiation measurements and their modeling. The SOP-1a took place from 11 June to 5 July 2013. Airborne measurements were made by both the ATR-42 and F-20 French research aircraft operated from Sardinia (Italy) and instrumented for in situ and remote-sensing measurements, respectively, and by sounding and drifting balloons, launched in Minorca. The experimental set-up also involved several ground-based measurement sites on islands including two ground-based reference stations in Corsica and Lampedusa and secondary monitoring sites in Minorca and Sicily. Additional measurements including lidar profiling were also performed on alert during aircraft operations at EARLINET/ACTRIS stations at Granada and Barcelona in Spain, and in southern Italy. Remote sensing aerosol products from satellites (MSG/SEVIRI, MODIS) and from the AERONET/PHOTONS network were also used. Dedicated meso-scale and regional modelling experiments were performed in relation to this observational effort. We provide here an overview of the different surface and aircraft observations deployed during the ChArMEx/ADRIMED period and of associated modeling studies together with an analysis of the synoptic conditions that determined the aerosol emission and transport. Meteorological conditions observed during this campaign (moderate temperatures and southern flows) were not favorable to produce high level of atmospheric pollutants nor intense biomass burning events in the region. However, numerous mineral dust plumes were observed during the campaign with main sources located in Morocco, Algeria and Tunisia, leading to aerosol optical depth (AOD) values ranging between 0.2 to 0.6 (at 440 nm) over the

ACPD
15, 19615–19727, 2015

western and central Mediterranean basins. Associated aerosol extinction values measured on-board the ATR-42 within the dust plume show local maxima reaching up to 150 Mm^{-1}. Non negligible aerosol extinction (about 50 Mm^{-1}) was also been observed within the Marine Boundary Layer (MBL). By combining ATR-42 extinction, absorption and scattering measurements, a complete optical closure has been made revealing excellent agreement with estimated optical properties. Associated calculations of the dust single scattering albedo (SSA) have been conducted, which show a moderate variability (from 0.90 to 1.00 at 530 nm). In parallel, active remote-sensing observations from the surface and onboard the F-20 aircraft suggest a complex vertical structure of particles and distinct aerosol layers with sea-salt and pollution located within the MBL, and mineral dust and/or aged north American smoke particles located above (up to 6–7 km in altitude). Aircraft and balloon-borne observations show particle size distributions characterized by large aerosols (> 10 µm in diameter) within dust plumes. In terms of shortwave (SW) direct forcing, in-situ surface and aircraft observations have been merged and used as inputs in 1-D radiative transfer codes for calculating the direct radiative forcing (DRF). Results show significant surface SW instantaneous forcing (up to $-90\,W\,m^{-2}$ at noon). Associated 3-D modeling studies from regional climate (RCM) and chemistry transport (CTM) models indicate a relatively good agreement for simulated AOD compared with measurements/observations from the AERONET/PHOTONS network and satellite data, especially for long-range dust transport. Calculations of the 3-D SW (clear-sky) surface DRF indicate an average of about -10 to $-20\,W\,m^{-2}$ (for the whole period) over the Mediterranean Sea together with maxima ($-50\,W\,m^{-2}$) over northern Africa. The top of the atmosphere (TOA) DRF is shown to be highly variable within the domain, due to moderate absorbing properties of dust and changes in the surface albedo. Indeed, 3-D simulations indicate negative forcing over the Mediterranean Sea and Europe and positive forcing over northern Africa.

ACPD
15, 19615–19727, 2015

1 Introduction

The Mediterranean region has been identified as one of the most prominent "Hot-Spots" in future climate change projections (Giorgi and Lionello, 2008). It is characterized by its vulnerability to changes in the water cycle (e.g. Chenoweth et al., 2011; García-Ruiz et al., 2011). General Circulation Model (GCM) and Regional Climate Model (RCM) simulations show a substantial precipitation decrease and a warming of the region, especially in the long warm and dry Mediterranean season. At the end of 21st century, the average of the model outputs predicts a significant loss of freshwater (+40 % for the period 2070–2090 compared to 1950–1999; Sanchez-Gomez et al., 2009) over the Mediterranean region. More recently, Mariotti et al. (2015) have used the newly available Coupled Model Intercomparison Project-Phase 5 (CMIP5) experiments and show a significant increase of the projected surface air temperature (by ∼ +2–3 °C) for the 2071–2098 period compared to 1980–2005. These results need to be put in the context of an increasing anthropogenic pressure on the Mediterranean region, with an expected doubling of the population in countries around the Mediterranean basin in the next decades, with a contrast between a small decrease in European countries and a strong increase in African and Middle-East countries (Brauch, 2003). However, as highlighted by Mariotti et al. (2008), despite the high degree of model consistency, the results concerning the future climate projections for the Mediterranean Sea water budget from the global coupled models are still uncertain due to their horizontal spatial resolutions that are not capable of resolving the local to regional Mediterranean specific processes (air–sea exchanges, coastline, topography, north–south gradient of albedo). Indeed, the Mediterranean climate is affected by local processes induced by the complex physiography of the region and the presence of a large body of water (the Mediterranean Sea). For example, the Alpine chain is a strong factor in modifying traveling synoptic and mesoscale systems and the Mediterranean Sea is an important source of moisture and precipitation in the region (Gimeno et al., 2010; Schicker et al., 2010) and of energy for storms (Lionello et al., 2006). The complex topography, coast-

ACPD
15, 19615–19727, 2015

line and vegetation cover of the region are well known to modulate the regional climate signal at small spatial scales (e.g. Millan et al., 1997; Gangoiti et al., 2001; Lionello et al., 2006).

So far, most global and regional climate simulations have investigated the impact of global warming on the Mediterranean climate without detailed considerations of the possible radiative influence and climatic feedback from the different Mediterranean aerosols (anthropogenic, marine, biomass burning, secondary biogenic and mineral dust particles). The Mediterranean region is rich in a variety of particles (natural and anthropogenic) from both continental and marine sources (Lelieveld et al., 2002). In Fig. 1, we illustrate the significant differences in aerosol loading between the eastern, central, and western sub-basins and between the North and the South of the Mediterranean shown by long-term aerosol satellite products. The aerosol optical depth (AOD), which represents the integration of the extinction by particles along the whole atmospheric column displays annual mean values (Fig. 1) from 0.2 to 0.5 (in the visible wavelengths), depending on the aerosol types observed over the Euro-Mediterranean region (Nabat et al., 2013).

Numerous studies have documented the AOD for polluted-anthropogenic Mediterranean aerosols at local scale over southeastern France (Mallet et al., 2006; Roger et al., 2006), Spain (Horvath et al., 2002; Alados-Arboledas et al., 2008), Greece (Chazette and Liousse, 2001; Gerasopoulos et al., 2003), Crete (Fotiadi et al., 2006), and Italy (Tafuro et al., 2007; Ciardini et al., 2012). Under polluted conditions, they report moderate AOD values ranging between 0.1 to 0.5 (at visible wavelengths). In parallel, multi-year TOMS and MODIS observations over the eastern Mediterranean (Hatzianastassiou et al., 2009) or the Po Valley (Royer et al., 2010) indicate the occurrence of high AOD values (up to more than 0.8 at 500 nm) over large urban areas surrounding megacities.

Up to now and contrarily to anthropogenic polluted aerosols, only few studies have been dedicated to biomass burning aerosols over the Mediterranean, which are mainly observed in July and August (driest months of the year) when the development of forest

ACPD
15, 19615–19727, 2015

fires is favoured (Pace et al., 2005). Long term observations of absorbing aerosols have clearly shown the major role of long range transport of biomass (agriculture waste) burning in the eastern Mediterranean (Sciare et al., 2008). At the present time, AOD data available for smoke particles show "intermediate" values between those observed for dust and anthropogenic particles. For example, AOD ranging between 0.3 and 0.8 (Pace et al., 2005) have been observed at Lampedusa from 05 to 22 August 2003, in relation with intense fires developed in southern Europe and transported over the Mediterranean basin during a regional heat wave. In addition, the STAAARTE-MED experiment (August 1998 in the Eastern Mediterranean) has also documented a mean AOD of 0.39 (at 550 nm) for aged smoke plume from Canadian fires (Formenti et al., 2002).

Concerning natural aerosols, different cases of Saharan mineral dust have been regularly documented with local optical measurements on the island of Lampedusa by Meloni et al. (2003, 2004), who indicate moderate AOD (at 415.6 nm) of about 0.23–0.26 and one significantly larger event with AOD values of 0.51. Meloni et al. (2008) also report AOD (at 500 nm) measurements ranging between 0.29 and 1.18 for the 1999 to 2006 period. For some extreme cases, dust AOD peaks may be even larger reaching values up to 2 as observed by di Sarra et al. (2011). In parallel to Lampedusa observations, Kubilay et al. (2003) have also documented three dust intrusion events at Erdemli (Turkish coast), occurring in spring from central Sahara, in summer from eastern Sahara, and in autumn from the Middle East/Arabian peninsula. In each case, the presence of dust particles significantly increased the AOD, up to 1.8.

For sea-salt particles, which are the second main natural species observed over the Mediterranean, Nabat et al. (2013) report a relatively low monthly mean AOD derived from satellites and modeling data, with values lower than 0.05 (in the visible wavelengths). By using recent improvements in the sea-salt emission scheme, Spada et al. (2013) show an averaged sea-salt AOD around 0.04 for the month of January (5 year period, 2002–2006) which is the favourable period for generating primary sea-salt due to strong sea-surface winds. Finally, and in the case of extreme wind episodes

ACPD
15, 19615–19727, 2015

occurring over the western basin, Salameh et al. (2007) show that the amount of aerosol loading, solely due to the Mistral, Tramontane and Ligurian outflows, is as large as 3–4 times the background aerosol amount. They indicate that the contribution of sea-salt particles to the total aerosol loading and optical depth ranges from 1 to 10 %. Salameh et al. (2007) report AOD around 0.15–0.20 (at 865 nm) within the sea-salt aerosol plume during such strong wind events. In addition, Mulcahy et al. (2008) reported a high correlation between AOD and wind-speed with AOD values of 0.3–0.4 at moderately-high wind speed.

Such atmospheric aerosol loadings are known (Nabat et al., 2012; Papadimas et al., 2012; Zanis et al., 2012) to significantly change the radiative budget of the Mediterranean region by (1) decreasing the sea-surface incoming shortwave radiations, (2) increasing/decreasing outgoing shortwave fluxes depending on the surface albedo and (3) possibly heating turbid atmospheric layers when particles absorb solar light. This is the so-called aerosol "Direct Radiative Forcing (DRF)". As for the AOD, many of the aerosol DRF calculations are now referenced over the Mediterranean clearly showing that the DRF is significantly larger at daily time scales than the one exerted by the additional anthropogenic greenhouse gases.

Concerning polluted aerosols, shortwave DRF have been estimated by many authors (Horvath et al., 2002; Markowicz et al., 2002; D. Meloni et al., 2003, 2015; Roger et al., 2006; Mallet et al., 2006; Saha et al., 2008; di Sarra et al., 2008; Di Biagio et al., 2009, 2010; di Sarra et al., 2011). Studies show significant decreases of surface solar fluxes of about 20–30 $W m^{-2}$ (daily mean) for different locations as Almeria (South Mediterranean coast of Spain), Finokalia (Crete Island), Lampedusa, Marseilles and Toulon (south-eastern France). In parallel, the combination of surface and satellite remote-sensing observations performed at Lampedusa have been used to perform calculations of the DRF, both in the shortwave (SW; Di Biagio et al., 2010) and longwave (LW; di Sarra et al., 2011; D. Meloni et al., 2015) spectral regions for different cases of Saharan dust intrusions. These studies emphasize that the radiative effect of desert dust in the LW spectral range is significant, and offsets a large fraction of

ACPD
15, 19615–19727, 2015

the SW forcing (di Sarra et al., 2011; D. Meloni et al., 2015). More recently, Sicard et al. (2014a, b) have also produced estimations of the dust LW radiative effect, based on remote-sensing observations in Barcelona and 1-D radiative transfer calculations.

Concerning the smoke DRF, only few studies are available over the Mediterranean region. One estimate is proposed by Formenti et al. (2002) for an aged Canadian biomass-burning plume and reveals a significant SW surface dimming of about $\sim 60\,W\,m^{-2}$. In addition, the DRF induced by smoke aerosols at Lampedusa between 03 and 23 August 2003, during the exceptionally hot and dry season, was derived by Pace et al. (2005) for the 300–800 nm spectral range. The smoke atmospheric forcing was estimated to be between +22 and $+26\,W\,m^{-2}$, with a corresponding SW heating rate possibly exceeding $2\,K\,day^{-1}$ at the smoke plume altitude.

At the regional scale, Papadimas et al. (2012) have proposed a recent estimation of the aerosol DRF using MODIS data from 2000 to 2007 for both all-sky and clear-sky conditions. They derived a multi-year regional mean surface of $-19\,W\,m^{-2}$, associated with a TOA DRF of $-4.5\,W\,m^{-2}$. Regional modelling studies have been also recently proposed by Nabat et al. (2012, 2015) using the coupled-chemistry RegCM and the CNRM-Regional Climate System Model (RCSM) models for multi-year simulations. These works reported a mean regional surface (TOA) forcing of about $-12\,W\,m^{-2}$ ($-2.4\,W\,m^{-2}$) and $-16\,W\,m^{-2}$ ($-5.7\,W\,m^{-2}$) for the RegCM and CNRM-RCSM models, respectively. RegCM has been also used to investigate direct and semi-direct radiative effects of mineral dust over the Sahara and Europe in a test case of July 2003 (Santese et al., 2010). In this work, Santese et al. (2010) computed a daily-mean SW DRF of $-24\,W\,m^{-2}$ (resp. $-3.4\,W\,m^{-2}$) on 17 July and $-25\,W\,m^{-2}$ ($-3.5\,W\,m^{-2}$) on 24 July at the surface (TOA) on average over the simulation domain. Zanis et al. (2012) also proposed a regional estimate of the DRF of anthropogenic particles over the 1996–2007 period using RegCM and showed a significant forcing of up to $-23\,W\,m^{-2}$ at TOA over Eastern Europe. In addition, Pere et al. (2011) have used the CTM-CHIMERE model coupled to the WRF model, for estimating the DRF of anthropogenic particles during the heat wave of summer 2003 and showed significant effects with implications on the

ACPD
15, 19615–19727, 2015

planetary boundary layer height (decrease up to 30 % in the presence of anthropogenic aerosols) and local air-quality. In addition to their important effects on the surface and TOA DRF, most of the Mediterranean aerosols are also able to absorb more or less effectively the solar radiations leading to a significant atmospheric forcing and associated SW heating rate. Local studies previously mentioned (Roger et al., 2006; Saha et al., 2008; Pace et al., 2005; Pere et al., 2011; D. Meloni et al., 2015) clearly report significant SW heating rate due to absorbing particles with values reaching up to 2–3 K day^{-1}, depending on the aerosol types. Finally, aerosols also have a significant effect on photolysis rates that may affect tropospheric chemistry and ozone production over the basin (Casasanta et al., 2011; Mailler et al., 2015).

In regards to such surface, TOA and atmospheric forcings, there is a need to investigate how the change in the radiative budget due to natural/anthropogenic aerosols influence the surface temperature (both over land and sea), relative humidity profiles, exchanges (latent heat fluxes) between ocean and atmosphere, cloud-cover (semi-direct effect of absorbing particles), precipitation and finally the whole Mediterranean hydrological cycle. The induced perturbations in the sea surface–atmosphere fluxes is expected to be important despite the relatively small size of the Mediterranean Sea, since this basin plays an important role at much larger scale by providing moisture for precipitation to its surroundings land region extending to northern Europe and northern Africa (Gimeno et al., 2010 and Schicker et al., 2010). Indeed and as shown by Ramanathan et al. (2001) for the Indian region or Foltz and McPhaden (2008) and Yue et al. (2011) for the Atlantic Ocean, a modification of the sea-surface evaporative fluxes, due to the dimming radiative effect of aerosols at the sea surface could significantly influence the lower troposphere moisture content and the associated precipitation distribution around the Mediterranean. In parallel, the absorbing particles over the Mediterranean (Mallet et al., 2013) could exert a semi-direct effect that could modify the vertical profiles of relative humidity and cloud cover, which has to be quantified. In that context, the main objectives of the ChArMEx/ADRIMED project were the following:

ACPD
15, 19615–19727, 2015

- to conduct an experimental campaign, based on surface and aircraft observations, for creating an innovative database gathering the physical, chemical, optical properties as well as the vertical distribution of the main Mediterranean aerosols
- to use experimental surface and aircraft observations to estimate the 1-D-local DRF and forcing efficiency of different aerosols at the surface, TOA and within the atmospheric layer
- to investigate how the modifications of the radiative budget due to aerosols affect the sea-surface evaporation fluxes, relative humidity profiles, cloud-cover, precipitation and more largely the Mediterranean hydrological cycle.

The rest of this article is divided into six different parts. In the first and second part (Sects. 2 and 3), we describe the in-situ and remote-sensing instrumentation deployed at the two super sites (Ersa and Lampedusa) and secondary sites (Minorca, Barcelona, Granada, Capo Granitola), the additional AERONET/PHOTONS (AErosol RObotic NETwork/PHOtométrie pour le Traitement Opérationnel de Normalisation Satellitaire, http://aeronet.gsfc.nasa.gov/; Holben et al., 1998) and EARLINET/ACTRIS (European Aerosol Research Lidar Network/Aerosols, Clouds, and Trace gases Research InfraStructure Network, http://www.actris.net/; Pappalardo et al., 2014) network stations that we used, and the airborne observations obtained onboard the two French research aircraft (ATR-42 and F-20) and with sounding and drifting balloons. The Sect. 4 is dedicated to present the main meteorological conditions, cloud cover and precipitation, which controlled the aerosol emission and transport during the period of observations. The Sect. 5 presents some examples of results concerning the in-situ and remote-sensing observations, in terms of aerosol physical, chemical, optical properties, and vertical profiles, as well as 1-D DRF SW and LW calculations. In the last part (Sect. 6), the modelling effort is presented. Different models are involved in this project, from high resolution meteorological and chemistry transport models to regional climate models. The modelling results are used to describe the anthropogenic (carbonaceous, secondary inorganic and organic species) and natural (dust and sea-salt) loading and

ACPD
15, 19615–19727, 2015

the estimated DRF at the regional scale for the period of experiment. Longer (inter-seasonal and inter-annual) aerosol-climate simulations are not described here and can be found in Nabat et al. (2012, 2014, 2015a).

2 Overview of the surface observation network

The regional experimental set-up deployed in the western and central Mediterranean during the campaign ChArMEx SOP-1a is shown in Fig. 2.

2.1 The Cape Corsica and Lampedusa surface super sites

Two super-sites were fully equipped for documenting the aerosol chemical, physical and optical properties as well as their possible mixing and their vertical structure at local scale (Table 1). The main characteristics of these two surface stations are presented here. The first station was located in Ersa on Cape Corsica (42°58′10″ N, 09°22′49″ E), near the North tip of Corsica Island. This station was primarily instrumented for investigating polluted air masses transported over the Mediterranean basin from the highly industrialized regions of the Po Valley (Royer et al., 2010) and/or the Marseille-Fos-Berre (Cachier et al., 2005) zone and Rhone Valley. This ground-based remote station is located at an altitude of about 530 m above mean sea level (a.m.s.l.) on a ridge equipped with wind mills and benefit from a direct view to the sea over a North sector of ∼ 270° extending from the SW to SE. The Cape Corsica peninsula is a remote site excluding important local anthropogenic sources that could affect the in-situ measurements.

The Lampedusa super-site (35°31′5″ N, 12°37′51″ E) was established at the "Roberto Sarao" station permanently operated by ENEA in the small island of Lampedusa (∼ 20 km^2), and it was augmented during the field campaign by the observations of the PortablE Gas and Aerosol Sampling UnitS (PEGASUS) mobile station operated by LISA. This surface station was mainly used for documenting very aged air masses

ACPD
15, 19615–19727, 2015

in south westerly flow from Europe, southern air masses from northern Africa (Tunisia, Algeria and Libya) possibly laden with mineral dust, as well as marine aerosols. It is situated on a cliff at about 45 m a.m.s.l. on the NE tip of the island.

The complete instrumentation deployed during the SOP-1a experiment for both super-sites is detailed in Table 1. Briefly, it served to determine the complete aerosol physical, chemical and optical properties as well as vertical profiles, and to measure radiative fluxes (broadband SW and LW, and spectral SW).

2.1.1 In situ measurements at super-sites

Both super-sites measured the mass concentration online using Tapered Element Oscillating Microbalance (TEOM) analysers. The number size distribution of particles are also measured, including fine and coarse fractions (radius ranges and corresponding instruments are reported Table 1). The aerosol composition was derived from chemical analyses of filters and cascade impactors (DEKATI and MOUDI) with time resolution varying from 12 to 48 h (depending on the aerosol load), but also from high-time resolution online measurements by an ACSM (Aerosol Chemical Speciation Monitor) at Ersa, a C-TOF-AMS (Time of Flight Aerosol Mass Spectrometer) at Lampedusa, and two PILS (Particle Into Liquid Sampler) systems at both sites (Table 1). Concerning aerosol optical properties, scattering and absorption coefficients (at wavelengths listed in Table 1) have been estimated for both super-sites using a 3λ nephelometer and a 7λ aethalometer, respectively. At Ersa station, the extinction coefficient (at 870 nm) was also estimated using a Photoacoustic Extinctiometer (PAX) instrument, while it has been estimated at 2λ (450 and 630 nm) at Lampedusa using 2 Cavity Attenuated Phase Shift Spectroscopy (CAPS) systems.

Additional in-situ measurements were performed at the Ersa station. The mixing state of fine particles (at the two selected diameters of 50 and 110 nm in dry conditions) has also been estimated from their hygroscopic behaviour using a VHTDMA (volatilization and humidification tandem differential mobility analyser) system (Johnson et al., 2004). In parallel, a TSI (model 3800) aerosol time of flight mass Spectrom-

ACPD
15, 19615–19727, 2015

eter (ATOFMS) (Gard et al., 1997) was used to measure the size-resolved chemical composition of single particles in the vacuum aerodynamic diameter (d_{va}) size range 100–3000 nm.

2.1.2 Remote sensing and radiation measurements at super-sites

A Leosphere Raman lidar model RMAN510 was setup at low altitude (~ 11 m a.s.l.) in the small village of Macinaggio (42°57′44″ N, 9°26′35″ E) located on the eastern coast of Cape Corsica. The lidar was operated at about 6 km East from the Ersa station and less than 700 m from the shoreline. The RMAN510 uses a laser emitting at 355 nm. It measures the total and polarized backscatter at 355 nm and the Raman nitrogen signal at 387 nm at night-time. A second ALS300 510 lidar system has been deployed in Lampedusa (Formenti et al., 2015) as well as a more powerful University of Rome-ENEA homemade lidar measuring backscatter at 532 and 1064 nm (Di Iorio et al., 2015). The main characteristics of lidar systems are provided and detailed in Table 1.

At each station, a multi-wavelength sun-photometer from the AERONET/PHOTONS network was operated, allowing the operational retrieval of column integrated AOD at 340, 380, 440, 500, 675, 870, 1020 nm (and also at 1650 nm at Ersa) and aerosols optical and microphysical properties such as the single scattering albedo, refractive index and particle size volume distribution (Dubovik and King, 2000; Dubovik et al., 2000, 2002, 2006). The Ersa sun-photometer is positioned since June 2008 near the navy semaphore on the northwestern tip of Cape Corsica (43°00′13″ N, 09°21′33″ E, alt. ~ 75 m a.m.s.l.) at about 4.2 km NNW of the Ersa surface station.

Both super-sites were complemented by a pyrgeometer and a pyranometer for monitoring longwave and shortwave downward fluxes measurements, respectively. Additional radiation measurements were performed at Lampedusa (Table 1). Spectral measurements of global, diffuse, and direct radiation were carried out with other instruments deployed by ENEA and the Physikalisch-Meteorologisches Observatorium Davos, World Radiation Center, (PMOD/WRC, Switzerland). Multi-filter rotating shadowband radiometer observations were carried out jointly with AERONET sun-

ACPD
15, 19615–19727, 2015

photometer (di Sarra et al., 2015) and allowed the derivation of the AOD at several wavelengths. By combining these two measurements, a long-term series of AOD, started in 2001, was obtained. Measurements of the spectral actinic flux, allowing the determination of the photolysis rates (Mailler et al., 2015), were carried out with a diode array spectrometer. Measurements of broadband irradiance included a CG3 pyrgeometer sensitive to radiation in the atmospheric infrared window. Finally, the total ozone and spectral UV irradiance were obtained with a Brewer spectrophotometer. Several radiosondes were also launched from Lampedusa during the SOP-1a, and vertical profiles of temperature and humidity were continuously measured by a microwave radiometer.

2.2 The secondary sites

2.2.1 Montesoro station

The Cape Corsica station was complemented by an additional remote-sensing setup at the peri-urban air quality station of Montesoro, southward of Bastia at about 45 m a.m.s.l. (Leon et al., 2015), including a Leosphere model EZ lidar operating at 355 nm (42°40′17″ N, 09°26′05″ E) and a Cimel AERONET/PHOTONS sun-photometer (42°40′19″ N, 09°26′06″ E). In addition, some air-quality parameters were monitored by Qualitair Corse, including $PM_{2.5}$ and PM_{10}. This station is less than 1 km far from the shore on the northeastern coast of Corsica, about 32 km South of Macinaggio.

2.2.2 Barcelona station

The Barcelona station (41.39° N, 2.11° E, 115 m a.m.s.l.) was equipped with the following fixed instruments including an AERONET sun-photometer, an automated Sigma Space-NASA Micro Pulse Lidar (MPL) and a Universitat Politècnica de Catalunya (UPC) home-made multi-wavelength lidar (Kumar et al., 2011). The MPL lidar works

ACPD
15, 19615–19727, 2015

at 532 nm and has a depolarization channel, while the UPC lidar works at 355, 532 and 1064 nm, and also includes two N_2- (at 387 and 607 nm) and one H_2O-Raman (at 407 nm) channels. The MPL system worked continuously. The UPC system was operated on alert in coordination with the two research aircraft plans involved in the SOP-1a campaign. The UPC system is part of the EARLINET network.

2.2.3 Minorca station

An additional station was setup during the campaign, located at Cap d'en Font, on the southeastern coast of the Balearic island of Minorca (Spain, 39°53′12″ N and 4°15′31″ E, ∼ 10 m a.m.s.l.), which is relatively central in the western Mediterranean basin. The Mobile Aerosol Station (MAS) of the LSCE (Laboratoire des Sciences du Climat et de l'Environnement) laboratory was equipped with the new Raman lidar WALI (Chazette et al., 2014a, b), an AERONET/PHOTONS sun-photometer, and a set of in-situ instruments. A 5-wavelength Solar Light Microtops-II manual sun-photometer was also used. The WALI instrument, its calibration and the associated errors are documented in Chazette et al. (2014a). During all the experiment, the acquisition was performed continuously with a vertical resolution of 15 m. AOD at the lidar wavelength of 355 nm has been extrapolated from that measured by sun-photometer at 380 and 440 nm using the Angström exponent (Chazette et al., 2015).

The in-situ instruments installed on-board the MAS included a 3-wavelength TSI nephelometer, a Magee Scientific Model AE31 7-wavelength aethalometer, a TEOM microbalance, and a Vaisala meteorological probe type PTU300. The nephelometer was sampling through a PM_{10} inlet to measure the aerosol scattering coefficient at 3 wavelengths (450, 550 and 700 nm) with an integrating time step of 5 min. The aethalometer was sampling through a $PM_{2.5}$ inlet to measure aerosol absorption (at 7 wavelengths) and derive a 5 min average black carbon concentration. The TEOM measured dry PM_{10} concentration every 30 min. In addition two optical particle counters (OPCs) were installed outdoors next to the sun-photometer on a mobile platform. A MetOne HHPC-6 and a LOAC (Renard et al., 2015a, b) respectively measured

ACPD
15, 19615–19727, 2015

aerosol particle number concentration in 6 channels above 0.3 µm in diameter and in 19 channels above 0.2 µm. The LOAC instrument accuracy is discussed in detail by Renard et al. (2015a, b).

2.2.4 Granada station

The station of the Atmospheric Physics Group (GFAT) is located in the Andalusian Institute for Earth System Research (IISTA-CEAMA), in Granada, Spain (37.16° N, 3.61° W, 680 m a.m.s.l.). The station is at a relatively short distance, about 200 km away, from the African continent and approximately 50 km away from the western Mediterranean Sea. During the SOP-1a campaign, lidar measurements were performed simultaneously with a multiwavelength Raman lidar and a scanning Raman lidar both from Raymetrics S.A. The multi-wavelength Raman system is part of the EARLINET network. In addition, a ceilometer was operated. Column integrated characterization of the atmospheric aerosol was performed following AERONET protocols with two Cimel sun-photometers deployed at two different heights: Granada (680 m a.s.l.) and Cerro Poyos (37°6′32″ N, 03°29′14″ W, 1790 m a.s.l.) stations. In addition, in-situ instrumentation was continuously operated providing measurements of aerosol light-absorption coefficient at multiple wavelengths (multi-angle absorption photometer (MAAP) from Thermo ESM Andersen Instruments and Aethalometer model AE31), size distribution and particle number concentration for diameters larger than 0.5 µm (TSI aerodynamic particle sizer APS model 3321) and light-scattering and backscattering coefficient at dry and at relative humidity of 85 % by means of a TSI tandem nephelometer humidograph system. Furthermore, the chemical composition in the PM_1 and PM_{10} size fractions was determined during 16 and 17 June by collecting aerosol samples using two high-volume samplers.

ACPD
15, 19615–19727, 2015

2.2.5 Capo Granitola station

Several instruments were also deployed at Capo Granitola (37°34′ N, 12°40′ E), a site along the Southern coast of Sicily. The site, within a combined effort of ENEA, Univ. of Florence, and Univ. of Valencia, was equipped with a PM_{10} sampler, a MultiFilter Rotating Shadowband Radiometer (MFRSR) to derive spectral AOD, and radiometers and spectrometers for the measurement of global, direct, and diffuse radiation throughout the SW and LW spectral ranges.

2.3 Surface remote-sensing network

Two surface remote-sensing networks were operated during the ChArMEx SOP-1a experiment, namely the AERONET/PHOTONS and EARLINET/ACTRIS (Pappalardo et al., 2014) networks. These networks were highly useful as they allow estimating the column-integrated aerosol loading as well as the vertical structure of particles.

2.3.1 The AERONET/PHOTONS Sun-Photometer Network

AERONET (Aerosol Robotic Network; http://aeronet.gsfc.nasa.gov/) is a federated network of ground-based sun-photometers and the associated data inversion and archive system, that routinely performs direct sun observations about every 15 min during daytime, and both almucantar and principal plane sky radiance measurements, at selected solar angles (Holben et al., 1998). Along with AOD observations, the AERONET aerosol retrieval algorithm (Dubovik and King, 2000) delivers the complete set of column-effective aerosol microphysical parameters, including volume size distribution, refractive index at several wavelengths and fraction of spherical particles (Dubovik et al., 2006, see also description in Dubovik et al., 2011). In addition, using these microphysical parameters, the algorithm provides other column-effective aerosol optical properties such as wavelength dependent SSA, phase function, and asymmetry parameter, as well as integral parameters of bi-modal particle size distributions (concen-

ACPD
15, 19615–19727, 2015

tration, mode radii and variances) (Dubovik et al., 2002). The accuracy of AERONET retrievals is evaluated and discussed by Dubovik et al. (2000, 2002). In addition to microphysical and optical aerosol properties, we also have used direct radiative forcing calculations operationally provided at any AERONET location as an operational product of the network. The method of derivation is described in detail by Garcia et al. (2012). Briefly, the broadband fluxes were calculated using the radiative transfer model GAME (Dubuisson et al., 2004; Roger at al., 2006) that has been integrated into operational AERONET inversion code. Sun-photometer stations deployed during the SOP-1a campaign over the Western basin are listed in the Table 2.

2.3.2 The EARLINET/ACTRIS network

Between 22 and 24 June, four ACTRIS/EARLINET lidar stations located in Italy, in addition to the EARLINET stations of Barcelona and Granada, were operated in support of aircraft operations (Sicard et al., 2015):

- Naples (40.84° N, 14.18° E, 118 m a.m.s.l.); measurements of backscatter profiles at 355 and 532 nm, as well as depolarization ratio profiles at 532 nm, on 22 June 2013.
- Serra La Nave (Sicily, 37.68° N, 14.98° E, 1735 m a.m.s.l.); measurements of backscatter profiles at 355 nm, as well as depolarization ratio profiles at 355 nm, on 22 June 2013.
- Potenza (40.60° N, 15.72° E, 760 m a.m.s.l.); measurements of extinction profiles at 355 and 532 nm, backscatter profiles at 1064 nm, as well as depolarization ratio profiles at 532 nm (Madonna et al., 2011), on 22 and 23 June 2013.
- Lecce (40.30° N, 18.10° E, 30 m a.m.s.l.); measurements of extinction profiles at 355 and 532 nm, backscatter profiles at 1064 nm, water vapour profiles, as well as depolarization ratio profiles at 355 nm, on 22 and 24 June 2013.

ACPD
15, 19615–19727, 2015

3 Overview of the aircraft and balloon operations

3.1 Overview of the ATR-42 and F-20 flights

Figure 3 summarizes ATR-42 and F-20 flights trajectories performed during the experiment and their main characteristics. Most of the western Mediterranean basin has been investigated during the campaign by both aircrafts, excluding areas under the control of African aviation authorities where authorizations for scientific operations are very difficult to obtain. The first period of the campaign (16 to 20 June) was mainly dedicated to ATR-42 flights over Spain and Minorca islands (16–17 June, flights 29–32) and Southern France–Corsica Island (19–20 June, flights 33–34). During the second period (21–28 June) of the SOP-1a, ATR-42 flights have been mostly conducted over the Sardinia–Sicily–Lampedusa region in the central Mediterranean (flights 35–40). In July, two ATR-42 flights (41 and 42) were conducted over Lampedusa on 2–3 July and two others (43 and 44) on 4 July over the Gulf of Genoa. It should be noted that most ATR-42 flights included some transects at fixed altitudes (generally ~ 30 min of duration) associated with vertical profiles over surface super-sites and secondary stations. Details about each flight track are available on the ChArMEx Operation Centre website (ChOC; http://choc.sedoo.fr). On Fig. 3, F-20 flights trajectories are also indicated with the day corresponding to each flight. Except for the 16 and 17 June when F-20 is not flying, most of flights have been made jointly between the two aircraft. The longer flight range of the F-20 allowed us to document the Tyrrhenian Sea (not covered by the ATR-42) and to perform vertical profiles of aerosols over Southern Italy in association with EARLINET/ACTRIS lidar observations. It should be finally noted the additional F-20 flight between Sardinia and Spain on 27 June specifically dedicated to sample a forest fire plume transported long-range from North America.

ACPD
15, 19615–19727, 2015

3.2 In-situ and remote sensing observations on board the ATR-42

The instrumentation deployed onboard the ATR-42, described in detail in Denjean et al. (2015) and Nicolas et al. (2015) is summarized in Table 3. It is analogous to the one used for the two super-sites and was devoted to the characterization of microphysical, chemical and optical properties of aerosols that have been advected above the MBL and so not detectable at the surface. As indicated in Table 3, the number size distribution of aerosols, including fine and coarse fractions, as well as the total concentration of particles have been evaluated using SMPS, GRIMM, FSSP and UHSAS systems. The corresponding size ranges for all instruments are indicated in Table 3. A 3λ nephelometer and 1λ Cavity Attenuated Phase Shift (CAPS PMex) particle light extinction monitor system (Petzold et al., 2013) have been used conjointly for estimating scattering and extinction properties of particles. The CAPS-PMex system, used for the first time onboard the ATR-42, provides an additional constrain on the aerosol optical properties, useful to determine the absorbing properties. Indeed, the aerosol absorbing characterization remains largely challenging using filter techniques (Moonsmuller et al., 2012). These optical inter-comparisons have been performed for different aerosol plumes and are presented in Denjean et al. (2015).

In addition, passive remote-sensing observations have been conducted during the SOP-1a experiment using the PLASMA (Photomètre Léger Aéroporté pour la Surveillance des Masses d'Air) system, which is an airborne sun-tracking photometer with two main characteristics: lightness and a wide spectral coverage (15 channels between 0.34–2.25 µm; see Karol et al., 2013). The instrument contains also a microprocessor which derives the Sun position depending on time, latitude, longitude (provided by a GPS system) and the rotation of the airborne (provided by a gyroscope). Spectral AOD is derived from these direct sun measurements and the calibration coefficients. During the campaign, several AOD comparisons were done between PLASMA and AERONET/PHOTONS sun-photometers (Cagliari, Lampedusa, Granada) showing differences within 0.01 at all wavelengths. Moreover, as a consequence of performing

ACPD
15, 19615–19727, 2015

AOD measurements at different heights, the aerosol extinction vertical profiles have been also obtained during every landing/taking off and during pre-scheduled vertical profiles (Torres et al., 2015). Finally, upward and downward radiative fluxes (SW & LW) have been measured onboard the ATR-42 by means of CMP22 and CGR4 radiometers calibrated before the campaign.

3.3 Remote-sensing observations on board the F-20

3.3.1 LNG observations

The LEANDRE Nouvelle Generation (LNG) was used in its backscatter configuration during the ChArMEx-ADRIMED field operation onboard the SAFIRE F-20 aircraft. In the present campaign, the LNG system involved three elastic channels at 1064, 532 and 355 nm. Depolarization was also measured in a fourth channel operating at 355 nm. The profiles of atmospheric particulate extinction and backscatter coefficients are retrieved after different steps as detailed by Pelon et al. (2015). Zenith pointing lidar measurements were taken before most of the flights from the ground at the Cagliari airport (39.25° N, 9.06° E) in Italy. Lidar observations allow the detection of biomass burning plumes (BBP) (see Sect. 4.3) arriving at the Cagliari airport on 28 June as described by Pelon et al. (2015).

3.3.2 OSIRIS observations

OSIRIS (Observing System Including PolaRisation in the Solar Infrared Spectrum) is an instrument devoted to observation of the polarization and directionality of the solar radiation reflected by the surface–atmosphere system. OSIRIS is based on the same imaging radiometer concept as the POLDER instrument (Deschamps et al., 1994). It includes two optical systems: one for the visible and near infrared range (VIS-NIR, from 440 to 940 nm) and the other for the shortwave infrared (SWIR, from 940 to 2200 nm). OSIRIS has eight spectral bands in the VIS-NIR and six in the SWIR. During the SOP-

ACPD
15, 19615–19727, 2015

1a campaign, OSIRIS was flown aboard the French F-20 aircraft and looked at nadir. The quantities used to derive the aerosol and cloud properties from OSIRIS are the normalized total and polarized (unitless) radiances. The aerosol algorithm used for OSIRIS over ocean is an optimal estimation method (OEM), similar to the one described in Waquet et al. (2013). For ocean targets, we use all the available angular and polarized information acquired in three spectral bands (490, 670 and 865 nm) to derive the aerosol parameters and some properties of the surface. A combination of two log normal size distribution functions is assumed (i.e. a fine mode and a coarse mode) as well as a mixture of spherical and non-spherical particles (Dubovik et al., 2006). The main retrieved parameters are the aerosol AOD, SSA, the fraction of spherical particles within the coarse mode and the complex refractive index.

3.4 Balloons operations

Instrumented balloons were launched by the French Space Agency (CNES) from the airfield of Sant Lluís (39°51′55″ N, 04°15′15″, 55 m a.s.l.) on Minorca Island, less than 6 km NE of the Cap d'en Font station described above. Two types of balloons were launched to document dust transport events: (i) ascending dilatable rubber balloons, and (ii) quasi-Lagrangian spherical pressurized drifting balloons, called BPCL (Ballon Pressurisé de Couche Limite, or boundary-layer pressurized balloons).

A total of 15 sounding balloons were launched during the campaign between 12 June and 2 July (Table 4) and most balloons reached more than 30 km in altitude. Except for the first test balloon on 12 June, the payload of sounding balloons included a pair of meteorological sondes with temperature, humidity and GPS sensors allowing the retrieval of the position (±10 m), derived pressure (±1 hPa) and wind (±0.15 m s^{-1}), respectively coupled to an ozone electrochemical sonde (Gheusi et al., 2015) and a LOAC OPC (Renard et al., 2015a, b). Balloon trajectories were confined within the area 39–41.2° N in latitude and 3–5° E in longitude.

BPCLs are designed to drift and make observations with a payload of a few kg in the lower troposphere for durations of up to several weeks (Vialard et al., 2009). Two ver-

ACPD
15, 19615–19727, 2015

sions were used, the standard one of 2.5 m in diameter, launched pressurized, which is limited to a maximum float altitude of about 2.5 km (Ducrocq et al., 2014), and one developed for ChArMEx of 2.6 m in diameter, launched unpressurized to reach a float altitude of more than 3 km in altitude. The payload was composed of a GPS system, PTU instruments on the upper pole of the balloon, a LOAC instrument on the lower pole of the balloon and two solar radiation sensors for upward and downward solar flux measurements. In addition a BPCL equipped with a modified ozone electrochemical sonde (Gheusi et al., 2015) instead of a LOAC was launched in parallel of a LOAC balloon on 4 occasions on 16 and 17 June (BPCL B53 and B54, respectively), and on 2 July (BPCL B55 and B57). 14 BPCL balloons were launched in total between 16 June and 2 July 2013 (Table 5). Trajectories are plotted in Fig. 4 with a visualization of daytime vs. night-time conditions. The longest flight in terms of distance (1053 km) and time duration (32.6 h) was the ozone BPCL B57, which passed the Sicily strait and reached the southern limit of the authorized flight domain south-south-west of Malta. Communication failure occurred with the two balloons B53 and B70. Flights were automatically terminated by drilling the envelope at a distance of 30 km from south-eastern French coasts, western Sicily coast, or North Tunisian coast. BPCL float altitudes ranged between about 1850 and 3350 m a.m.s.l. (balloon B54 with an ozone sonde and B71 with a LOAC, respectively). Pairs of balloons with LOAC measurements were launched at different float altitudes to document Saharan dust transport on 16 June (2100 and ~ 3100 m a.m.s.l.) and 19 June (2550 and ~ 3500 m a.m.s.l.).

4 Overview of meteorological conditions

4.1 Synoptic situation

As mentioned below, the SOP-1a experiment was mostly characterized by moderate aerosol loading mainly controlled by the contribution of mineral dust particles. This situation is well observed through the AOD derived by MODIS, MISR, PARASOL or

ACPD
15, 19615–19727, 2015

SEVERI sensors and averaged for the June–July 2013 period (Fig. 5), which show an average AOD ranging between 0.2 and 0.4 (at 550 nm) over the western and central Mediterranean basins. During the SOP-1a, distinct meteorological conditions have led to the transport of mineral dust over the basin as shown in the Figs. 5 and 6. Figure 7 shows the dust mass concentration together with the geopotential and wind at 700 hPa for the 16, 19, 22, 29 June and 2 July. In the following sections, we discuss the meteorological conditions (surface wind, sea level pressure, 700 hPa geopotential and wind direction) for these different days in order to understand the transport of both mineral dust and anthropogenic aerosols over the Mediterranean.

Wind direction vertical profiles as simulated by the ALADIN regional model (outputs every 3 h) as a function of time, for the 11 June to 6 July period and for the whole SOP-1a period at three different sites: Ersa, Minorca and Lampedusa islands are shown in Fig. 8. At the beginning of the SOP-1a, the northwestern Mediterranean area was under the influence of a large pressure ridge at 700 hPa, generating a westerly to south-westerly flow over Spain and southern France. Over Minorca, the near surface (1000–850 hPa) winds were generally from the easterly to north-easterly direction (indicated by the blue color in the Fig. 8) while the wind direction estimated between 700 and 500 hPa was clearly from the south, southwest direction (brown color), which is a favourable condition for the transport of mineral dust above South-Spain and then Balearic islands (Fig. 6). This point is well observed in Fig. 7, showing the geopotential at 700 hPa for the 16 June. The general circulation at 700 hPa during this dust event indicates a reinforcement of the southwesterly winds in southern Spain advecting air masses with large concentrations of dust aerosols as shown by SEVERI AOD for that day (Fig. 6). A low pressure system moved from the British Isles towards the Gulf of Biscay and then the Iberian Peninsula between the 17 and 20 June, leading to veering winds that became southerly over the northwestern Mediterranean. Thus in Minorca, the direction of the wind changed from easterly to southerly direction between 1000 and 850 hPa. A more pronounced southerly-southwesterly flow was also observed at 700 hPa in Minorca (19–21 June) as shown by the geopotential at 700 hPa. This cir-

ACPD
15, 19615–19727, 2015

culation characterized by the presence of the low geopotential over the Gulf of Biscay induced a strong southerly flow at 700 hPa between the Balearic and Corsica islands associated with large dust optical depth concentrated in this zone as shown by SEVERI AOD for 19 June (Fig. 6). This period of the SOP-1a corresponds to the two ATR-42 flights 33 and 34 (Fig. 3). After 20 June, this low pressure system moved eastward, generating a trough located between France and Italy, and inducing a waving westerly flow over the north-western Mediterranean. As a result, the aerosol loading over the western basin decreased between 21 and 24 June, but the westerly (resp. northerly) winds observed at 700 hPa in Minorca (resp. Ersa) (Fig. 8) reinforced the transport of dust aerosols over the central basin and the Lampedusa station (where winds were from the north westerly direction at 3 km height). These meteorological conditions lead to an increase of the dust optical depth over the central Mediterranean as shown by the SEVERI instrument and AERONET/PHOTONS data. Between 25 and 29 June, a northwesterly flow set up between the Gulf of Lions and Sicily. The vertical profiles of the wind direction reveal a remarkable transition on 29 June with significant changes in direction from westerlies to north, north-westerlies, notably over the Minorca and Ersa stations above 850 hPa. The 700 hPa geopotential field on 29 June at 12:00 UTC from the ALADIN atmospheric model analysis shows a maximum over the Atlantic Ocean whereas a deep low pressure system was located over southern Algeria. This strong geopotential gradient lead to intense northerly to north-westerly winds at 700 hPa over the western basin leading to significant AOD over Libya and the Alboran sea as shown in Fig. 6. These meteorological conditions lead to low dust optical thickness over the central Mediterranean as observed by AERONET/PHOTONS data. Finally, during the last period of the SOP-1a experiment, (30 June–5 July), weather conditions became more anticyclonic over the region while low systems were confined to northern Europe. Figure 8 shows north-westerly winds in the whole troposphere in Lampedusa and Minorca, limiting the presence of dust aerosols to the southern part of the north-western Mediterranean.

ACPD
15, 19615–19727, 2015

4.2 Surface temperature, cloud cover and precipitation

In terms of surface temperature, which is one of the most important meteorological variables that control biogenic or biomass burning aerosol emissions over the Euro-Mediterranean region, the summer 2013 was mostly characterized by moderate values as shown in Fig. 9. Indeed, during the SOP-1a period, surface temperatures (in °C and at 12:00 UTC) derived from NCEP reanalysis for different days reveal moderate values especially over the western Mediterranean region (South-West France and Spain). One can observe temperatures of about 15–20 °C (at 12:00 UTC) over Spain and Portugal, which are one of the main regions of the Mediterranean where large fire events occur. In addition, part of France was also characterized by moderate surface temperature but slightly higher than over Spain especially over northeastern regions. A strong west to east gradient is observed over Europe with strongest values over the eastern regions (around 30 °C over Greece and the Balkans) compared to the western basin. A similar conclusion is obtained over the Mediterranean Sea with differences of about 5 °C between the eastern (around 25 °C for the SOP-1a period) and the western (around 20 °C) basin. Among other factors (such as cloud fraction and shortwave radiations), such moderate surface temperatures do not create favourable meteorological conditions to produce intense Mediterranean biomass burning events and/or significant production of secondary organic and inorganic aerosols. Concerning smoke aerosols, GAFS-V1 emission data, analysed for the SOP-1a period, do not reveal important primary BC and OC fluxes emissions (not shown). This is consistent with the APIFLAME biomass burning emission estimates (Turquety et al., 2014) data as reported by Menut et al. (2015).

During the SOP-1a, the cloud cover retrieved over the Euro-Mediterranean region (excluding the Mediterranean Sea) from CRU (Climate Research Unit) data (Fig. 10) indicates the largest values (between 75 and 95 %) over France, Benelux and Eastern Europe regions. In parallel, southern France, as well as western Spain and the Balkans are characterized by moderate cloud cover with values around 50–60 % for

ACPD
15, 19615–19727, 2015

June 2013. Over the Mediterranean coast, the cloud cover strongly decreases for most of countries, with values lower than 40 %. Such spatial cloud cover (observed during the SOP-1a) over the Euro-Mediterranean could limit the photochemical processes over the main anthropogenic sources (such as the Benelux and Po Valley) and the associated production of secondary aerosols. This could explain for a part the low to moderate contribution of fine anthropogenic particles to the total atmospheric loading during the SOP-1a. In parallel, the mean precipitation (averaged for June 2013), obtained from the TRMM (Tropical Rainfall Measuring Mission) instrument over land and sea (CRU observations are only available over land, see Fig. 10), are found to be very heterogeneous over the Euro-Mediterranean continental region, with some important values over the Balkans, Alps and eastern Europe (from 100 to 250 mm for the month of June 2013) and moderate values over Italy, Croatia, western France and Benelux (80 to 100 mm, as shown in the Fig. 11). Over the Mediterranean Sea, southern Spain and northern Africa, the precipitation was smaller, with most of values lower than 20 mm during the SOP-1a.

To summarize, this global view of the synoptic situation, cloud cover and regional precipitation patterns indicate that the meteorological conditions during the experimental campaign were favourable to moderate mineral dust emissions, associated with a weak contribution of anthropogenic aerosols over the western basin. This important characteristic of the SOP-1a is well observed in Fig. 12, which indicates the AOD anomalies of summer 2013 compared to all AOD summer derived from MODIS and MISR data. Indeed, negative AOD anomalies of about −0.05 are found over the western Mediterranean basin for the summer 2013, both from MODIS and MISR observations. To conclude, it appears that the period of observations during the SOP-1a was characterized by aerosol concentration slightly lower that usually observed during summer over the western Mediterranean. The level of aerosol concentration was found to be moderate but allows investigating several dust and sea-salt events as well as an unexpected and interesting intense biomass burning plume advected from North America.

ACPD
15, 19615–19727, 2015

4.3 An aged smoke plume advected over Europe

During the SOP-1a, several large forest fires occurred in North America (Colorado, Alaska, Canada) from 17 to 24 June 2013, as identified by the MODIS instrument. Absorbing aerosol index produced from GOME-2 by KNMI (http://www.temis.nl/aviation/aai-pmd-gome2b.php?year=2013) shows that a large smoke plume crossed the north Atlantic and reached Western Europe coasts on 25 June. Main fire areas, with fire radiative power higher than 50 MW (Shroeder et al., 2010), have been detected over Canada (Ancellet et al., 2015). Average MODIS AOD during the same period (23 to 28 June 2013) indicate values as high as 1 over the Atlantic Ocean, suggesting that a significant fraction of the aerosol produced by the fires was transported to Western Europe during the ChArMEx/ADRIMED field campaign. To investigate if the western Mediterranean has been impacted by these fires, a forward simulation of the Lagrangian plume dispersion model FLEXPART (Ancellet et al., 2015) has been conducted to quantify the spatial extent of the fire plume transport for 11 days. Fires emissions areas were identified by MODIS observations over several locations in Canada and Colorado. The aerosol mass is emitted in the transport model from 17 June to 28 in a 3 km layer as suggested by the CALIOP lidar observations over Canada. The biomass burning plume reaches much lower latitudes over Europe, down to the Western Mediterranean 4–10 days after the emission in Canada. During the SOP-1a, the plume was mainly present in the altitude range of 2.5–4.5 km and has been sampled by many remote sensing and in-situ instruments on 27 and 28 June; at Minorca and Cagliari surface stations, and between Sardinia and Lampedusa onboard the ATR-42 aircraft.

ACPD
15, 19615–19727, 2015

5 Overview of aerosol physical-chemical-optical properties, vertical profiles and local direct radiative forcing

5.1 Aerosol physical and chemical properties

5.1.1 Aerosol mass and number concentration at the two super-sites

First, PM concentrations between the two different stations are reported in the Fig. 13, which reports the daily time-series of PM_1 and PM_{10} at Ersa, as well as PM_{10} and PM_{40} at Lampedusa. The results indicate a significantly higher mass concentration at Lampedusa compared to Ersa. Indeed, the mass concentration observed at Lampedusa is comprised between 10 and 75 $\mu g\,m^{-3}$, with a mean of 37 $\mu g\,m^{-3}$, which is 4 times higher than the averaged PM_{10} ($\sim 9\,\mu g\,m^{-3}$) measured at Ersa. One can note the significant peak (maxima of 75 $\mu g\,m^{-3}$) at Lampedusa during the 24 to 26 June period that corresponds to a significant production of primary marine aerosols. Finally, the PM_1 concentration at Ersa is found to be almost constant during the period of the campaign, with a mean value of 6 $\mu g\,m^{-3}$. In addition, the background aerosol number concentrations (for $D_p > 0.01\,\mu m$) observed within the boundary layer in Corsica averaged $\sim 2000\,cm^{-3}$ (not shown). The lowest concentrations ($\sim 200\,cm^{-3}$) resulted from aerosol activation to cloud droplets, and scavenging from cloud droplets and rain drops, while high concentrations as high as $10\,000\,cm^{-3}$ were observed during pollution events from continental European air masses. The number concentrations showed a diurnal cycle suggesting that the site was situated within the marine boundary layer during daytime and within the free troposphere during night-time. The analysis of the diurnal variation of the particle number size distribution is further indicating that nucleation events also increased the particle number concentration during daytime, about one third of the time (Sellegri et al., 2015). The periods of high aerosol number concentrations detected between the 12 and 25 June were also dominated by a single mode with diameters between 30 and 150 nm. The small Aitken mode (dg < 50 nm) as-

ACPD
15, 19615–19727, 2015

sociated with pollution events suggests a relatively fresh aerosol that has been formed during transport from the European continent. The largest mode (dg ∼ 150 nm) occurred during the dust event on 18 June.

5.1.2 Columnar particle volume size distribution

We have used the column-integrated particle size volume distributions derived from AERONET/PHOTONS sky radiance measurements (Dubovik et al., 2000). These size distributions allow investigating the changes in aerosol size distribution between different stations during the SOP-1a and over the western basin. Four different stations have been studied, which include the two super-sites of Lampedusa and Ersa, as well as the aircraft and balloon base stations; Cagliari and Cap d'En Font, respectively. Daily volume size distributions for both sites are represented in the Fig. 14, as well as the averaged (red curve) size distribution for the whole period (1 June to 5 July) and the number of observations. In addition, the mean values of the volume radius, concentration of fine and coarse mode and the standard deviations of the volume size distribution are reported in the Table 6. It should be noted that the scales of the *y* axis are different for each figure. One can note the bimodal size distribution for both stations with large spread of radius values, especially for the coarse mode. The most important concentrations are obviously observed in Lampedusa, near the mineral dust sources, with maxima of $\sim 0.12\,\mu m^3\,\mu m^{-2}$ for the coarse mode. In parallel, the lowest concentrations are observed at the Ersa station, near the anthropogenic sources of the southern France and Italy. This is well consistent with the absence of intense polluted-photochemical or smoke aerosol events during the SOP-1a. In that sense, the mean contribution (red curve) of the coarse mode to the aerosol volume size distribution appears to be predominant at most sites, except at the Ersa station. This point is well noted for the Cap d'En Font station, where the concentration of each modes appear as equivalent, due to the absence of pollution from the Iberian Peninsula during the period of observations. For this site, it is interesting to note the intense peak for the 27 June, with concentration near $0.08\,\mu m^3\,\mu m^{-2}$, which is due to the transport of an

ACPD
15, 19615–19727, 2015

important smoke plume over the Mediterranean (see Ancellet et al., 2015 and Pelon et al., 2015). Finally, the contribution of the coarse mode clearly increases for the two other, more southern Italian sites of Cagliari and Lampedusa, which are more affected by the mineral dust compared to Ersa and Cap d'En Font. The variability of AERONET products collected over a period of four years at Ersa and Palma de Mallorca, near Cap d'En Font, is reported in Sicard et al. (2015). It is interesting to note the important variability in the derived size of the coarse mode at Lampedusa (see Table 6), which will be analysed in regards to dust sources in a future study. The derived volume concentrations over these two stations highlight the moderate dust activity occurring during the SOP-1a experiment, when compared to stations under high dust conditions. As an example of comparisons, Dubovik et al. (2002) reported a large range of concentration for the coarse mode for dusty sites (such as Cape Verde or Solar Village), which are characterized by larger concentrations, close to 0.30 $\mu m^3 \mu m^{-2}$. In parallel, the Bahrain (Persian Gulf) AERONET station is characterized by a concentration of 0.14–0.15 $\mu m^3 \mu m^{-2}$.

5.1.3 Particle size distribution during transport

Figure 15 presents an example of the evolution of the aerosol particle number concentrations in the 19 particle size classes of the LOAC instrument as measured along the northward trajectory of the BPCL balloon B74 from Minorca Island to the French coast (see Fig. 4). The balloon was launched at 09:46 UTC on 16 June 2013 during a moderate desert dust event shown on top of Fig. 6 (AERONET-derived AOD at 500 nm of 0.15). It drifted at a constant altitude of ~ 2.1 km at the bottom of the African dust layer observed with the WALI lidar at Minorca (not shown; see Chazette et al., 2015), and was automatically forced to land on the sea before reaching the coast South of Marseille, after a 12 h flight of 368 km. The dominant mineral dust nature of the particles was confirmed by the LOAC particle typology measurements (Renard et al., 2015). The figure illustrates that LOAC has detected large particles of up to 50 µm in diameter, although the plume originated from North-Africa a few days before (Renard et al.,

ACPD
15, 19615–19727, 2015

2015b). The concentrations of particles remained relatively constant during the flight, suggesting either no significant sedimentation of the largest particles during the flight or compensation by particles coming from above. The BPCL balloon B70 launched a few minutes later drifted at an upper altitude of ∼ 3.1 km and followed a different trajectory towards East (Fig. 4) but showed a quite similar extended particle size range with larger concentrations in almost all channels except the extremes (not shown). The 4 other drifting balloons launched in the dust layer during this event on 17 and 19 June (Table 5) did confirm the presence of very large particles (> 20 µm), which cannot be reported by AERONET particle size distribution retrieval algorithm (Hashimoto et al., 2012). In addition, observations of large particles (> 15 µm) was systematically found during all other LOAC balloon flights drifting in African dust layers, which will need further analysis to better understand the process that can maintain such large particles in suspension during several days.

5.1.4 Aerosol chemical composition

In terms of aerosol chemical properties, an example of averaged mass-size distributions for carbonaceous (Elemental and Organic Carbon, EC and OC) species (mass size distribution of inorganic and mineral dust aerosols are not shown) obtained at Ersa from a 12-stage cascade impactor (DEKATI system, see Table 1) is reported in Fig. 16. As mentioned in Table 1, the measurements were obtained by using a 2 day collection period in order to obtain a sufficient aerosol mass on filters for chemical analyses. This system provides the speciation of the mass size distribution, including fine and coarse fractions. Such information is very useful to derive optical properties using Mie calculations (Mallet et al., 2011) for the main particle types (sulfates, ammonium, nitrates, sea-salt, dust, black and organic carbon). This provides crucial information's on key radiative properties which are classically used in regional climate models (mass extinction efficiencies, SSA and asymmetry parameter). Furthermore, it allows one to assess the spectral dependence of radiative properties, which cannot always be estimated from in-situ instrumentation.

ACPD
15, 19615–19727, 2015

Concerning OC (blue curves), observations clearly report a bi-modal mass size distribution with two different peaks for the majority of cases. The first (almost constant) peak is found in the 0.4–0.5 µm size range in diameter and more occasionally a second one occurs in the coarse fraction around 3 µm. Compared to the few available data over the Western Mediterranean, these mass size distributions are found to be different from those obtained over Southern France, especially for the accumulation mode. Indeed, during the ESCOMPTE experiment in southern France, Mallet et al. (2003) also observed a bi-modal size distribution for OC aerosols but with a finer accumulation mode observed in the 0.1–0.2 µm size range. Differences between the two observations is likely due to the proximity of anthropogenic sources during the ESCOMPTE experiment compared to the Ersa station, where the possible ageing of carbonaceous particles could affect the size of aerosols. On the contrary, the coarse mode of OC appears in the same range of size, around 3 µm, for both experiments. Compared to data obtained in the eastern Mediterranean basin, the OC mass size distributions are in good agreement with those estimated by Sciare et al. (2003) in Crete during the MINOS campaign, with two modes around 0.4 and 3 µm. The BC (green curves in Fig. 16) mass size distribution is also characterized by a bi-modal size distribution, with two modes well correlated with the mass size distribution of OC, except for the 16–19 June period (dust episode), where the size of EC fine mode is higher ($\sim$ 0.5–0.6 µm) than OC aerosols, the EC coarse mode remaining similar at $\sim$ 3 µm. This reveals a possible external mixing of carbonaceous aerosols for this event.

In most cases, we observed at Ersa lower concentrations of EC particles for both modes compared to OC aerosols. The mass of OC and BC observed during the SOP-1a, for both modes, are found to be equivalent with those observed by Sciare et al. (2003) in Crete in summer 2001. They report mean values of 0.30 and 0.15 µg m^{-3} for fine OC and BC, respectively. During the MINOS experiment, the mean concentrations for OC and BC coarse modes were about 0.1 and 0.02–0.03 µg m^{-3}, what is also consistent with the observations at Ersa. Finally, the mass concentrations obtained for each mode at Ersa are logically lower than those obtained during the ESCOMPTE

ACPD
15, 19615–19727, 2015

experiment, located much closer to pollution sources. For example, EC and OC fine mode concentrations were respectively between 0.8 and 2.8 $\mu g\,m^{-3}$ and between 3.1 and 6.9 $\mu g\,m^{-3}$ during ESCOMPTE (Mallet et al., 2003). It should be noted that, in parallel to filter analyses, higher time resolved observations from the PILS systems have been deployed at the two stations of Lampedusa and Ersa during the SOP-1a.

In parallel to filters chemical analysis, over 700 000 single particle mass spectra were generated by the A-TOFMS instrument during the sampling period (not shown). A K-means algorithm ($K = 80$), as described in detail by Healy et al. (2010) and Gross et al. (2010) was used to classify aerosol mass spectra into different particle classes. More than 40 distinct ATOFMS particle classes were identified and subsequently grouped into 8 general categories for clarity. Elemental carbon containing particles dominated the dataset (55 % of total spectra), followed by K-rich particles (30 %) and sea-salt (7 %). The remaining particle categories include organic carbon (OC)-containing (3 %), trimethylamine (TMA)-containing (3 %), shipping (2 %), Fe-containing (0.5 %) and Ca-containing (0.3 %). EC particles dominated the first third of the sampling period, decreased noticeably for approx. 6 days and then dominated the rest of the sampling period again. In contrast, K-rich particle (associated with biomass burning and dust) numbers were high only for the latter half of the campaign, with a peak on 27–28 June. The profiles of these two particle categories suggest transport from regional sources. Sea-salt particle numbers were at their highest during the period where EC particles were at their lowest, and were generally low when EC particle numbers were high. OC-containing particles were present during the same period K-rich numbers peaked, suggesting an association with the transport of biomass burning particles. TMA particles were present in low numbers throughout the sampling period, suggesting a less regional source, independent of the air masses influencing EC and sea-salt particle occurrence. The same can be said of Fe and Ca-containing particles, likely to be local dust, while shipping particle numbers were slightly higher during the first half of the sampling period.

ACPD
15, 19615–19727, 2015

5.2 Aerosol optical properties

5.2.1 In-situ optical properties at the surface

Figure 17 reports the (daily mean) time-series of nephelometer observations obtained at the surface for the Ersa and Lampedusa stations during the SOP-1a. Daily scattering coefficients (at the three nephelometer wavelengths of 450, 550 and 700 nm) are reported, as well as the scattering Angström exponent (AE) calculated between 450 and 700 nm. At 550 nm and at Ersa, the scattering coefficient presents a significant variability during the SOP-1a with peaks of about 35–40 Mm^{-1} during the dust event (19–20 June) transported over the Corsica island, associated to low values (15 Mm^{-1}) for certain periods of time, as for 21–22 June. The mean scattering coefficient (at 550 nm) is 24 Mm^{-1}. Such scattering coefficient values are comparable to observations reported by Vaishya et al. (2012) at the Mace Head station for Atlantic marine air, with scattering coefficient (at 550 nm) comprised between 10 and 25 Mm^{-1} during the summer period. In terms of scattering spectral dependence, the calculated scattering AE is found to be almost constant, with AE ∼ 1.5–2 and a mean value of 1.71 (indicating that scattering is mostly dominated by fine aerosols) during the SOP-1a, except for the 23–24 June. The lowest values (AE ∼ 0.3–0.5) observed during this period are the result of a large contribution of coarse sea-salt aerosols (Claeys et al., 2015), which is also observed from the filter chemical size-resolved analyses and detected on the A-TOFMS and VHTDMA data. In parallel, we observe that the dust event occurring in Ersa on 18–20 June is not correlated to low scattering AE, revealing a possible contribution of fine dust particles only to scattering, result of a possible deposition of the coarse dust fraction during transport. The AERONET-derived AE between 440 and 870 nm shows values < 1 in the afternoon of 19 June and early morning of 20 June suggesting that coarse dust is present in the column. At Lampedusa, where the nephelometer was sampling from a PM_{40} inlet, the daily scattering coefficient (at 550 nm) is between 20 to 90 Mm^{-1} (mean value of 50 Mm^{-1}), which is twice higher than at Ersa (Fig. 17). The scattering

ACPD
15, 19615–19727, 2015

AE was also highly variable, with values comprised between 0.5 and 2.5 (mean value of 1.13). The range of variability of these values is due to the observed switch from clean air masses strongly impacted by marine emissions to polluted air masses of various ages, including very aged/processed air masses from Northern Europe. A single intrusion of mineral dust at the site was recorded on 9 June as a result of a cyclone-type of transport from Tunisia (Formenti et al., 2015).

5.2.2 Remote-sensing observations from the surface

The optical properties obtained from sun-photometer observations for different AERONET/PHOTONS sites are shown in Fig. 18. The total AOD, Absorbing Aerosol Optical Depth (AAOD), AOD for the fine (AODf) and coarse (AODc) modes of the volume size distribution, are indicated (at 440 nm) for 11 AERONET/PHOTONS stations (Table 2). As mentioned previously, the AOD time-series for the complete SOP-1a period reveal moderate values, never reaching values as large as reported during the summer 2012 ChArMEx/TRAQA SOP-0 experiment (Rea et al., 2015). During summer 2013, the AOD was generally comprised between 0.1 and 0.7 (at 440 nm) for most of the AERONET/PHOTONS sites. Over the western basin, the Granada, Minorca and Barcelona sites display the largest values during the transport of dust aerosols as detected by satellite remote-sensing observations (Fig. 6) for the 16 to 20 June. During this dust event, the contribution of fine and coarse modes to the total extinction AOD is equivalent. Over the central basin, Lampedusa data reveal various peaks. The largest AOD was measured on 6 June (about 0.84 at 440 nm) and 8 June (about 0.63 at 440 nm). Other peaks occurred around 22 June and 1–2 July, with corresponding AOD of about 0.30–0.40 (at 440 nm), with again an equivalent contribution of each particle size mode of the volume size distribution to the AOD. On 27–28 June, an AOD peak was also observed over most of the sites and corresponded to the transport of an aged smoke plume from the Canadian continent. In this specific case, AOD was comprised between 0.25 and 0.50 (at 440 nm) and affected all sites. Contrarily to the previously mentioned dust events, the contribution of the different modes to AOD was significantly

ACPD
15, 19615–19727, 2015

different during this episode. Indeed, as shown in Fig. 18, AOD was mostly controlled by the fine mode of the volume size distribution. This specific biomass burning case is more deeply analysed by Ancellet et al. (2015) and Pelon et al. (2015).

We have also used the SSA dataset from AERONET/PHOTONS network for making comparisons of its optical parameters between different stations during the SOP-1a. As for the size distributions, we have analysed dataset in four stations, which are Ersa, Lampedusa, Cagliari and Cap d'En Font. All (daily) SSA retrievals, associated with the mean values (at the four wavelengths), are included in the Fig. 19 and Table 7. Due to the moderate AOD over the period, we used Level 1.5 AERONET/PHOTONS products. In that sense, it should be reminded that uncertainties associated to SSA retrievals are important, about ±0.07 as reported by Dubovik et al. (2000). The results indicate an important variability of aerosol SSA and its spectral dependence over the different stations. At the wavelength of 440 nm, the mean SSA is comprised between 0.91 and 0.98, with the lowest (resp. highest) value observed in Lampedusa (resp. Ersa). Hence, aerosols appear as almost scattering at Ersa and moderately absorbing at Lampedusa. The contribution of the coarse mode to the total size distribution could explain the lower values observed in Lampedusa at this wavelength. Indeed, the radiative effects and optical properties of dust are strongly dependent on the coarse mode size distribution as the larger particles appreciably decrease the SSA (McConnell et al., 2010; Otto et al., 2009). More recently and during the FENNEC experiment, Ryder et al. (2013) have calculated SSA (at 550 nm) for dust aerosols using the full range of sizes measured, indicating that dust SSA was highly sensitive to effective diameter: size distributions with the largest effective diameters produced the lowest SSA values. Observations for the Cap d'En Font and Cagliari stations reveal an intermediate value (0.93 at 440 nm) in Cagliari, which is also more affected by mineral dust aerosols (Fig. 13). We can also observe very low values in Cagliari (for the period of 14 to 17 June) that could be due to local pollution. Anyway, it should be remained that those retrievals have been performed under low AOD (~ 0.10 at 440 nm) conditions and are associated to large uncertainties. One important point concerns the changes in the SSA spectral signature

ACPD
15, 19615–19727, 2015

between Ersa (negative tendency between 440 to 1020 nm) and Lampedusa (positive) stations. This observation is very consistent with AERONET/PHOTONS data analysed for a long-time period over the Mediterranean by Mallet et al. (2013), who report different spectral variations in SSA, following the aerosol regime (dusty and/or polluted particles). One of the main conclusions here is that aerosols are found to be moderately absorbing during the SOP-1a period, what is consistent with in-situ observations performed onboard the ATR-42 aircraft and summarized by Denjean et al. (2015).

5.2.3 ATR-42 and F-20 aircraft observations

In parallel to surface observations, an example of the vertical profiles of aerosol optical properties obtained from ATR-42 measurements is shown Fig. 20 that corresponds to the flight 35–36 over the station of Lampedusa for the 22 June (see also Denjean et al., 2015 and Nicolas et al., 2015). Scattering coefficients (in Mm^{-1}) are plotted at 450, 550 and 700 nm (left) vs. altitude (in m). Completely different behaviours in the scattering spectral dependence as a function of altitude was observed (Fig. 20). Two different aerosol plumes characterized by a significant spectral dependence (typically of submicronic polluted, smoke or fine marine aerosols) are observed around 1000 and 2000–2500 m. Above 3000 m, the spectral dependence is clearly reduced, corresponding to air masses with high mineral dust concentrations. For this upper aerosol layer, the scattering coefficient increases up to 60 Mm^{-1}. The analysis of the extinction (at 530 nm) vertical profiles obtained from the CAPS system (Table 3) reveals an excellent agreement with nephelometer data showing the peaks of extinction at similar altitudes (see Denjean et al., 2015), with maxima ($\sim$ 90 Mm^{-1}) logically observed within the dust plumes (4000–5000 m). Number concentration of particles, as well as volume size distributions, highlight the significant atmospheric loading by aerosol particles with diameter higher than 1 µm above 3000 m (maxima of 5000 # cm^{-3}). For this atmospheric layer, the aerosol volume size distribution is characterized by a coarse mode, with a mode around 6–8 µm. As previously mentioned, vertical profiles of optical properties in terms of AE, single scattering albedo, asymmetry parameters as

ACPD
15, 19615–19727, 2015

well as their spectral dependence are presented and discussed in details by Denjean et al. (2015) and Nicolas et al. (2015). The airborne SW and LW radiation measurements and the comparison with radiative transfer model simulations at Lampedusa are presented by M. Meloni et al. (2015).

5.3 Aerosol vertical structure

5.3.1 Lidar surface observations

Although deeply analysed in other dedicated papers, some examples of the aerosol vertical profiles are presented here. First and over the Minorca station, surface lidar observations in Fig. 21a were obtained during 16 and 17 June, that corresponds to the first event of transported mineral dust over the western basin. They show a dust aerosol layer located between 1.5 and 5 km, with a maximum of aerosol extinction (at 355 nm) around 0.10 km^{-1} on 16 June between 12:00 and 14:00 LT. Comparisons of retrieved AOD with the lidar system is shown to be very consistent with sun-photometer observations for these two days (Fig. 21a, top), with moderate AOD (at 355 nm) comprised between 0.2 and 0.4 at maximum. During 17 June, the dust layer is less intense and the aerosol extinction above 1.5 km decreases. After 14:00 LT, Fig. 21a clearly shows that most of the contribution to AOD is due to the MBL over the Minorca station. At Ersa (Fig. 21b), the dust event reached the northern tip of Corsica on 19 June. A deep depolarizing aerosol layer was observed at altitudes between 3 and 6 km. In the night of the 20, the particulate depolarization ratio is close to 18 % and the lidar ratio within the dust layer was estimated at 46 sr. The extinction coefficient remains moderate within the dust layer $\sim 0.05\,km^{-1}$ (Fig. 21b) between 4 and 6 km. It should be noted that a complete analysis of lidar observations series obtained over the cape Corsica site is reported in Leon et al. (2015). The dust event vertical distribution is further analysed by means of the EARLINET lidar stations in Sicard et al. (2015) and by means of the EARLINET and ChArMEx lidar stations in Barragan et al. (2015).

ACPD
15, 19615–19727, 2015

In addition to Minorca and Ersa, two lidars were also operated at Lampedusa during the SOP-1a and provided vertical profiles of aerosol backscattering and depolarization. The ENEA/University of Rome lidar measures the aerosol backscattering at 532 and 1064 nm, plus the depolarization at 532 nm. This system was operated throughout the campaign, although not continuously. The lidar data retrieval is described by Di Iorio et al. (2009), and uses sun-photometer AOD observations to constrain the determination of the aerosol backscattering profile. Figure 22a shows the evolution of the vertical profile of the aerosol backscattering coefficient at 1064 nm on 03 July 2013 at Lampedusa. At low altitudes the air masses reaching Lampedusa originated from the North. Air masses above 2 km conversely came from a southwesterly direction crossing North Algeria and Tunisia, and carried desert dust. Elevated backscattering attributed to dust was observed up to 5 km altitude, and a steep transition in the backscattering coefficient occurred at this altitude throughout the day. Figure 22b shows the backscattering coefficient profile at 532 and 1064 nm, and the depolarization ratio measured at 15:45 UT by the ENEA/University of Rome and the LISA lidars. Evidently, the backscattering coefficient above 2 km shows very small wavelength dependence, and elevated values of the depolarization ratio, as expected from large irregular desert dust particles (Sassen, 1999). The influence of large particles is smaller below 2 km, where the backscattering coefficient shows some dependency on wavelength, and the depolarization ratio decreases. The significant role played by the large particles on 3 July is also confirmed by the aerosol size distribution and optical properties (i.e., values and spectral dependency of the refractive index and single scattering albedo) retrieved from the AERONET observations at Lampedusa. The average AOD (at 500 nm) was 0.28, and the Angström exponent was 0.39, as expected for cases with a large contribution of desert dust. The retrieved columnar volume size distributions on the two days show that the mode with a median radius around 2 µm is 2–3 times more intense on 3 July than on 17 June.

Finally, nighttime measurements at Potenza (Italy) on 21 June starting at 23:40 UT, which coincides with the arrival of the Saharan dust event over southern Italy, indicate

ACPD
15, 19615–19727, 2015

a clear signature of Saharan dust in the tropospheric layer between 1.8 and 3.9 km, an extinction-related AE value of approximately 0 is measured between roughly 2 and 3 km and a quite constant LR around 50 sr at both 355 and 532 nm (not shown, see Sicard et al., 2015; Barragan et al., 2015).

5.3.2 LNG observations

An example of LNG (Lidar Nouvelle Génération) observations onboard the F-20 aircraft is presented in the Fig. 23 for the 19 June that corresponds to a flight (12:46 to 13:26 UT) from the Gulf of Genoa to Sardinia. The aerosol extinction (in km^{-1} and at 532 nm) is represented in function of latitude during this flight as well as the associated AOD with a high temporal and spatial frequency. One can observe the significant North–South gradient during this dust event with low-values of AOD (around 0.1 at 532 nm) for latitude of 44° N and moderate-high AOD (0.40 to 0.55) for latitudes lower than 42–43° N. In terms of vertical structure, this increase of AOD is due to an upper dust layer (around 5 to 6 km) characterized by an aerosol extinction of about 0.1 km^{-1}. This intense dust layer transported over most of the investigated region (40.5–43.5° N) is associated with a second more diluted aerosol layer observed between 3 and 4 km with LNG. Another interesting aspect is the variability of aerosol extinction detected in the marine boundary layer showing large differences throughout the F-20 transect. The aerosol extinction is found to be significant around 41 to 41.5° N that could be due to sea-salt particles generated in south Corsica Island due to the local acceleration of the wind occurring between the Corsica and Sardinia islands (not shown). This increase of the aerosol loading in the MBL associated with dust aerosol transported to higher altitudes results in an increase of total AOD at these latitudes. Such aircraft lidar data will be useful for testing the different modeling systems used for the SOP-1a experiment and more specifically their ability to reproduce complex vertical aerosol structures over the western Mediterranean. Additional observations of the aerosol extinction vertical profile obtained over different surface-stations from the passive remote-sensing PLASMA instrument onboard the ATR-42 aircraft are presented in Torres et al. (2015).

ACPD
15, 19615–19727, 2015

5.3.3 Sounding balloon observations

Figure 24 shows an example of the vertical profile of the aerosol particle size distribution obtained on 19 June near the end of the dust episode that started on 16 June over Minorca. The daytime average AOD geographical distribution derived from MSG/SEVIRI is shown in Fig. 6. The vertical profile clearly shows the presence of the dust layer between about 2.5 and 4.5 km in altitude, in agreement with coincident lidar continuous observations at Minorca that show the more limited vertical extent of dust compared to previous days and the end of the episode on 19 June in this area (Chazette et al., 2015). It should be noted that sounding balloons appear to underdetect very large particles within dust layers compared to the drifting balloons. This can be due isokinetic sampling differences between sounding systems that have a vertical velocity of several $m\,s^{-1}$ and systems drifting at a constant air density that are quasi-Lagrangian. However coincident AERONET and LOAC vertically integrated particle size distribution in the range 0.1–30 µm in diameter performed on 16 and 17 June were found quite comparable. In the marine atmospheric boundary layer, the LOAC speciation index (Renard et al., 2015a) indicates hydrated particles. In the free troposphere above dust, the concentration of particles rapidly decreased by one order of magnitude and particles were mainly of submicronic size with sometimes a significant number of particles in the 1.1–3 µm channel.

5.4 Local direct radiative forcing

5.4.1 Estimates using in-situ aircraft data and radiative transfer codes over the two super-sites

Before investigating the possible climatic effect of aerosols on the Mediterranean climate, an important preliminary step is the calculation of the direct radiative forcing (DRF) exerted by aerosols. This can be addressed by using in-situ (physical-optical properties) and remote-sensing (vertical profiles) observations of aerosols as input to

ACPD
15, 19615–19727, 2015

radiative transfer models. Simulated SW and LW radiative fluxes can be evaluated using observed radiative fluxes both at the surface and onboard the two aircraft. The combination of in-situ and remote sensing measurements provide a complete and unique dataset for conducting such 1-D radiative transfer simulations. To this end, vertical profiles from the ATR-42 were combined with surface observations from the two (Ersa and Lampedusa) stations to calculate the SW DRF of different aerosol events (Nicolas et al., 2015; M. Meloni et al., 2015). Over the western basin and for the first period of the campaign (16 to 20 June), different calculations, with the GAME radiative transfer model (Dubuisson et al., 2004), of the downward and upward SW cloud-free irradiances have been performed by Nicolas et al. (2015) for 6 vertical profiles over Granada, Minorca and Corsica islands. Briefly, the methodology is based on extinction, SSA and phase function vertical profiles (and their spectral dependence), obtained from observations and Mie calculations, and associated with atmospheric thermodynamic properties. They clearly show a significant change in surface radiative fluxes with a well-known decrease (dimming effect) of downward radiations due to scattering and absorption of solar radiation by dust aerosols. Inter-comparisons between observed/simulated downward and upward clear-sky SW fluxes show a good agreement during the ascent and descent profiles. At TOA, Nicolas et al. (2015) reported a direct (instantaneous at noon) SW DRF comprised between −4 and −33 $W m^{-2}$, revealing a cooling effect due to dust particles. These simulations also indicate that the decrease in surface radiation is not completely compensated by the TOA cooling, meaning that aerosols exerted a positive atmospheric forcing due to their ability to absorb solar radiations.

Similar calculations (not shown) have been done over the Lampedusa reference-site by Meloni et al. (2015) by using a similar method based on lidar, sun-photometer, in-situ surface, ATR-42 and F-20 observations and the MODTRAN 5.3 radiative transfer code. Meloni et al. (2015) estimate both the SW and the LW aerosol radiative forcing profiles and the balance between the two spectral components (SW and LW). During the descent towards Lampedusa airport on 22 June, the instantaneous (12.5° solar zenith angle and aerosol optical depth at 500 nm of 0.32) SW cooling at the surface

ACPD
15, 19615–19727, 2015

($-44\,W\,m^{-2}$) is reduced by about 10 % due to infrared emission. The dust SW radiative forcing at TOA is $-6\,W\,m^{-2}$. These values are obtained using the AERONET aerosol size distribution and different aerosol refractive indices in the SW and in the LW spectral regions. The LW contribution at the surface is lower than the values reported in previous studies (di Sarra et al., 2011; Meloni et al., 2015), partially due to the different solar zenith angle and to the presence of mixed aerosol below the dust layer down to the surface.

5.4.2 Estimates of instantaneous clear-sky SW DRF using AERONET/PHOTONS observations

As reported previously, AERONET/PHOTONS network provides, in addition to microphysical and optical aerosol properties, an estimate of the local (instantaneous) clear-sky direct radiative forcing at any AERONET/PHOTONS location as an operational product of the network. The method of derivation is described in Garcia et al. (2012). As mentioned above, the extremely good regional coverage of AERONET/PHOTONS sun-photometer instruments during the SOP-1a allow a complementary estimate of the local radiative (clear-sky) forcing to those derived by M. Meloni et al. (2015) and Nicolas et al. (2015). The Fig. 25 indicated the averaged of all instantaneous (clear-sky) DRF (in $W\,m^{-2}$) estimated during a day for both AERONET/PHOTONS station. Estimates are reported at the surface (bottom left), at TOA (bottom right) and within the total atmosphere (down). Averaged values of the DRF are also indicated in the Fig. 25. As mentioned above, sun-photometers retrievals demonstrate a significant DRF during the SOP-1a experiment. As an example and at the surface, the mean forcing is comprised between $-15\,W\,m^{-2}$ (Barcelona, not affected by dust transport) and $-35\,W\,m^{-2}$ in Burjassot. Such values are consistent with independent 1-D estimates reported by Nicolas et al. (2015) and M. Meloni et al. (2015). AERONET/PHOTONS data also reveal a negative DRF at TOA over most of sites, meaning that aerosols exert in majority a cooling effect at TOA, with values around ~ -6 to $-12\,W\,m^{-2}$. These negative values

ACPD
15, 19615–19727, 2015

are also due to the fact that most of AERONET/PHOTONS stations are located over islands, which are characterized by low surface albedo. Logically and due to the moderate values of aerosol absorption observed during the SOP-1a (Denjean et al., 2015), a positive atmospheric forcing is observed with mean values from +7 to +30 $W m^{-2}$ (with maxima in Burjassot), that could affect the vertical profiles of temperature and relative humidity as shown recently by Nabat et al. (2015).

5.4.3 Estimates using in-situ radiative flux observations

As shown by di Sarra et al. (2011), an estimate of the aerosol radiative forcing can be obtained by comparing irradiance measurements made during days characterized by different aerosol loads. In particular, the identification of a cloud-free day with low aerosol amounts is important to provide a reference for pristine conditions. During the SOP-1a, 17 June at Lampedusa displayed a very low aerosol optical depth (daily average of 0.064 at 500 nm) and cloud-free conditions throughout the day, and was identified as the reference day for pristine conditions. 3 July, conversely, was one of the days characterized by the presence of desert dust, with moderately high values of the AOD (0.28). As shown in Fig. 22a, dust was present above 2 km altitude and there were no major changes in the aerosol vertical distribution during the day, as it also appears from the limited daily variability of the AOD (daily standard deviation of the AOD at 500 nm of 0.015). Cloud-free conditions were present throughout the day.

Figure 26 displays the downward solar irradiance measured on 3 July, compared with the one measured on the pristine reference day (17 June). The irradiance measurements were corrected for the radiometer thermal offset as discussed by Di Biagio et al. (2009). The sharp narrow peak occurring on 17 June around 06:30 was related to a small isolated cloud, and these data were discarded from the analysis. The differences between the downward irradiances measured on these two days were calculated as a function of the solar zenith angle; these differences are due to the effect of aerosol and, to a smaller extent, column water vapour. The effect of water vapour was estimated by means of a radiative transfer model (see e.g., di Sarra et al., 2011), and the

ACPD
15, 19615–19727, 2015

remaining difference was integrated over 24 h to obtain the daily average effect, ΔI, on the downward solar irradiance. The daily aerosol radiative forcing RF can be derived as:

$$RF = \Delta I/(1 - A)$$

where ΔI is the difference between the two curves of Fig. 26 integrated over 24 h, and A is the surface albedo. For a surface albedo of 0.07 (di Sarra et al., 2011), the estimated surface RF is $-14.8\,W\,m^{-2}$. The radiative forcing efficiency RFE, which is the radiative forcing produced by a unit AOD, was calculated as:

$$RFE = RF/(AOD_2 - AOD_1)$$

where AOD_2 and AOD_1 are the measured daily average aerosol optical depth on 17 June and 3 July, respectively. The estimated RFE is $-67.4\,W\,m^{-2}$. Di Biagio et al. (2010), based on a multi-year dataset at Lampedusa, derived a similar value for desert dust ($-68.9\,W\,m^{-2}$) at the equinox; di Sarra et al. (2010), for an intense desert dust event occurring in March 2010 found values between -70 and $-85\,W\,m^{-2}$. For a desert dust event associated with the propagation of a gravity wave, with values of AOD similar to those of 3 July, di Sarra et al. (2013) derived an RFE equal to $-79\,W\,m^{-2}$. Values of the dust RFE at the surface in the same range were obtained by Derimian et al. (2006), although they were derived in different conditions for which the influence of surface albedo should be taken into account.

The downward LW irradiance measured on 3 July was higher than on 17 June by $23\,W\,m^{-2}$. Most of this effect is due to differences in the water vapour column amount (about 1 cm difference between the two days, with larger values on 3 July). Once the water vapour contribution was subtracted by means of radiative transfer calculations, we found a net positive effect induced by the aerosol of about $+5.5\,W\,m^{-2}$. This is, on the daily timescale, about 35 % of the SW effect. The resulting aerosol RFE in the LW spectral range is $+25.5\,W\,m^{-2}$, in agreement with previous results by di Sarra et al. (2011) who found values between +25.9 and $+27.9\,W\,m^{-2}$.

ACPD
15, 19615–19727, 2015

6 Overview of modeling activities

Several models are used to analyze the SOP-1a period: the meso-scale meteorological COSMO-MUSCAT model, the chemistry transport model (CTM) CHIMERE model, and two regional climate (RegCM and CNRM-RCSM) models. These models differ in terms of horizontal and vertical resolutions, physical parameterizations, aerosol-chemical schemes and are able to deliver complementary information to address key scientific questions of the ChArMEx/ADRIMED experiment. Their main characteristics are summarized in the Table 8.

6.1 COSMO-MUSCAT model

The parallelized multi-scale regional model system COSMO-MUSCAT (Wolke et al., 2012) consists of the non-hydrostatic atmosphere model COSMO (Consortium for Small-scale Modelling) that is on-line coupled to the 3-D chemistry tracer transport model MUSCAT (MUltiScale Chemistry Aerosol Transport Model). The atmospheric dust cycle consisting of the emission, transport and deposition of dust particles is simulated within MUSCAT using meteorological and hydrological fields from COSMO. Dust emission is calculated using the emission scheme by Tegen et al. (2002) and depends on local surface wind friction velocities, surface roughness length, soil texture and soil moisture. Calculated dust emission fluxes depend on particle diameter for individual size classes that are assumed to be log-normally distributed. Following Marticorena and Bergametti (1995), dust emission is considered as threshold function of local friction velocities and thus initial dust emission is computed as a function of soil particle size distribution. Dust emission is limited to regions where active dust sources have been identified during 2006–2009 from MSG SEVIRI observations (Schepanski et al., 2007). The advection of dust particles is described by a third order upstream scheme; dust particles are transported as passive tracer in five independent size classes with limiting radius at 0.1, 0.3, 0.9, 2.6, 8, and 24 µm. The removal of dust particles from the atmosphere is described by dry and wet deposition taking particle size, particle density,

ACPD
15, 19615–19727, 2015

and atmospheric conditions into account. Here, the simulations of the atmospheric dust cycle are performed at a 28 km horizontal grid and 40 vertical layers, covering North African dust sources, the eastern North Atlantic, the Mediterranean basin and Europe.

6.2 The CHIMERE chemistry-transport model

CHIMERE is a chemistry-transport model able to simulate concentrations fields of gaseous and aerosols species at a regional scale. The model is off-line and thus needs pre-calculated meteorological fields to run. In this study, we used the version fully described in Menut et al. (2013), forced by the WRF meso-scale model. The horizontal domain is the same as the one of WRF, and, for the vertical grid, the 28 vertical levels of WRF are projected on the 20 levels of the CHIMERE mesh. The gaseous species are calculated using the MELCHIOR 2 scheme and the aerosols using the scheme developed by Bessagnet et al. (2004). This module takes into account species such as sulfate, nitrate, ammonium, primary organic (OC) and black carbon (BC), secondary organic aerosols (SOA), sea-salt, mineral dust, and water. These aerosols are represented using ten bins, from 40 nm to 20 µm, in diameter. The life cycle of these aerosols is completely represented with nucleation of sulfuric acid, coagulation, adsorption/desorption, wet and dry deposition and scavenging. This scavenging is both represented by coagulation with cloud droplets and precipitation. The formation of SOA is also taken into account. The anthropogenic emissions are estimated using the same methodology as the one described in Menut et al. (2013) but with the HTAP masses as input data. These masses were prepared by the EDGAR Team, using inventories based on MICS-Asia, EPA-US/Canada and TNO databases (http://edgar.jrc.ec.europa.eu/htap_v2). Biogenic emissions are calculated using the MEGAN emissions scheme (Guenther et al., 2006), which provides fluxes of isoprene, terpene and pinenes. In addition to this 2013 version, several processes were improved and added in the framework of this study. First, mineral dust emissions are now calculated using new soil and surface databases, as described in Menut et al. (2013). Second, chemical species emissions fluxes produced by vegetation fires are estimated

ACPD
15, 19615–19727, 2015

using the new high resolution fire model presented in Turquety et al. (2014). Finally, the photolysis rates are explicitly calculated using the FastJ radiation module (Mailler et al., 2015).

6.3 The RegCM regional climate model

The RegCM system is a community model designed for use by a varied community composed of scientists in industrialized countries as well as developing nations. It is supported through the Regional Climate Network, or RegCNET, a widespread network of scientists coordinated by the Earth System Physics section of the Abdus Salam International Centre for the Theoretical Physics (ICTP, Giorgi et al., 2012). RegCM is a hydrostatic, compressible, sigma-p vertical coordinate model. As a limited area model, RegCM requires initial and boundary conditions that can be provided both by NCEP or ECMWF analyses. The horizontal resolution used need to be higher than 10 km, due to the hydrostatic dynamic core of the model, associated with 23 vertical levels. A simplified aerosol scheme specifically designed for application to long-term climate simulations has been incrementally developed within the RegCM system. Solmon et al. (2006, 2008) first implemented a first-generation aerosol model including sulfates, organic carbon, and black carbon. Zakey et al. (2006) then added a 4-bin desert dust module, and Zakey et al. (2008) implemented a 2-bin sea-salt scheme. In RegCM, the dust emission scheme accounts for sub-grid emissions by different types of soil. The dust emission size distribution can now also be treated according to Kok (2011). When all aerosols are simulated, 12 additional prognostic equations are solved in RegCM, including transport by resolvable scale winds, turbulence and deep convection, sources, and wet and dry removal processes. In RegCM, the natural/anthropogenic aerosols are radiatively interactive both in the solar and infrared regions and so are able to feedback on the meteorological fields.

ACPD
15, 19615–19727, 2015

6.4 The CNRM-RCSM Regional Climate model

The fully coupled RCSM (Regional Climate System Model), which is developed at CNRM has been also used within the ChArMEx/ADRIMED project. This model includes the regional climate atmospheric model ALADIN-Climate (Déqué and Somot, 2008), the regional ocean model NEMOMED8 (Beuvier et al., 2010) and the land-surface model ISBA (Noilhan and Mahfouf, 1996). We used here the version described in Nabat et al. (2015b) with a 50 km horizontal resolution. ALADIN-Climate includes the Fouquart and Morcrette radiation scheme based on the ECMWF model incorporating effects of greenhouse gases as well as direct effects of aerosols. The ocean model NEMOMED8 is the regional eddy-permitting version of the NEMOV2.3 ocean model that covers the Mediterranean Sea. Concerning the aerosol phase, the model ALADIN-Climate incorporates a radiative scheme to take into account the direct and semi-direct effects of five aerosol types (sea-salt, desert dust, sulfates, black and organic carbon aerosols) through either AOD climatologies or a prognostic aerosol scheme (Nabat et al., 2013, 2015b). On the one hand, Nabat et al. (2013) have proposed a new AOD monthly climatology over the period 2003–2009, based on a combination of satellite-derived and model-simulated products. The objective is having the best estimation of the atmospheric aerosol content for these five most relevant aerosol species. On the other hand, a prognostic aerosol scheme has been recently implemented in ALADIN-Climate, and has shown its ability to reproduce the main patterns of the aerosol variability over the Mediterranean (Nabat et al., 2015b).

6.5 SOP-1a multi-model aerosol simulations

6.5.1 Aerosol Optical Depth

Figure 27 reports the AOD (in the visible range) simulated for the SOP-1a period and for the COSMO-M, RegCM, CNRM-RCSM and CHIMERE models. Except the CTM-CHIMERE model which includes all the secondary species (SOA and inorganic), the

ACPD
15, 19615–19727, 2015

others have different aerosols schemes and take into account both natural (COSMO-M) or natural plus a part of anthropogenic aerosols as described in the Table 8. The configurations used for each models are listed in the Table 8. One can observe the large variability of AOD simulated by models over the Mediterranean region with highest values clearly simulated by the COSMO-M (AOD ∼ 1–1.5 in the visible wavelengths) over the Northern Africa region. The CHIMERE model indicates two different regions where AOD peaks around 1, over Algeria–Tunisia and southern of Morocco. For COSMO-M and CHIMERE, no intense dust AOD are simulated over the northeast Africa (Lybia and Egypt) and values are below 0.25, contrary to RegCM and CNRM-RCSM that simulate moderate AOD over this region with more intense peaks (∼ 0.7 for CNRM-RCSM simulations). Some identified regions with important AOD over Tunisia, Algeria, and South Morocco are well captured by all models except COSMO-M which show more intense AOD south of Algeria. It should be noted that this regional pattern of AOD is found to be consistent with MODIS observations as shown by Menut et al. (2015) for the CHIMERE model. Averaged over the SOP-1a period, all models simulate low to moderate AOD over the EURO-Mediterranean region which is consistent with AERONET/PHOTONS observations (Fig. 14). Once again and as noted by Menut et al. (2015), this modeling exercise clearly shows that the summer 2013 was not characterized by intense dust plumes or intense anthropogenic or forest fire emissions. However, modeling results indicate regular dust intrusions during the SOP-1a characterized by moderate atmospheric loads. Over Europe, the CTM CHIMERE model obviously simulate anthropogenic aerosol AOD (AOD ∼ 0.3), especially over the Benelux and Pô Valley that are not simulated by the two other regional models. Indeed, CNRM-RCSM simulations reveal a more diffuse AOD about 0.2 over Europe with maximum over Western France certainly due to the advection of primary marine particles generated over the Atlantic Ocean. RegCM simulations indicate a plume of anthropogenic aerosols over the Balkan region mainly due to secondary inorganic species. As RegCM does not use the spectral nudging technique in this simulation and are only forced at the boundaries during the period of simulation, some biases in meteorological fields could appear (as

ACPD
15, 19615–19727, 2015

for the precipitation location and intensity), which need to be evaluated. Finally and in addition to analysis of the AOD regional pattern, a specific comparison with in-situ observations and remote-sensing (AERONET/PHOTONS and satellite) data has been made for the CTM-CHIMERE model (Menut et al., 2015) and is planned in accompanied studies for the COSMO-M, RegCM and CNRM-RCSM models, associated with an inter-comparison exercise for evaluating the dust emissions, vertical distribution, size distribution and dry/wet deposition using all data collected in the framework of the SOP-1a.

In parallel to time averaged AOD simulated at the regional scale, we report comparisons of simulated AOD with AERONET/PHOTONS data for the two reference stations (Lampedusa and Ersa). As reported in Table 8, it should be reminded here that all models did not take into account aerosol species in a similar way. As an example, COSMO-MUSCAT includes mineral dust only in this simulation, while CNRM-RCSM and RegCM model include natural (sea-salt and dust) and sulfates as well as secondary ammonium and nitrate particles (treated as bulk aerosols) but for RegCM only. The most complete regional model (in terms of aerosol phase) is CHIMERE, which takes into account natural and all anthropogenic particles (including secondary organics and inorganic) resolved in size by using large number of bins (Menut et al., 2013) compared to RegCM, CNRM-RCSM or COSMO-MUSCAT (number of dust bins between 3 to 4 bins). Figure 28 reports the time evolution of simulated and observed AOD at 550 nm for the two sites (Ersa and Lampedusa) during the SOP-1a. Time correlation, as well as bias, is calculated after removing AERONET/PHOTONS data for the 27 June, strongly affected by smoke aerosols transported from Northern America biomass burning sources that are not included in the different domains. Figure 28 indicates that all models are able to simulate AOD in the range of magnitude of observations. For the dusty Lampedusa site, CNRM-RCSM and CHIMERE reveal high temporal correlations (0.82, 0.85, respectively), with standard deviations close to AERONET/PHOTONS data, especially for CHIMERE. For this station, COSMO-M and RegCM display moderate temporal correlation (0.55 and 0.49, respectively) compared to CNRM-RCSM and CHIMERE. As

ACPD
15, 19615–19727, 2015

already mentioned, one reason of lowest time-correlation for these models is related to the fact that they are only forced at the boundaries and the synoptic conditions inside the domain can derive during the simulation. This effect is limited for CNRM-RCSM that used the spectral nudging technique and for CHIMERE forced by WRF meteorological field (Menut et al., 2015). For each models, biases are shown to be low, both positive (for CNRM-RCSM and CHIMERE) and negative (for COSMO-M and RegCM).

For the Ersa station, less influenced by long-range transport of mineral dust during this period, temporal correlations are lowest and found to be moderate (0.40) for CHIMERE and COSMO-M and low for RegCM and CNRM-RCSM. In terms of bias, values are positive and low (0.02 to 0.04) for all models, except for COSMO-M (−0.07) that does not include anthropogenic aerosols nor sea-salt in the present simulation (Table 8). For each model, calculated standard deviations are in the same range of magnitude but slightly higher than observations, especially for RegCM (bias of 0.08) that simulated a large AOD for 19–20 June period. By comparison with the values obtained in Lampedusa, these low correlations at Ersa reveal the limitations of these models in terms of horizontal resolution with respect to the representativeness of the site. Lampedusa being isolated in the middle of the Mediterranean and under the main pathways of African mineral dust, AOD is mostly related to long-ranged transport. On the other hand, the site of Ersa in Corsica may be under several types of aerosols contributions (anthropogenic, biogenic, vegetation fires) more intense and more spatially variables than in Lampedusa. Ersa being closer to large industrial areas, the models with a horizontal resolution of tens of kilometers are probably not highly enough resolved to catch small scales aerosols plumes from the continent.

6.5.2 Regional SW 3-D direct radiative forcing

The SW (clear-sky) DRF, averaged for the SOP-1a period, has been estimated from the RegCM and CNRM-RCSM models, both at the surface and TOA, as shown in the Fig. 29. For this discussion, we only consider these two models as they estimate the clear-sky SW DRF by taking into account natural and anthropogenic aerosols, con-

ACPD
15, 19615–19727, 2015

trary to the COSMO-MUSCAT model in this study. At the surface first, one can observe the large regional dimming due to anthropogenic (especially over Europe) and natural (Northern Africa and Mediterranean) particles over the Euro-Mediterranean. Concerning the North African region, both models simulate large surface forcing $\sim -20\,W\,m^{-2}$ (with local maxima of $-50\,W\,m^{-2}$ associated with higher AOD). CNRM-RCSM is shown to simulate higher surface radiative forcing for the whole domain, especially over Algeria. Although such RCM climate models are not designed to simulate finely the size distribution and the chemical composition of aerosols as an A-Q system (Menut et al., 2013), a first estimate of the radiative effect of polluted particles over Europe is provided. Figure 29 displays a negative forcing, obviously lower than for mineral dust, of about -10 to $-15\,W\,m^{-2}$ for RegCM, especially over Balkans and no significant radiative effect over the Benelux region for this period. Over the continental region, CNRM-RCSM simulated a more diffuse surface forcing with values around $-10\,W\,m^{-2}$, including a large part of Europe (France, Benelux and Eastern Europe). As shown recently by Nabat et al. (2015a), this decrease in SW radiations due to aerosols could perturb the surface continental temperature, SST and latent heat fluxes over the Mediterranean Sea and more largely on meteorological fields.

At TOA, the dipole of the direct forcing between the North and the South of the domain is well reproduced by the two RCM systems with more intense values for CNRM-RCSM. One can clearly observe positive forcing at TOA (heating) over Northern Africa and negative forcing (cooling) over the Mediterranean and Europe. This represents one of the characteristics of the Euro-Mediterranean region with a large variability of surface albedo from the South (with higher values) to the North (low to moderate albedo). Due to this gradient, moderate absorbing dust aerosols emitted over Northern Africa first decrease the shortwave radiations at TOA, compared to a non-turbid atmosphere, and increase upward SW fluxes at TOA, when advected above low surface reflectance as marine or dense forest over Europe. One can see the transition between positive to negative TOA forcing that occurs over Northern Algeria and Morocco as soon as dust particles are transported over darker surfaces. This TOA radiative forcing gradient

ACPD
15, 19615–19727, 2015

is well captured by such RCM models which use a finer resolution than GCM. Over Europe and Mediterranean, the TOA forcing is simulated to be negative for both RCM with lower values around −5 to −10 $W m^{-2}$. The last important point to mention here concerns the fact that most of SW radiations losses at the surface are not completely compensated by fluxes reflected back to space. Hence, this gain of solar energy within dusty layers (due to moderate dust SW absorption, see Denjean et al., 2015) has been shown to result in significant feedbacks on the temperature and relative humidity profiles over the Mediterranean region with some important implications on its climate (Nabat et al., 2015a).

7 Conclusions

The special observing period (SOP-1a) performed during the Mediterranean dry season (11 June to 5 July 2013) over the western and central Mediterranean basins has been described in detail, as well as the 1-D to 3-D modeling effort, involved in the ChArMEx/ADRIMED project focused on aerosol-radiation-climate interactions. Details of the in-situ and remote-sensing instrumentation deployed at the different sites and the main meteorological conditions that occurred during the campaign have been provided. Some results from the in-situ and remote-sensing observations, vertical profiles, 1-D and 3-D aerosols direct radiative forcing (DRF) computations have also been presented. Concerning the aerosol loading during the SOP-1a, our results indicate that numerous but moderate mineral dust plumes were observed during the campaign with main sources located in Morocco, Algeria and Tunisia, leading to AOD between 0.1 to 0.6 (at 440 nm) over the western and central Mediterranean. Analysis of synoptic situations demonstrates unfavorable conditions to produce large concentrations of polluted-smoke particles during the SOP-1a but interesting sea-salt events have been observed.

Aerosol extinctions measured on-board the ATR-42 within the dust plume show local maxima reaching up to 150 Mm^{-1}. Non negligible aerosol extinctions (about 50 Mm^{-1})

ACPD
15, 19615–19727, 2015

have also been observed within the Marine Boundary Layer (MBL), due to the presence of polluted or marine aerosols. By combining ATR-42 extinction, absorption and scattering measurements, complete optical closures have been made revealing an excellent agreement in estimated optical properties. Associated calculations of the dust SSA have been conducted showing a moderate variability (from 0.90 to 1.00 at 530 nm) during the period of observations, corroborated by AERONET/PHOTONS SSA retrievals. Concerning the aerosol vertical structure, active remote-sensing observations, at the surface and onboard the F-20, indicate complex vertical profiles of particles with sea-salt and pollution located in the MBL, and mineral dust and/or even aged North American smoke particles located above (up to 6–7 km in altitude). Microphysical properties of aerosols measured onboard the ATR-42 aerosol observations for transported/aged mineral dust also reveal particle volume size distributions with diameters greater than 5 µm. Balloon observations revealed much larger particles (> 20 µm in diameter) within African dust layers. The analysis of the particle mass size distribution indicates that carbonaceous (BC and OC) aerosols are characterized by a bi-modal distribution, with two identified modes in the fine and coarse fraction.

In terms of shortwave (SW) and longwave (LW) DRF, in-situ surface and aircraft observations have been merged and used as inputs in different radiative transfer codes for calculating the 1-D DRF. Modeling results show significant surface (instantaneous) SW radiative forcing down to as much as $-90\,W\,m^{-2}$ over super-sites. In parallel, AOD together with surface radiative fluxes observations have also been used to directly estimate the local daily surface forcing in SW (and LW) spectral regions, showing a significant effect with values of $-15\,W\,m^{-2}$ ($+5.5\,W\,m^{-2}$) over Lampedusa. Associated 3-D modeling studies, using regional climate (RCM) and chemistry transport (CTM) models, indicate a relatively good agreement between simulated AOD and that determined from AERONET/PHOTONS data. Such models allow 3-D calculations of the daily SW DRF revealing a regional DRF of -10 to $-20\,W\,m^{-2}$ (at the surface and in clear-sky conditions), when averaged over the SOP-1a period. At TOA, a significant dipole in the DRF is estimated between the North and the South of the domain, with positive (heat-

ACPD
15, 19615–19727, 2015

ing) over Northern Africa and negative (cooling) DRF over the Mediterranean basin and Europe, reflecting changes in surface albedo associated to moderately absorbing aerosols.

This unprecedented dataset of aerosol microphysical, chemical, optical properties and vertical profiles obtained over the western Mediterranean will now be used for evaluating regional models to reproduce such properties. In addition to classical model evaluations based generally on the AOD, new comparisons between models and in-situ observations on aerosol absorbing (SSA and AAOD) properties and SW and LW heating rates, which control the semi-direct effect of aerosols, should be conducted. Comparisons will also be conducted on the aerosol size distribution for investigating the ability of regional models to simulate the observed large dust particle size during the transport over the Mediterranean, which could also be helpful for improving the representation of deposition in such models. In parallel, in-situ observations of sea-salt particles obtained at the surface and from ATR-42 measurements will also be used to evaluate the different primary sea-salt generation schemes, in terms of concentration and size distribution. The objective is to improve the representation of microphysical and optical properties of aerosols in regional climate models which will be used in multi-year simulations to assess the impact of natural and anthropogenic aerosols on climate in this region.

Acknowledgements. This research has received funding from the French National Research Agency (ANR) projects ADRIMED (contract ANR-11-BS56-0006). This work is part of the ChArMEx project supported by ADEME, CEA, CNRS-INSU and Météo-France through the multidisciplinary programme MISTRALS (Mediterranean Integrated Studies aT Regional And Local Scales). The station at Ersa was partly supported by the CORSiCA project funded by the Collectivité Territoriale de Corse through the Fonds Européen de Développement Régional of the European Operational Program 2007–2013 and the Contrat de Plan Etat Région. We acknowledge the AERONET/PHOTONS sun-photometer networks and the PIs of the selected stations and their staff for their work to produce the dataset used in this study. ACTRIS/EARLINET lidar measurements are supported by the 7th Framework Programme under the project ACTRIS (Aerosols, Clouds, and Trace Gases Research Infrastructure Network; grant agreement

ACPD
15, 19615–19727, 2015

no. 262 254) and ACTRIS-2 (grant agreement no. 654 109). Measurements at Lampedusa by ENEA were partly supported by the Italian Ministry for University and Research through the NextData and Ritmare Projects. This study, especially the balloon campaign and part of the aircraft operations has also been supported by the French space agency (CNES). The technical staff of SAFIRE, INSU Technical Division and the CNES Balloon sub-directorate (with special mention to Aurélien Bourdon and Gilles Dupouy) are warmly acknowledged for their contribution to the success of the experimental work. Contributions by Didier Bruneau (Latmos), Silvia Becagli (Univ. of Florence, Italy), Marco Cacciani (Univ. of Rome, Italy), Julian Groebner and Natalia Kouremeti (Physikalisch-Meteorologisches Observatorium Davos, World Radiation Center, Switzerland), and José Antonio Martinez Lozano (University of Valencia, Spain) are gratefully acknowledged. Granada station was partially supported by the Andalusian Regional Government through project P12-RNM-2409 and by the Spanish Ministry of Science and Technology through project CGL2013-45410-R. Sahar Hassazadeh, Constantino Munoz Porcar, and Santi Bertolin and Diego Lange are also acknowledged for their kind assistance in operating the Menorca surface station, as well as François Gheusi, Brice Barret, Flore Tocquer, and Yves Meyerfeld for their contribution to the balloon campaign preparation and/or deployment. Claude Basdevant, Alexis Doerenbecher, and Fabien Bernard are acknowledged for their help and very useful tools in support of our drifting balloon experiment.

References

Alados-Arboledas, L., Alcántara, A., Olmo, F. J., Martínez-Lozano, J. A., Estellés, V., Cachorro, V., Silva, A. M., Horvath, H., Gangl, M., Díaz, A., Pujadas, M., Lorente, J., Labajo, A., Sorribas, M., and Pavese, G.: Aerosol columnar properties retrieved from CIMEL radiometers during VELETA 2002, Atmos. Environ., 42, 2654–2667, 2008.

Ancellet, G., Pelon, J., Totems, J., Chazette, P., Bazureau, A., Sicard, M., Di Iorio, T., Dulac, F., and Mallet, M.: Mixing of aerosol sources during the North American biomass burning episode in summer 2013: analysis of lidar observations in the Mediterranean basin, Atmos. Chem. Phys. Discuss., in preparation, 2015.

Barragan, R., Sicard, M., Totems, J., Léon, J.-F., Renard, J.-B., Dulac, F., Mallet, M., Pelon, J., Alados-Arboledas, L., Amodeo, A., Augustin, P., Boselli, A., Bravo-Aranda, J. A., Burlizzi, P., Chazette, P., Comerón, A., D'Amico, G., Granados-Muñoz, M. J., Leto, G., Guerrero-

ACPD
15, 19615–19727, 2015

Rascado, J. L., Madonna, F., Mona, L., Muñoz-Porcar, C., Pappalardo, G., Perrone, M. R., Pont, V., Rocadenbosch, F., Rodriguez, A., Scollo, S., Spinelli, N., Titos, G., Wang, X., and Zanmar Sanchez, R.: Characterization of aerosol transport and ageing during a multi-intrusion Saharan dust event over the western and central Mediterranean Basin in June 2013 in the framework of the ADRIMED/ChArMEx campaign, Atmos. Chem. Phys. Discuss., in preparation, 2015.

Bessagnet, B., Hodzic, A., Vautard, R., Beekmann, M., Cheinet, S., Honoré, C., Liousse, C., and Rouil, L.: Aerosol modeling with CHIMERE: preliminary evaluation at the continental scale, Atmos. Environ., 38, 2803–2817, 2004.

Beuvier, J., Sevault, F., Herrmann, M., Kontoyiannis, H., Ludwig, W., Rixen, M., Stanev, E., Béranger, K., and Somot, S.: Modeling the Mediterranean Sea interannual variability during 1961–2000: Focus on the Eastern Mediterranean Transient, J. Geophys. Res., 115, C08017, doi:10.1029/2009JC005950, 2010.

Brauch, H. G.: Urbanization and natural disasters in the Mediterranean: population growth and climate change in the 21st century, in: Building Safer Cities – The Future of Disaster Risk, edited by: Kreimer, A., Arnold, M., and Carlin, A., The World Bank, Disaster Risk Management Series No. 3, 149–164, 2003.

Cachier, H., Aulagnier, F., Sarda, R., Gautier, F., Masclet, P., Besombes, J. L., Marchand, N., Despiau, S., Croci, D., Mallet, M., Laj, P., Marinoni, A., Deveau, P. A., Roger, J. C., Putaud, J. P., Van Dingenen, R., Dell'Acqua, A., Viidanoja, J., Martins-Dos Santos, S., Liousse, C., Cousin, F., and Rosset, R.: Aerosol studies during the ESCOMPTE Experiment: an overview, Atmos. Res., 74, 547–563, doi:10.1016/j.atmosres.2004.06.013, 2005.

Casasanta, G., di Sarra, A., Meloni, D., Monteleone, F., Pace, G., Piacentino, S., and Sferlazzo, D.: Large aerosol effects on ozone photolysis in the Mediterranean, Atmos. Environ., 45, 3937–3943, doi:10.1016/j.atmosenv.2011.04.065, 2011.

Chazette, P. and Liousse, C.: A case study of optical and chemical ground apportionment for urban aerosols in Thessaloniki, Atmos. Environ., 35, 2497–2506, doi:10.1016/S1352-2310(00)00425-8, 2001.

Chazette, P., Marnas, F., and Totems, J.: The mobile Water vapor Aerosol Raman LIdar and its implication in the framework of the HyMeX and ChArMEx programs: application to a dust transport process, Atmos. Meas. Tech., 7, 1629–1647, doi:10.5194/amt-7-1629-2014, 2014a.

ACPD
15, 19615–19727, 2015

Chazette, P., Marnas, F., Totems, J., and Shang, X.: Comparison of IASI water vapor retrieval with H_2O-Raman lidar in the framework of the Mediterranean HyMeX and ChArMEx programs, Atmos. Chem. Phys., 14, 9583–9596, doi:10.5194/acp-14-9583-2014, 2014b.

Chazette, P. et al.: Aerosol transport and optical properties over Menorca Island during the June 2013 ChArMEx/ADRIMED campaign, Atmos. Chem. Phys. Discuss., in preparation, 2015.

Chenoweth, J., Hadjinicolaou, P., Bruggemen, A., Lelieveld, J., Levin, Z., Lange, M. A., Xoplaki, E., and Hadkikakou, M.: Impact of climate change on the water resources of the eastern Mediterranean and middle east region: modeled 21st century, Water Resour. Res., 47, W06506, doi:10.1029/2010WR010269, 2011.

Ciardini, V., Di Iorio, T., Di Liberto, L., Tirelli, C., Casasanta, G., di Sarra, A., Fiocco, G., Fuà, D., and Cacciani, M.: Seasonal variability of tropospheric aerosols in Rome, Atmos. Res., 118, 205–214, doi:10.1016/j.atmosres.2012.06.026, 2012.

Claeys, M., Roberts, G., Mallet, M., Sellegri, K., Sciare, J., Tulet, P., Sauvage, B., and Arndt, J.: Characterisation of a sea salt episode during ADRIMED campaign: ageing, transport and size distribution study, Atmos. Chem. Phys. Discuss., in preparation, 2015.

Denjean, C., Chevaillier, S., Triquet, S., Grand, N., Cassola, F., Mazzino, A., Bourrianne, T., Momboisse, G., Dupuy, R., Sellegri, K., Schwarzenbock, A., Mallet, M., and Formenti, P.: Size distribution and optical properties of mineral dust aerosols transported in the West Mediterranean, Atmos. Chem. Phys. Discuss., in preparation, 2015.

Déqué, M. and Somot, S.: Extreme precipitation and high resolution with Aladin, Idöjaras Quaterly Journal of the Hungarian Meteorological Service, 112, 179–190, 2008.

Derimian, Y., Karnieli, A., Kaufman, Y. J., Andreae, M. O., Andreae, T. W., Dubovik, O., Maenhaut, W., Koren, I., and Holben, B. N.: Dust and pollution aerosols over the Negev desert, Israel: properties, transport, and radiative effect, J. Geophys. Res., 111, D05205, doi:10.1029/2005JD006549, 2006.

Deschamps, P.-Y., Bréon, F.-M., Leroy, M., Podaire, A., Brickaud, A., Buriez, J. C., and Sèze, G.: The POLDER mission: instrument characteristics and scientific objectives, IEEE Trans. Geosci. Remote Sens., 32, 598–615, 1994.

Di Biagio, C., di Sarra, A., Meloni, D., Monteleone, F., Piacentino, S., and Sferlazzo, D.: Measurements of Mediterranean aerosol radiative forcing and influence of the single scattering albedo, J. Geophys. Res., 114, D06211, doi:10.1029/2008JD011037, 2009.

ACPD
15, 19615–19727, 2015

Di Biagio, C., di Sarra, A., and D. Meloni, D.: Large atmospheric shortwave radiative forcing by Mediterranean aerosol derived from simultaneous ground-based and spaceborne observations, and dependence on the aerosol type and single scattering albedo, J. Geophys. Res., 115, D10209, doi:10.1029/2009JD012697, 2010.

Di Iorio, T., di Sarra, A., Sferlazzo, D. M., Cacciani, M., Meloni, D., Monteleone, F., Fuà, D., and Fiocco, G.: Seasonal evolution of the tropospheric aerosol vertical profile in the central Mediterranean and role of desert dust, J. Geophys. Res., 114, D02201, doi:10.1029/2008JD010593, 2009.

Di Iorio, T., Di Biagio, C., di Sarra, A., Formenti, P., Gomez Amo, J.-L., Meloni, D., and Pace, G.: Height resolved aerosol optical properties at Lampedusa during ADRIMED, Atmos. Chem. Phys. Discuss., in preparation, 2015.

di Sarra, A., Pace, G., Meloni, D., De Silvestri, L., Piacentino, S., and Monteleone, F.: Surface shortwave radiative forcing of different aerosol types in the central Mediterranean, Geophys. Res. Lett., 35, L02714, doi:10.1029/2007GL032395, 2008.

di Sarra, A., Di Biagio, C., Meloni, D., Monteleone, F., Pace, G., Pugnaghi, S., and Sferlazzo, D.: Shortwave and longwave radiative effects of the intense Saharan dust event of 25–26 March 2010 at Lampedusa (Mediterranean Sea), J. Geophys. Res., 116, D23209, doi:10.1029/2011JD016238, 2011.

di Sarra, A., Sferlazzo, D., Meloni, D., Anello, F., Bommarito, C., Corradini, S., De Silvestri, L., Di Iorio, T., Monteleone, F., Pace, G., Piacentino, S., and Pugnaghi, S.: Empirical correction of multi filter rotating shadowband radiometer (MFRSR) aerosol optical depths for the aerosol forward scattering and development of a long-term integrated MFRSR-Cimel dataset at Lampedusa, Appl. Optics, 54, 2725–2737, doi:10.1364/AO.54.002725, 2015.

Dubovik, O. and King, M. D.: A flexible inversion algorithm for retrieval of aerosol optical properties from Sun and sky radiance measurements, J. Geophys. Res., 105, 20673–20696, doi:10.1029/2000JD900282, 2000.

Dubovik, O., Smirnov, A., Holben, B. N., King, M. D., Kaufman, Y. J., Eck, T. F., and Slutsker, I.: Accuracy assessment of aerosol optical properties retrieval from AERONET Sun and sky radiance measurements, J. Geophys. Res., 105, 9791–9806, doi:10.1029/2000JD900040, 2000.

Dubovik, O., Holben, B., Eck, T. F., Smirnov, A., Kaufman, Y. J., King, M. D., Tanré, D., and Slutsker, I.: Variability of absorption and optical properties of key aerosol types

ACPD
15, 19615–19727, 2015

observed in worldwide locations, J. Atmos. Sci., 59, 590–608, doi:10.1175/1520-0469(2002)059<0590:VOAAOP>2.0.CO;2, 2002.
Dubovik, O., Sinyuk, A., Lapyonok, T., Holben, B. N., Mishchenko, M., Yang, P., Eck, T. F., Volten, H., Muñoz, O., Veihelmann, B., van der Zande, W. J., Léon, J.-F., Sorokin, M., and Slutsker, I.: Application of spheroid models to account for aerosol particle nonsphericity in remote sensing of desert dust, J. Geophys. Res., 111, D11208, doi:10.1029/2005JD006619, 2006.
Dubovik, O., Herman, M., Holdak, A., Lapyonok, T., Tanré, D., Deuzé, J. L., Ducos, F., Sinyuk, A., and Lopatin, A.: Statistically optimized inversion algorithm for enhanced retrieval of aerosol properties from spectral multi-angle polarimetric satellite observations, Atmos. Meas. Tech., 4, 975–1018, doi:10.5194/amt-4-975-2011, 2011.
Dubuisson, P., Dessailly, D., Vesperini, M., and Frouin, R.: Water vapor retrieval over ocean using near-infrared radiometry, J. Geophys. Res., 109, D19106, doi:10.1029/2004JD004516, 2004.
Ducrocq, V., Braud, I., Davolio, S., Ferretti, R., Flamant, C., Jansa, A., Kalthoff, N., Richard, E., Taupier-Letage, I., Ayral, P. A., Belamari, S., Berne, A., Borga, M., Boudevillain, B., Bock, O., Boichard, J. L., Bouin, M. N., Bousquet, O., Bouvier, C., Chiggiato, J., Cimini, D., Corsmeier, U., Coppola, L., Cocquerez, P., Defer, E., Delanoë, J., Delrieu, G., Di Girolamo, P., Doerenbecher, A., Drobinski, P., Dufournet, Y., Fourrié, N., Gourley, J. J., Labatut, L., Lambert, D., Le Coz, J., Marzano, F. S., Montani, A., Nuret, M., Ramage, K., Risøn, B., Roussot, O., Saïd, F., Schwarzenboeck, A., Testor, P., Van Baelen, J., Vincendon, B., Aran, M., and Tamayo, J.: HyMeX-SOP1, the field campaign dedicated to heavy precipitation and flash-flooding in northwestern Mediterranean. B. Am. Meteorol. Soc., 95, 1083–1100, doi:10.1175/BAMS-D-12-00244.1 and doi:10.1175/BAMS-D-12-00244.2, 2014.
Foltz, G. R. and McPhaden, M. J.: Impact of Saharan dust on tropical North Atlantic SST, J. Climate, 21, 5048–5060, doi:10.1175/2008JCLI2232.1, 2008.
Formenti, P., Boucher, O., Reiner, T., Sprung, D., Andreae, M. O., Wendisch, M., Wex, H., Kindred, D., Tzortziou, M., Vasaras, A., and Zerefos, C.: STAAARTE-MED 1998 summer airborne measurements over the Aegean Sea, 2. Aerosol scattering and absorption, and radiative calculations, J. Geophys. Res., 107, 4451, doi:10.1029/2001JD001536, 2002.
Fotiadi, A., Hatzianastassiou, N., Drakakis, E., Matsoukas, C., Pavlakis, K. G., Hatzidimitriou, D., Gerasopoulos, E., Mihalopoulos, N., and Vardavas, I.: Aerosol physical and optical

ACPD
15, 19615–19727, 2015

properties in the Eastern Mediterranean Basin, Crete, from Aerosol Robotic Network data, Atmos. Chem. Phys., 6, 5399–5413, doi:10.5194/acp-6-5399-2006, 2006.
Gangoiti, G., Millán, M., Salvador, R., and Mantilla, E.: Long-range transport and re-circulation of pollutants in the western Mediterranean during the project Regional Cycles of Air Pollution in the West-Central Mediterranean Area, Atmos. Environ., 35, 6267–6276, doi:10.1016/S1352-2310(01)00440-X, 2001.
García, O. E., Díaz, J. P., Expósito, F. J., Díaz, A. M., Dubovik, O., Derimian, Y., Dubuisson, P., and Roger, J.-C.: Shortwave radiative forcing and efficiency of key aerosol types using AERONET data, Atmos. Chem. Phys., 12, 5129–5145, doi:10.5194/acp-12-5129-2012, 2012.
García-Ruiz, J. M., López-Moreno, J. I., Vicente-Serrano, S. M., Lasanta–Martínez, T., and Beguería, S.: Mediterranean water resources in a global change scenario, Earth-Sci. Rev., 105, 121–139, doi:10.1016/j.earscirev.2011.01.006, 2011.
Gard, E., Mayer, J. E., Morrical, B. D., Dienes, T., Fergenson, D. P., and Prather., K. A.: Real-time analysis of individual atmospheric aerosol particles: design and performance of a portable ATOFMS, Anal. Chem., 69, 4083–4091, doi:10.1021/ac970540n, 1997.
Gerasopoulos, E., Andreae, M. O., Zerefos, C. S., Andreae, T. W., Balis, D., Formenti, P., Merlet, P., Amiridis, V., and Papastefanou, C.: Climatological aspects of aerosol optical properties in Northern Greece, Atmos. Chem. Phys., 3, 2025–2041, doi:10.5194/acp-3-2025-2003, 2003.
Gheusi, F., Durand, P., Verdier, N., Dulac, F., Attié, J.-L., Commun, P., Barret, B., Basdevant, C., Clenet, A., Doerenbecher, A., Fontaine, A., Jambert, C., Meyerfeld, Y., Roblou, L., and Tocquer, F.: Modified ECC ozone sonde for long-duration flights aboard boundary-layer pressurized balloons, Atmos. Meas. Tech. Discuss., in preparation, 2015.
Gimeno, L., Drumond, A., Nieto, R., Trigo, R. M., and Stohl, A.: On the origin of continental precipitation, Geophys. Res. Lett., 37, L13804, doi:10.1029/2010GL043712, 2010.
Giorgi, F. and Lionello, P.: Climate change projections for the Mediterranean region, Global Planet. Change, 63, 90–104, doi:10.1016/j.gloplacha.2007.09.005, 2008.
Giorgi, F., Coppola, E., Solmon, F., Mariotti, L., Sylla, M. B., Bi, X., Elguindi, N., Diro, G. T., Nair, V., Giuliani, G., Turuncoglu, U. U., Cozzini, S., Guttler, I., O'Brien, T. A., Tawfik, A. B., Shalaby, A., Zakey, A. S., Steiner, A. L., Stordal, F., Sloan, L. C., and Brankovic, C.: RegCM4: Model description and preliminary tests over multiple CORDEX domains, Clim. Res., 52, 7–29, doi:10.3354/cr01018, 2012.

ACPD
15, 19615–19727, 2015

Gross, D. S., Atlas, R., Rzeszotarski, J., Turetsky, E., Christensen, J., Benzaid, S., Olson, J., Smith, T., Steinberg, L., and Sulman, J.: Environmental chemistry through intelligent atmospheric data analysis, Environ. Modell. Softw., 25, 760–769, doi:10.1016/j.envsoft.2009.12.001, 2010.

Guenther, A., Karl, T., Harley, P., Wiedinmyer, C., Palmer, P. I., and Geron, C.: Estimates of global terrestrial isoprene emissions using MEGAN (Model of Emissions of Gases and Aerosols from Nature), Atmos. Chem. Phys., 6, 3181–3210, doi:10.5194/acp-6-3181-2006, 2006.

Hashimoto, M., Nakajima, T., Dubovik, O., Campanelli, M., Che, H., Khatri, P., Takamura, T., and Pandithurai, G.: Development of a new data-processing method for SKYNET sky radiometer observations, Atmos. Meas. Tech., 5, 2723–2737, doi:10.5194/amt-5-2723-2012, 2012.

Hatzianastassiou, N., Gkikas, A., Mihalopoulos, N., Torres, O., and Katsoulis, B. D.: Natural versus anthropogenic aerosols in the eastern Mediterranean basin derived from multiyear TOMS and MODIS satellite data, J. Geophys. Res., 114, D24202, doi:10.1029/2009JD011982, 2009.

Healy, R. M., Hellebust, S., Kourtchev, I., Allanic, A., O'Connor, I. P., Bell, J. M., Healy, D. A., Sodeau, J. R., and Wenger, J. C.: Source apportionment of $PM_{2.5}$ in Cork Harbour, Ireland using a combination of single particle mass spectrometry and quantitative semi-continuous measurements, Atmos. Chem. Phys., 10, 9593–9613, doi:10.5194/acp-10-9593-2010, 2010.

Holben, B. N., Eck, T. F., Slutsker, I., Tanré, D., Buis, J. P., Setzer, A., Vermote, E., Reagan, J. A., Kaufman, Y. J., Nakajima, T., Lavenu, F., Jankowiak, I., and Smirnov, A.: AERONET – a federated instrument network and data archive for aerosol characterization, Remote Sens. Environ., 66, 1–16, doi:10.1016/S0034-4257(98)00031-5, 1998.

Horvath, H., Alados Arboledas, L., Olmo, F. J., Jovanovic, O., Gangl, M., Sanchez, C., Sauerzopf, H., and Seidl, S.: Optical characteristics of the aerosol in Spain and Austria and its effect on radiative forcing, J. Geophys. Res., 107, 4386, doi:10.1029/2001JD001472, 2002.

Johnson, G., Ristovski, Z., and Morawska, L.: Application of the VH-TDMA technique to coastal ambient aerosols, Geophys. Res. Lett., 31, L16105, doi:10.1029/2004GL020126, 2004.

Kok, J. F.: A scaling theory for the size distribution of emitted dust aerosols suggests climate models underestimate the size of the global dust cycle, P. Natl. Acad. Sci. USA, 108, 1016–1021, doi:10.1073/pnas.1014798108, 2011.

ACPD
15, 19615–19727, 2015

Kumar, D., Rocadenbosch, F., Sicard, M., Comeron, A., Muñoz, C., Lange, D., Tomás, S., and Gregorio, E.: Six-channel polychromator design and implementation for the UPC elastic/Raman LIDAR, in: SPIE Remote Sens., Int. Soc. Opt. Photon., Prague, Czech Republic, 81820W–81820W, 2011.

Lelieveld, J., Berresheim, H. Borrmann, S., Crutzen, P. J., Dentener, F. J., Fischer, H., Feichter, J., Flatau, P. J., Heland, J., Holzinger1, R., Korrmann, R., Lawrence, M. G., Levin, Z., Markowicz, K. M., Mihalopoulos, N., Minikin, A. Ramanathan, V., de Reus, M., Roelofs, G. J. Scheeren, H. A., Sciare, J., Schlager, H., Schultz, M., Siegmund, P., Steil, B., Stephanou, E. G., Stier, P., Traub, M., Warneke, C., Williams, J., and Ziereis, H.: Global air pollution crossroads over the Mediterranean, Science, 298, 794–799, doi:10.1126/science.1075457, 2002.

Léon, J.-F., Augustin, P., Mallet, M., Bourrianne, T., Pont, V., Dulac, F., Fourmentin, M., Lambert, D., and Sauvage, B.: Aerosol vertical distribution, optical properties and transport over Corsica (western Mediterranean), Atmos. Chem. Phys. Discuss., 15, 9507–9540, doi:10.5194/acpd-15-9507-2015, 2015.

Lionello, P., Malanotte-Rizzoli, P., Boscolo, R., Alpert, P., Artale, V., Li, L., Luterbacher, J., May, W., Trigo, R., Tsimplis, M., Ulbrich, U., and Xoplaki, E: The Mediterranean climate: an overview of the main characteristics and issues, in: The Mediterranean Climate Variability, edited by: Lionello, P., Malanotte-Rizzoli, P., and Boscolo, R., Developments in Earth and Environmental Sciences, 4, Elsevier, 1–26, 2006.

Madonna, F., Amodeo, A., Boselli, A., Cornacchia, C., Cuomo, V., D'Amico, G., Giunta, A., Mona, L., and Pappalardo, G.: CIAO: the CNR-IMAA advanced observatory for atmospheric research, Atmos. Meas. Tech., 4, 1191–1208, doi:10.5194/amt-4-1191-2011, 2011.

Mailler, S., Menut, L., di Sarra, A. G., Becagli, S., Di Iorio, T., Formenti, P., Bessagnet, B., Briant, Régis, Luis Gómez-Amo, J., Mallet, M., Rea, Géraldine, Siour, G., Sferlazzo, D. M., Traversi, R., Udisti, R., and Turquety, S.: On the radiative impact of aerosols on photolysis rates: comparison of simulations and observations in the Lampedusa island during the ChArMEx/ADRIMED campaign, Atmos. Chem. Phys. Discuss., 15, 7585–7643, doi:10.5194/acpd-15-7585-2015, 2015.

Mallet, M., Roger, J. C., Despiau, S., Dubovik, O., and Putaud, J. P.: Microphysical and optical properties of aerosol particles in urban zone during ESCOMPTE, Atmos. Res., 69, 73–97, doi:10.1016/j.atmosres.2003.07.001, 2003.

ACPD
15, 19615–19727, 2015

Mallet, M., Pont, V., Liousse, C., Roger, J. C., and Dubuisson, P.: Simulation of aerosol radiative properties with the ORISAM-RAD model during a pollution event (ESCOMPTE 2001), Atmos. Environ., 40, 7696–7705, doi:10.1016/j.atmosenv.2006.08.031, 2006.

Mallet, M., Gomes, L., Solmon, F., Sellegri, K., Pont, V., Roger, J. C., Missamou, T., and Piazzola, J.: Calculations of key optical properties over the main anthropogenic aerosols over the Western French coastal Mediterranean Sea, Atmos. Res., 101, 396–411, doi:10.1016/j.atmosres.2011.03.008, 2011.

Mallet, M., Dubovik, O., Nabat, P., Dulac, F., Kahn, R., Sciare, J., Paronis, D., and Léon, J. F.: Absorption properties of Mediterranean aerosols obtained from multi-year ground-based remote sensing observations, Atmos. Chem. Phys., 13, 9195–9210, doi:10.5194/acp-13-9195-2013, 2013.

Markowicz, K. M., Flatau, P. J., Ramana, M. V., Crutzen, P. J., and Ramanathan, V.: Absorbing Mediterranean aerosols lead to a large reduction in the solar radiation at the surface, Geophys. Res. Lett., 29, 1968, doi:10.1029/2002GL015767, 2002.

Mariotti, A., Zeng, N., Yoon, J., Artale, V., Navarra, A., Alpert, P., and Li, L. Z. X.: Mediterranean water cycle changes: transition to drier 21st century conditions in observations and CMIP3 simulations, Environ. Res. Lett., 3, 044001, doi:10.1088/1748-9326/3/4/044001, 2008.

Mariotti, A., Pan, Y., Zeng, N., and Alessandri, A.: Long-term climate change in the Mediterranean region in the midst of decadal variability, Clim. Dynam., 44, 1437–1456, doi:10.1007/s00382-015-2487-3, 2015.

Marticorena, B. and Bergametti, G.: Modeling the atmospheric dust cycle 1. Design of a soil-derived dust production scheme, J. Geophys. Res., 100, 16415–16430, 1995.

McConnell, C. L., Formenti, P., Highwood, E. J., and Harrison, M. A. J.: Using aircraft measurements to determine the refractive index of Saharan dust during the DODO Experiments, Atmos. Chem. Phys., 10, 3081–3098, doi:10.5194/acp-10-3081-2010, 2010.

Meloni, D., Di Sarra, A., DeLuisi, J., Di Iorio, T., Fiocco, G., Junkermann, W., and Pace, G.: Tropospheric aerosols in the Mediterranean: 2. Radiative effects through model simulations and measurements, J. Geophys. Res., 108, 4317, doi:10.1029/2002JD002807, 2003.

Meloni, D., Di Sarra, A. Di Iorio, T., and Fiocco, G.: Direct radiative forcing of Saharan dust in the Mediterranean from measurements at Lampedusa Island and MISR space-borne observations, J. Geophys. Res., 109, D08206, doi:10.1029/2003JD003960, 2004.

ACPD
15, 19615–19727, 2015

Meloni, D., Di Sarra, A., Monteleone, F., Pace, G., Piacention, S., and Sferlazzo, D. M.: Seasonal transport patterns of intense dust events at the Mediterranean island of Lampedusa, Atmos. Res., 88, 134–148, doi:10.1016/j.atmosres.2007.10.007, 2008.

Meloni, D., Junkermann, W., di Sarra, A., Cacciani, M., De Silvestri, L., Di Iorio, T., Estellés, V., Gómez-Amo, J. L., Pace, G., and Sferlazzo, D. M.: Altitude-resolved shortwave and longwave radiative effects of desert dust in the Mediterranean during the GAMARF campaign: indications of a net daily cooling in the dust layer, J. Geophys. Res.-Atmos., 120, doi:10.1002/2014JD022312, 2015.

Meloni, M., di Sarra, A., Brogniez, G., Denjean, C., De Silvestri, L., Di Iorio, T., Formenti, P., Gomez-Amo, J.-L., Gröbner, J., Kouremeti, N., Mallet, M., and Pace., G.: Simulating vertically resolved SW and LW irradiances and infrared brightness temperatures measured at Lampedusa during the Charmex/ADRIMED campaign, in preparation, 2015.

Menut, L., Bessagnet, B., Khvorostyanov, D., Beekmann, M., Blond, N., Colette, A., Coll, I., Curci, G., Foret, G., Hodzic, A., Mailler, S., Meleux, F., Monge, J.-L., Pison, I., Siour, G., Turquety, S., Valari, M., Vautard, R., and Vivanco, M. G.: CHIMERE 2013: a model for regional atmospheric composition modelling, Geosci. Model Dev., 6, 981–1028, doi:10.5194/gmd-6-981-2013, 2013.

Menut, L., Mailler, S., Siour, G., Bessagnet, B., Turquety, S., Rea, G., Briant, R., Mallet, M., Sciare, J., Formenti, P., and Meleux, F.: Ozone and aerosol tropospheric concentrations variability analyzed using the ADRIMED measurements and the WRF and CHIMERE models, Atmos. Chem. Phys., 15, 6159–6182, doi:10.5194/acp-15-6159-2015, 2015.

Millán, M. M., Salvador, R., Mantilla, E., and Kallos, G.: Photooxidant dynamics in the Mediterranean basin in summer: results from European research projects, J. Geophys. Res., 102, 8811–8823, doi:10.1029/96JD03610, 1997.

Mulcahy, J. P., O'Dowd, C. D., Jennings, S. G., and Ceburnis, D.: Significant enhancement of aerosol optical depth in marine air under high wind conditions, Geophys. Res. Lett., 35, L16810, doi:10.1029/2008GL034303, 2008.

Nabat, P., Solmon, F., Mallet, M., Kok, J. F., and Somot, S.: Dust emission size distribution impact on aerosol budget and radiative forcing over the Mediterranean region: a regional climate model approach, Atmos. Chem. Phys., 12, 10545–10567, doi:10.5194/acp-12-10545-2012, 2012.

Nabat, P., Somot, S., Mallet, M., Chiapello, I., Morcrette, J. J., Solmon, F., Szopa, S., Dulac, F., Collins, W., Ghan, S., Horowitz, L. W., Lamarque, J. F., Lee, Y. H., Naik, V., Nagashima, T.,

ACPD
15, 19615–19727, 2015

Shindell, D., and Skeie, R.: A 4-D climatology (1979–2009) of the monthly tropospheric aerosol optical depth distribution over the Mediterranean region from a comparative evaluation and blending of remote sensing and model products, Atmos. Meas. Tech., 6, 1287–1314, doi:10.5194/amt-6-1287-2013, 2013.

Nabat, P., Somot, S., Mallet, M., Sanchez-Lorenzo, A., and Wild, M., Contribution of anthropogenic sulfate aerosols to the changing Euro-Mediterranean climate since 1980, Geophys. Res. Lett., 41, 5605–5611, doi:10.1002/2014GL060798, 2014.

Nabat, P., Somot, S., Mallet, M., Sevault, F., Chiacchio, M., and Wild, M.: Direct and semi-direct aerosol radiative effect on the Mediterranean climate variability using a coupled regional climate system model, Clim. Dynam., 44, 1127–1155, doi:10.1007/s00382-014-2205-6, 2015a.

Nabat, P., Somot, S., Mallet, M., Michou, M., Sevault, F., Driouech, F., Meloni, D., di Sarra, A., Di Biagio, C., Formenti, P., Sicard, M., Léon, J.-F., and Bouin, M.-N.: Dust aerosol radiative effects during summer 2012 simulated with a coupled regional aerosol–atmosphere–ocean model over the Mediterranean, Atmos. Chem. Phys., 15, 3303–3326, doi:10.5194/acp-15-3303-2015, 2015b.

Nicolas, J., Mallet, M., Roberts, G., Denjean, C., Formenti, P., Fresney, E., Sellegri, K., Borgniez, G., Bourrianne, T., Piguet, B., Torres, B., Dubuisson, P., and Dulac, F.: Aerosol direct radiative forcing at a regional scale over the western Mediterranean in summer within the ADRIMED project: airborne observations compared to GAME simulations, Atmos. Chem. Phys. Discuss., in preparation, 2015.

Noilhan, J. and Mahfouf, J.-F.: The ISBA land surface parameterisation scheme, Global Planet. Change, 13, 145–159, doi:10.1016/0921-8181(95)00043-7, 1996.

Otto, S., Bierwirth, E., Weinzierl, B., Kandler, K., Esselborn, M., Tesche, M., Schladitz, A.,Wendisch, M., and Trautmann, T.: Solar radiative effects of a Saharan dust plume observed during SAMUM assuming spheroidal model particles, Tellus B, 61, 270– 296, doi:10.1111/j.1600-0889.2008.00389.x, 2009.

Pace, G., Meloni, D., and di Sarra, A.: Forest fire aerosol over the Mediterranean basin during summer 2003, J. Geophys. Res., 110, D21202, doi:10.1029/2005JD005986, 2005.

Papadimas, C. D., Hatzianastassiou, N., Matsoukas, C., Kanakidou, M., Mihalopoulos, N., and Vardavas, I.: The direct effect of aerosols on solar radiation over the broader Mediterranean basin, Atmos. Chem. Phys., 12, 7165–7185, doi:10.5194/acp-12-7165-2012, 2012.

ACPD
15, 19615–19727, 2015

Pappalardo, G., Amodeo, A., Apituley, A., Comeron, A., Freudenthaler, V., Linné, H., Ansmann, A., Bösenberg, J., D'Amico, G., Mattis, I., Mona, L., Wandinger, U., Amiridis, V., Alados-Arboledas, L., Nicolae, D., and Wiegner, M.: EARLINET: towards an advanced sustainable European aerosol lidar network, Atmos. Meas. Tech., 7, 2389–2409, doi:10.5194/amt-7-2389-2014, 2014.

Pelon, J., Ancellet, G., Totems, J., Denjean, C., Formenti, P., Chazette, P., Dulac, F., Mallet, M., Di Iorio, T., and Sicard, M., Characterization of radiative properties of Long-range transported biomass burning aerosols over the western Mediterranean basin during ADRIMED-CHARMEX using airborne, ground-based and satellite observations, Atmos. Chem. Phys. Discuss., in preparation, 2015.

Péré, J. C., M. Mallet, V. Pont and Bessagnet, B., Impact of aerosol direct radiative forcing on the radiative budget, surface heat fluxes, and atmospheric dynamics during the heat wave of summer 2013 over western Europe: a modelling study, J. Geophys. Res., 116, D23119, doi:10.1029/2011JD016240, 2011.

Ramanathan, V., Crutzen, P. J., Lelieveld, J., Mitra, A. P., Althausen, D., Anderson, J., Andreae, M. O., Cantrell, W., Cass, G., Chung, C. E., Clarke, A. D., Coakley, J. A., Collins, W. D., Conant, W. C., Dulac, F., Heintzenberg, J., Heymsfield, A. J., Holben, B., Howell, S., Hudson, J., Jayaraman, A., Kiehl, J. T., Krishnamurti, T. N., Lubin, D., MacFarquhar, G., Novakov, T., Ogren, J. A., Podgorny, I. A., Prather, K., Priestley, K., Prospero, J. M., Quinn, P. K., Rajeev, K., Rasch, P., Rupert, S., Sadourny, R., Satheesh, S.K., Shaw, G. E., Sheridan, P., and Valero, F. P. J.: Indian Ocean experiment: an integrated analysis of the climate forcing and effects of the great Indo-Asian haze, J. Geophys. Res., 106, 28371–28398, doi:10.1029/2001JD900133, 2001.

Rea, G., Turquety, S., Menut, L., Briant, R., Mailler, S., and Siour, G.: Source contributions to 2012 summertime aerosols in the Euro-Mediterranean region, Atmos. Chem. Phys. Discuss., 15, 8191–8242, doi:10.5194/acpd-15-8191-2015, 2015.

Renard, J.-B., Dulac, F., Berthet, G., Lurton, T., Vignelles, D., Jégou, F., Tonnelier, T., Thaury, C., Jeannot, M., Couté, B., Akiki, R., Mineau, J.-L., Verdier, N., Mallet, M., Gensdarmes, F., Charpentier, P., Mesmin, S., Duverger, V., Dupont, J.-C., Elias, T., Crenn, V., Sciare, J., Giacomoni, J., Gobbi, M., Hamonou, E., Olafsson, H., Dagsson-Waldhauserova, P., Camy-Peyret, C., Mazel, C., Décamps, T., Piringer, M., Surcin, J., and Daugeron, D.: LOAC: a small aerosol optical counter/sizer for ground-based and balloon measurements of the size distribution and nature of atmospheric particles – Part 1: Principle of measurements and in-

ACPD
15, 19615–19727, 2015

strument evaluation, Atmos. Meas. Tech. Discuss., 8, 1203–1259, doi:10.5194/amtd-8-1203-2015, 2015a.
Renard, J.-B., Dulac, F., Berthet, G., Lurton, T., Vignelle, D., Jégou, F., Tonnelier, T., Thaury, C., Jeannot, M., Couté, B., Akiki, R., Mineau, J.-L., Verdier, N., Mallet, M., Gensdarmes, F., Charpentier, P., Mesmin, S., Duverger, V., Dupont, J.-C., Elias, T., Crenn, V., Sciare, J., Giacomoni, J., Gobbi, M., Hamonou, E., Olafsson, H., Dagsson-Waldhauserova, P., Camy-Peyret, C., Mazel, C., Décamps, T., Piringer, M., Surcin, J., and Daugeron, D.: LOAC: a small aerosol optical counter/sizer for ground-based and balloon measurements of the size distribution and nature of atmospheric particles – Part 2: First results from balloon and unmanned aerial vehicle flights, Atmos. Meas. Tech. Discuss., 8, 1261–1299, doi:10.5194/amtd-8-1261-2015, 2015b.
Roger, J. C., Mallet, M., Dubuisson, P., Cachier, H., Vermote, E., Dubovik, O., and Despiau, S., A synergetic approach for estimating the local direct aerosol forcing: application to an urban zone during the Experience sur Site pour Contraindre les Modèles de Pollution et de Transport d'Emission (ESCOMPTE) experiment, J. Geophys. Res., 111, D13208, doi:10.1029/2005JD006361, 2006.
Royer, P., Raut, J.-C., Ajello, G., Berthier, S., and Chazette, P.: Synergy between CALIOP and MODIS instruments for aerosol monitoring: application to the Po Valley, Atmos. Meas. Tech., 3, 893–907, doi:10.5194/amt-3-893-2010, 2010.
Ryder, C. L., Highwood, E. J., Rosenberg, P. D., Trembath, J., Brooke, J. K., Bart, M., Dean, A., Crosier, J., Dorsey, J., Brindley, H., Banks, J., Marsham, J. H., McQuaid, J. B., Sodemann, H., and Washington, R.: Optical properties of Saharan dust aerosol and contribution from the coarse mode as measured during the Fennec 2011 aircraft campaign, Atmos. Chem. Phys., 13, 303–325, doi:10.5194/acp-13-303-2013, 2013.
Saha, A., Mallet, M., Roger, J. C., Dubuisson, P. Piazzola, J., and Despiau, S.: One year measurements of aerosol optical properties over an urban coastal site: effect on local direct radiative forcing, Atmos. Res., 90, 195–202, doi:10.1016/j.atmosres.2008.02.003, 2008.
Sanchez-Gomez, E., Somot, S., and Mariotti, A.: Future changes in the Mediterranean water budget projected by an ensemble of regional climate models, Geophys. Res. Lett., 36, L21401, doi:10.1029/2009GL040120, 2009.
Salameh, T., Drobinski, P., Menut, L., Bessagnet, B., Flamant, C., Hodzic, A., and Vautard, R.: Aerosol distribution over the western Mediterranean basin during a Tramontane/Mistral event, Ann. Geophys., 25, 2271–2291, doi:10.5194/angeo-25-2271-2007, 2007.

ACPD
15, 19615–19727, 2015

Santese, M., Perrone, M. R., Zakey, A. S., De Tomasi, F., and Giorgi, F.: Modeling of Saharan dust outbreaks over the Mediterranean by RegCM3: case studies, Atmos. Chem. Phys., 10, 133–156, doi:10.5194/acp-10-133-2010, 2010.

Sassen, K.: Lidar backscatter depolarization technique for cloud and aerosol research, in: Light Scattering by Nonspherical Particles: Theory, Measurements, and Applications, edited by: Mishchenko, M., Hovenier, J. W., and Travis, L. D., Academic Press, 393–417, 1999.

Schepanski, K., Tegen, I., Laurent, B., Heinold, B., and Macke, A.: A new Saharan dust source activation frequency map derived from MSG-SEVIRI IR-channels, Geophys. Res. Lett., 34, 18803, doi:10.1029/2007GL030168, 2007.

Sciare, J., Cachier, H., Oikonomou, K., Ausset, P., Sarda-Estève, R., and Mihalopoulos, N.: Characterization of carbonaceous aerosols during the MINOS campaign in Crete, July–August 2001: a multi-analytical approach, Atmos. Chem. Phys., 3, 1743–1757, doi:10.5194/acp-3-1743-2003, 2003.

Sciare, J., Oikonomou, K., Favez, O., Liakakou, E., Markaki, Z., Cachier, H., and Mihalopoulos, N.: Long-term measurements of carbonaceous aerosols in the Eastern Mediterranean: evidence of long-range transport of biomass burning, Atmos. Chem. Phys., 8, 5551–5563, doi:10.5194/acp-8-5551-2008, 2008.

Schicker, I., Radanovics, S., and Seibert, P.: Origin and transport of Mediterranean moisture and air, Atmos. Chem. Phys., 10, 5089–5105, doi:10.5194/acp-10-5089-2010, 2010.

Schroeder, W., Csiszar, I., Giglio, L., and Schmidt, C. C.: On the use of fire radiative power, area, and temperature estimates to characterize biomass burning via moderate to coarse spatial resolution remote sensing data in the Brazilian Amazon, J. Geophys. Res., 115, D21121, doi:10.1029/2009JD013769, 2010.

Sellegri, K., Rose, C., Culot, A., Sauvage, S., Roberts, G., Marchand, N., Pey, J., Sciare, J., Bourriane, T., Mallet, M., and Dulac, F.: Spatial extend, occurrence and precursors of nucleation events over the western mediterranean bassin, in preparation, 2015.

Sicard, M., Pérez, C., Rocadenbosch, F., Baldasano, J. M., and García-Vizcaino, D.: Mixed-layer depth determination in the Barcelona coastal area from regular lidar measurements: methods, results and limitations, Bound.-Lay. Meteorol., 119, 135–157, doi:10.1007/s10546-005-9005-9, 2006.

Sicard, M., Rocadenbosch, F., Reba, M. N. M., Comerón, A., Tomás, S., García-Vízcaino, D., Batet, O., Barrios, R., Kumar, D., and Baldasano, J. M.: Seasonal variability of aerosol optical

ACPD
15, 19615–19727, 2015

properties observed by means of a Raman lidar at an EARLINET site over Northeastern Spain, Atmos. Chem. Phys., 11, 175–190, doi:10.5194/acp-11-175-2011, 2011.

Sicard, M., Bertolín, S., Mallet, M., Dubuisson, P., and Comerón, A.: Estimation of mineral dust long-wave radiative forcing: sensitivity study to particle properties and application to real cases in the region of Barcelona, Atmos. Chem. Phys., 14, 9213–9231, doi:10.5194/acp-14-9213-2014, 2014a.

Sicard, M., Bertolín, S., Muñoz, C., Rodríguez, A., Rocadenbosch, F., and Comerón, A.: Separation of aerosol fine- and coarse-mode radiative properties: effect on the mineral dust long-wave, direct radiative forcing, Geophys. Res. Lett., 41, doi:10.1002/2014GL060946, 2014b.

Sicard, M., Totems, J., Barragan, R., Léon, J.-F., Dulac, F., Mallet, M., Comerón, A., Alados-Arboledas, L., Augustin, P., Chazette, P., Olmo, F. J., Pont, V., Renard, J.-B., Rocadenbosch, F.: Aerosol optical, microphysical and ratiative properties at three regional background insular sites in the western Mediterranean Basin, Atmos. Chem. Phys. Discuss., in preparation, 2015.

Solmon, F., Giorgi., F., and Liousse, C.: Aerosol modelling for regional climate studies: application to anthropogenic particles and evaluation over a European/African domain, Tellus B, 58, 51–72, doi:10.1111/j.1600-0889.2005.00155.x, 2006.

Solmon. F., Mallet., M., Elguindi., N., Giorgi., F., Zakey., A., and Konaré, A.: Dust aerosol impact on regional precipitation over western Africa: mechanisms and sensitivity to absorption properties, Geophys. Res. Lett., 35, L24705, doi:10.1029/2008GL035900, 2008.

Spada, M., Jorba, O., Pérez García-Pando, C., Janjic, Z., and Baldasano, J. M.: Modeling and evaluation of the global sea-salt aerosol distribution: sensitivity to size-resolved and sea-surface temperature dependent emission schemes, Atmos. Chem. Phys., 13, 11735–11755, doi:10.5194/acp-13-11735-2013, 2013.

Tafuro, A. M., Kinne, S., De Tomasi, F., and Perrone, M. R.: Annual cycle of aerosol direct radiative effect over southeast Italy and sensitivity studies, J. Geophys. Res., 112, D20202, doi:10.1029/2006JD008265, 2007.

Tegen, I., Harrison, S. P., Kohfeld, K. E., and Prentice, I. C.: Impact of vegetation and preferential source areas on global dust aerosol: results from a model study, J. Geophys. Res., 107, 4576, doi:10.1029/2001JD000963, 2002.

Torres, B., Dubovik, O., Fuertes, D., Lapyonok, T., Toledano, C., Schuster, G. L., Goloub, P., Blarel, L., Barreto, A., Mallet, M., and Tanré, D.: Advanced characterization of aerosol prop-

ACPD
15, 19615–19727, 2015

erties from measurements of spectral optical thickness of the atmosphere, in preparation, 2015.
Turco, M., Llasat, M. C., Tudela, A., Castro, X., and Provenzale, A.: Brief communication Decreasing fires in a Mediterranean region (1970–2010, NE Spain), Nat. Hazards Earth Syst. Sci., 13, 649–652, doi:10.5194/nhess-13-649-2013, 2013.
Turquety, S., Menut, L., Bessagnet, B., Anav, A., Viovy, N., Maignan, F., and Wooster, M.: APIFLAME v1.0: high-resolution fire emission model and application to the Euro-Mediterranean region, Geosci. Model Dev., 7, 587–612, doi:10.5194/gmd-7-587-2014, 2014.
Ramanathan, V., Crutzen, P. J., Lelieveld, J., Mitra, A. P., Althausen, D., Anderson, J., Andreae, M. O., Cantrell, W., Cass, G., Chung, C. E., Clarke, A. D., Coakley, J. A., Collins, W. D., Conant, W. C., Dulac, F., Heintzenberg, J., Heymsfield, A. J., Holben, B., Howell, S., Hudson, J., Jayaraman, A., Kiehl, J. T., Krishnamurti, T. N., Lubin, D., MacFarquhar, G., Novakov, T., Ogren, J. A., Podgorny, I. A., Prather, K., Priestley, K., Prospero, J. M., Quinn, P. K., Rajeev, K., Rasch, P., Rupert, S., Sadourny, R., Satheesh, S. K., Shaw, G. E., Sheridan, P., and Valero, F. P. J.: Cirene: air–sea interactions in the Seychelles-Chagos thermocline ridge region, B. Am. Meteorol. Soc., 90, 45–61, doi:10.1175/2008BAMS2499.1, 2009.
Waquet, F., Cornet, C., Deuzé, J.-L., Dubovik, O., Ducos, F., Goloub, P., Herman, M., Lapyonok, T., Labonnote, L. C., Riedi, J., Tanré, D., Thieuleux, F., and Vanbauce, C.: Retrieval of aerosol microphysical and optical properties above liquid clouds from POLDER/PARASOL polarization measurements, Atmos. Meas. Tech., 6, 991–1016, doi:10.5194/amt-6-991-2013, 2013.
Wolke, R., Schroeder, W., Schroedner, R., Renner, E.: Influence of grid resolution and meteorological forcing on simulated European air quality: a sensitivity study with the modeling system COSMO-MUSCAT, Atmos. Environ., 53, 110–130, 2012.
Yue, X., Liao, H., Wang, H. J., Li, S. L., and Tang, J. P.: Role of sea surface temperature responses in simulation of the climatic effect of mineral dust aerosol, Atmos. Chem. Phys., 11, 6049–6062, doi:10.5194/acp-11-6049-2011, 2011.
Zakey, A. S., Solmon, F., and Giorgi, F.: Implementation and testing of a desert dust module in a regional climate model, Atmos. Chem. Phys., 6, 4687–4704, doi:10.5194/acp-6-4687-2006, 2006.
Zakey, A. S., Giorgi, F., and Bi, X.: Modeling of sea salt in a regional climate model: fluxes and radiative forcing, J. Geophys. Res., 113, D14221, doi:10.1029/2007JD009209, 2008.

ACPD
15, 19615–19727, 2015

Zanis, P., Ntogras, C., Zakey, A., Pytharoulis, I., and Karacostas, T.: Regional climate feedback of anthropogenic aerosols over Europe using RegCM3, Clim. Res., V52, 267–278, doi:10.3354/cr01070, 2012.

ACPD
15, 19615–19727, 2015

Table 1. List of the Instrumentations deployed over the two super-sites (Ersa and Lampedusa) during the SOP-1a experiment for the characterization of physical, chemical and optical properties of aerosols, vertical profiles, columnar-averaged properties and radiation measurements. Meteorological parameters and gases concentrations are not included in this Table.

	Ersa		Lampedusa	
	Instruments	Frequency	Instruments	Frequency
Number concentration	1 CPC (0.01–3 µm)	continuous (1')	1W-CPC (0.01–3 µm)	continuous (2')
CCN concentration	1 CCN counter	continuous	1 CCN counter	continuous
Mass concentration	1 $PM_{2.5}$	continuous	1 PM_{40} (TEOM)	continuous
	1 PM_{10}	continuous		
Number size distribution	1 OPC (0.3–5 µm)	continuous	2 GRIMM (0.25–32 µm)	continuous
	1 APS (TSI)	continuous	1 APS (TSI) (0.5–20 µm)	continuous
	1 SMPS (3–300 nm)	continuous	2 (dry/ambient) SMPS	continuous
Mass size distribution	2 Impactor DEKATI (13 stages)	48 h	2 Impactor DEKATI (13 stages)	48 h
			1 Impactor Nano-MOUDI	24 h
PM_1 composition	1 PILS	continuous	AMS (Aerodyne)	continuous
			1 PILS	continuous
PM_{10} composition			1 FAI Hydra Sampler	12 h
Mass BC concentration	1 (7λ) aethalometer	continuous	1 PSAP continuous	(1 h)
			1 MAAP	continuous
Vertical Profiles	1 (1λ 350 nm) Leosphere	continuous	1 (1λ) Leosphere ALS 300	continuous (20')
			2 (3-l) ENEA/Univ. of Rome lidar	continuous (1')
			microwave radiometer (p, T, RH)	continuous (15')
			radiosondes	on event
Scattering coefficient	1 (3λ) TSI nephelometer (450–550-700 nm)	continuous (1')	1 (3λ) TSI nephelometer (450–550-700 nm)	continuous (1')
Absorbing coefficient	1 (7λ) aethalometer (370–420-490–520-660–880-950 nm)	continuous	1 (7λ) aethalometer (370–420-490–520-660–880-95 nm)	continuous
Extinction coefficient	1 (1λ) (860 nm) PAX	continuous (1')		
Column optical properties	1 (9λ) AERONET/PHOTONS	continuous (15' for AOD)	1 (9-λ) AERONET/PHOTONS	continuous (15' for AOD)
			2 (12-l) MFRSRs	continuous (15 s)
Mineral Aerosol Deposition	1 CARAGA	continuous (7 days)	1 CARAGA	continuous (7 days)
Downward shortwave irradiance	1 pyranometer	continuous (30 s)	1 (CMP 21) pyranometer	continuous (30 s)
Downward longwave irradiance	1 pyrgeometer	continuous (30 s)	1 (CGR4) pyrgeometer	continuous (30 s)
Downward window (8–14 µm) irradiance			1 modified CG3 pyrgeometer	continuous (60 s)
Direct Solar radiance			1 CHP1 Pyrheliometer	continuous (30 s)
Direct spectral solar radiation			1 PMOD Precision SpectroRad.	continuous (30 s)
Spectral downward global solar irradiance			1 HyperOCR spectrometer	continuous (30 s)
Spectral downward diffuse solar irradiance			1 HyperOCR spectrometer	continuous (30 s)
Spectral direct solar irradiance			1 spectroradiometer	continuous (60 s)
Downward spectral actinic flux			1 Diode array spectrometer	continuous (60 s)

ACPD
15, 19615–19727, 2015

Table 2. List of the long-term AERONET/PHOTONS sun-photometer stations operated in the western Mediterranean during the ChArMEx/ADRIMED (SOP-1a) experiment.

AERONET/PHOTONS Site Name	Latitude (°N)	Longitude (°E)	Altitude (m)	Nbr of observation days (level 2)	Site characteristics
Modena (MOD)	44.63	10.94	56	1300	Urban
Avignon (AVI)	43.93	4.87	32	3017	Rural
Villefranche-sur-Mer (VSM)	43.68	7.33	130	1538	Peri-urban coastal
Toulon (TLN)	43.13	6.00	50	1580	Urban coastal
Ersa (ERS)	43.00	9.35	80	869	Remote island
Rome Tor Vergata (ROM)	41.84	12.65	130	2236	Peri-urban
Barcelone (BCN)	41.38	2.17	125	1855	Urban near coastal
IMAA-Potenza (POT)	40.60	15.72	820	1076	Urban
Lecce University (LEC)	40.33	18.11	30	1791	Peri-urban coastal
Oristano (ORI)	39.91	8.5	10	934	Peri-urb. coastal
Burjassot (BUR)	39.50	−0.42	30	1102	Urban near coastal
Messina (MES)	38.20	15.57	15	958	Urban coastal
Granada(GRA)	37.16	−3.6	680	1493	Urban
Malaga (MAL)	36.71	−4.47	40	830	Peri-urban
Blida (BLI)	36.50	2.88	230	1645	Rural coastal
Lampedusa (LMP)	35.51	12.63	45	1217	Remote Island

ACPD
15, 19615–19727, 2015

Table 3. In-situ instrumentation deployed onboard the ATR-42 during the SOP-1a experiment.

Parameter measured	Instrument	Abreviation	Location in the aircraft	Wavelength (nm)	Nominal size range (µm)
Size distribution	Forward Scattering Spectrometer Probe, Model 300, Particle Measuring Systems	FSSP-300	wing-mounted	632.8	0.28–20
	Ultra High Sensitivity Aerosol Spectrometer, Droplet Measument Technologies	UHSAS	wing-mounted	1054	0.04–1
	Sky-Optical Particle Counter, Model 1.129, Grimm Technik	GRIMM1	AVIRAD inlet	655	0.25–32
	Optical Particle Counter, Model 1.109, Grimm Technik aerosol inlet	GRIMM2	Communautary	655	0.25–32
	Optical Particle Counter, Model 1.109, Grimm Technik	GRIMM3	Communautary aerosol inlet	655	0.25–32
	Scanning mobility particle sizer, custom-built (Villani et al., 2007)	SMPS	Communautary aerosol inlet	NA	0.03–0.4
Integrated number concentration	Condensation Particle Counters, Model 3075, TSI	CPC	AVIRAD inlet	NA	> 0.005
Scattering coefficient	3λ Integrated Nephelometer, Model 3563, TSI	Nephelometer	AVIRAD inlet	450, 550, 700	NA
Absorption coefficient	3λ Particle Soot Absorption Photometer, Radiance Research	PSAP	Communautray aerosol inlet	467, 530, 660	NA
Extinction coefficient	Cavity Attenuated Phase Shift, Aerodyne Research Inc.	CAPS	Communautary Aerosol inlet	530	NA
	Photomètre Léger Aéroporté pour la Surveillance des Masses d'Air	PLASMA	roof-mounted	340–2250	NA
Chemical composition	Filter sampling	NA	AVIRAD inlet	NA	NA
	Single particle soot photometer, Droplet Measurement Technologies	SP2	Communautary aerosol inlet	1064	0.08–0.5

ACPD
15, 19615–19727, 2015

Table 4. Characteristics of the 15 sounding balloons flights from Sant Lluis, Minorca Island, during the ChArMEx SOP1a/ADRIMED campaign.

No.	Date (2013)	Start time (UTC)	Ceiling altitude (m)	Latitude at ceiling	Longitude at ceiling	Sensors
BLD1	12 Jun	21:13	21 178	39.5156° N	04.3010° E	T, U
BLD2	15 Jun	21:40	32 119	39.9903° N	04.1801° E	T, U, LOAC, O_3
BLD3	16 Jun	10:29	31 880	40.0527° N	04.1524° E	T, U, LOAC, O_3
BLD4	16 Jun	21:13	33 390	40.0999° N	04.0118° E	T, U, LOAC, O_3
BLD5	17 Jun	10:01	32 744	40.2109° N	03.9672° E	T, U, LOAC, O_3
BLD6	17 Jun	18:25	33 411	40.2502° N	03.9402° E	T, U, LOAC, O_3
BLD7	18 Jun	16:34	35 635	40.5832° N	04.0515° E	T, U, LOAC
BLD8	18 Jun	21:17	21 507	40.6372° N	04.4889° E	T, U, LOAC, O_3
BLD9	19 Jun	10:12	30 902	40.6794° N	04.3691° E	T, U, LOAC, O_3
BLD10	19 Jun	13:48	36 129	40.6553° N	04.1970° E	T, U, LOAC
BLD11	27 Jun	09:43	35 832	39.7546° N	04.4746° E	T, U, LOAC
BLD12	28 Jun	05:36	36 293	39.4505° N	04.1709° E	T, U, LOAC
BLD13	29/30 Jun	23:31	36 310	39.6168° N	03.7383° E	T, U, LOAC
BLD14	30 Jun	14:03	36 319	39.8937° N	03.9568° E	T, U, LOAC
BLD15	02 Jul	10:27	32 833	39.9942° N	04.2996° E	T, U, LOAC, O_3

ACPD
15, 19615–19727, 2015

Table 5. Characteristics of the 14 BPCL drifting balloon flights.

Date and time of launch (UT)	Balloon Nbr and type of sensor	Last data time (UT)	Last data location	Trajectory length (km)	Flight duration (h)	Approximate float altitude (m)
16 Jun, 09:46	B74, LOAC	16 Jun, 21:51	43.0265° N 05.2285° E	368	11:57	2100
16 Jun, 09:53	B53, O3	17 Jun, 00:26	40.6541° N 06.2398° E	203	14:28	3000–3050
16 Jun, 09:58	B70, LOA	16 Jun, 23:01	40.1825° N 06.1293° E	174	13:17	3050–3150
17 Jun, 09:27	B54, O3	17 Jun, 16:49	43.1433° N 03.5293° E	371	07:22	1850–2000
17 Jun, 09:29	B75, LOAC	17 Jun, 16:51	43.0868° N 03.6866° E	365	07:23	1950–2050
17 Jun, 11:07	B72, LOAC	17 Jun, 19:07	43.2333° N 04.7403° E	382	08:03	2750
19 Jun, 10:34	B77, LOAC	19 Jun, 17:59	43.1576° N 04.7562° E	387	07:37	2550
19 Jun, 10:35	B71, LOAC	19 Jun, 15:03	43.0560° N 05.1336° E	369	04:39	3250–3350
27 Jun, 10:00	B80, LOAC	28 Jun, 12:07	37.9165° N 12.1605° E	759	26:19	2950–3050
28 Jun, 05:20	B73, LOAC	28 Jun, 17:24	37.4095° N 09.2346° E	523	12:16	2650–2750
02 Jul, 13:03	B76, LOAC	03 Jul, 09:38	37.8897° N 12.1312° E	731	20:39	3150–3250
02 Jul, 13:11	B57, O3	03 Jul, 22:43	35.0900° N 14.1140° E	1053	33:44	3100–3200
02 Jul, 17:59	B55, O3	04 Jul, 02:20	37.3545° N 12.21980E	762	32.32	2400–2450
02 Jul, 17:50	B78, LOAC	04 Jul, 02:13	37.5639° N 12.1507° E	755	32.25	2350–2450

ACPD
15, 19615–19727, 2015

Table 6. Main aerosol volume size distribution characteristics: r_{vf} (µm), σ_f, r_{vc} (µm), σ_c, C_{vf}, C_{vc}, for the four different AERONET/PHOTONS stations: Ersa, Lampedusa, Cagliari and Cap d'En Font. C_{vi} denotes the particle volume concentration, r_{vi} is the median radius, and σ_i is the standard deviation. Each average value in the table is accompanied by its standard deviation (this is not an accuracy of the retrieval).

	Ersa	Lampedusa	Cagliari	Cap d'En Font
Number of observations	33	18	20	20
r_{vf} (µm)	0.16 ± 0.02	0.14 ± 0.01	0.15 ± 0.03	0.17 ± 0.03
σ_f	0.43 ± 0.03	0.50 ± 0.06	0.46 ± 0.04	0.45 ± 0.04
r_{vc} (µm)	2.49 ± 0.43	2.36 ± 0.48	2.52 ± 0.28	2.48 ± 0.30
σ_c	0.69 ± 0.03	0.68 ± 0.05	0.71 ± 0.04	0.71 ± 0.04
C_{vf} ($\mu m^3\,\mu m^{-2}$)	0.02 ± 0.01	0.02 ± 0.01	0.02 ± 0.01	0.02 ± 0.01
C_{vc} ($\mu m^3\,\mu m^{-2}$)	0.03 ± 0.01	0.08 ± 0.05	0.05 ± 0.03	0.04 ± 0.03

ACPD
15, 19615–19727, 2015

Table 7. Averaged mean Single Scattering Albedo (SSA) estimated from the AERONET/PHOTONS network at four stations during the SOP-1a, at 440, 670, 870 and 1020 nm.

	Ersa	Lampedusa	Cagliari	Cap d'En Font
Number of observations	33	18	20	20
440/970/870/1020	0.977/0.970/0.965/0.964	0.916/0.922/0.925/0.929	0.927/0.915/0.914/0.916	0.957/0.951/0.948/0.948

ACPD
15, 19615–19727, 2015

Table 8. Main characteristics (period of simulations, horizontal resolution, number of vertical layers, main aerosol (primary and/or secondary) species, radiative transfer codes) of the four different 3-D models used during the SOP-1a experiment (see Sect. 6) (GME is for the global model of the German Weather Service).

Models	Time of simulation	Horizontal resolution	Number of vertical layers	Aerosol species	Layer Forcing	Radiative transfer code
CHIMERE	01 Jun–31 Jul	50 km	20	Dust, Sea Salt, Secondary organic and inorganic, primary OC-BC	WRF	FastJX
CNRM-RCSM	01 Jun–31 Jul	50 km	31	Dust, Sea-Salt, Sulphates, primary OC-BC	ERA-Interim	SW: FMR (6 bands, Morcrette et al., 1989) LW: RRTM (Mlawer et al., 1997)
RegCM	13 Jun–05 Jul	25 km	23	Dust, Sea-Salt, Secondary inorganic, primary OC-BC	NCEP reanalysis	CCM3 or RRTM
COSMO-MUSCAT	15 May–31 Jul	28 km	40	Dust	GME	Ritter and Geleyn (1992)

ACPD
15, 19615–19727, 2015

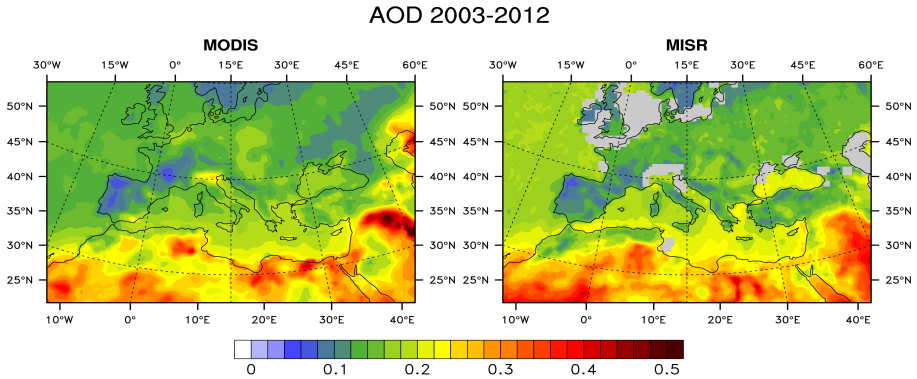

Figure 1. Aerosol Optical Depth (at 550 nm) derived from MODIS and MISR satellites for the 2003 to 2012 period.

ACPD
15, 19615–19727, 2015

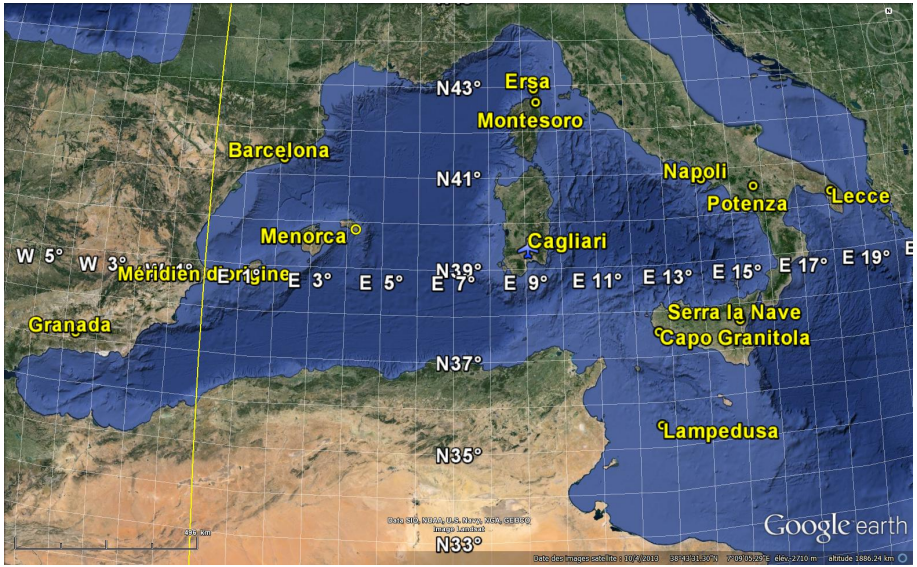

Figure 2. The regional experimental set-up deployed in the western and central Mediterranean during the campaign ChArMEx SOP-1a. The two aircraft were based at Cagliari.

ACPD
15, 19615–19727, 2015

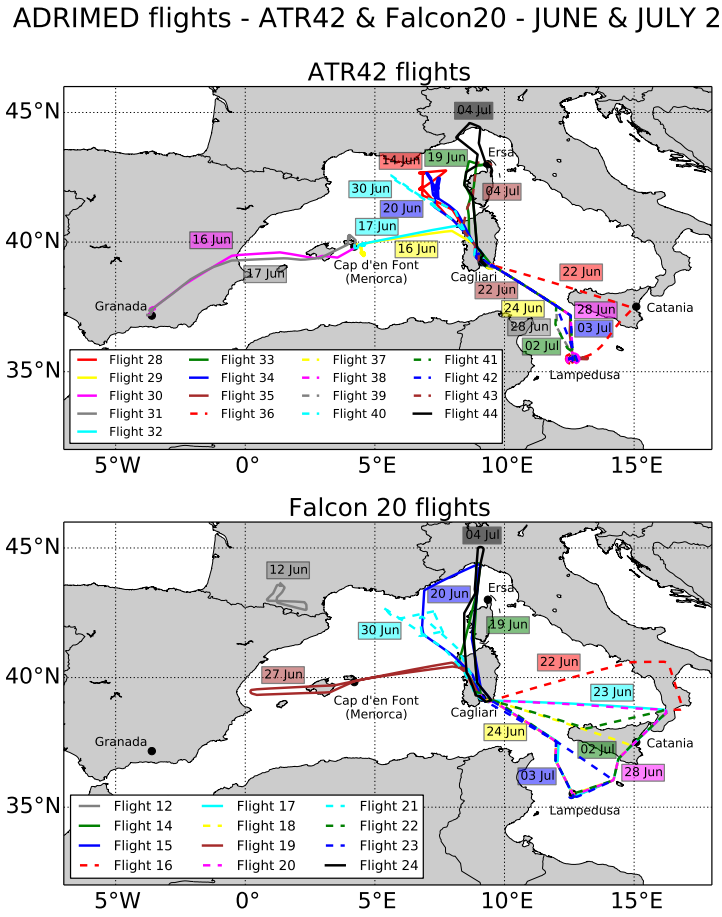

Figure 3. Overview of the different ATR-42 and F-20 flights trajectories performed during the SOP-1a experiment.

ACPD
15, 19615–19727, 2015

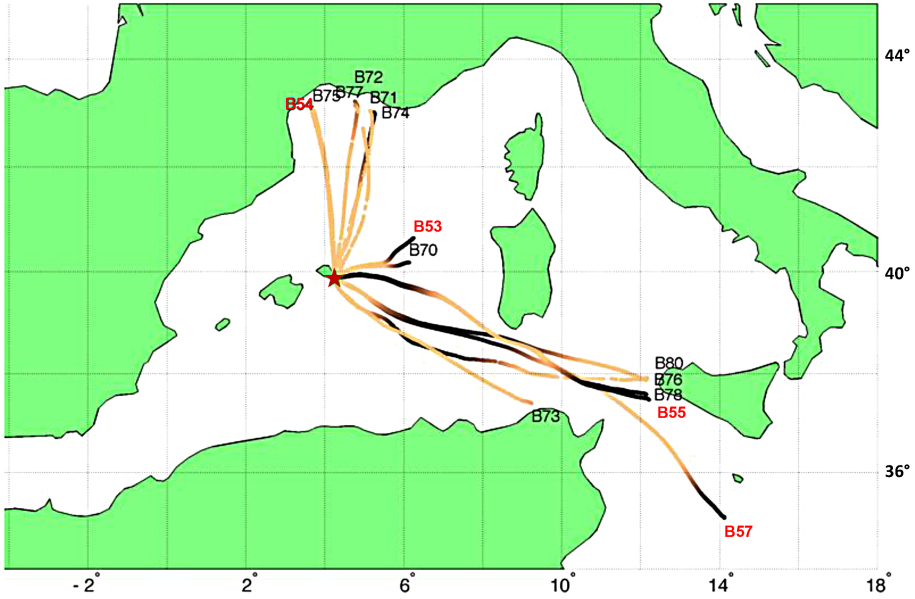

Figure 4. Trajectories of the 14 BPCL drifting balloons launched from Minorca Island during the campaign. Dark portion along trajectories correspond to night-time conditions. The four red labels from B54 to B57 indicate balloons with an ozone sonde and the 10 others carried a LOAC instrument.

ACPD
15, 19615–19727, 2015

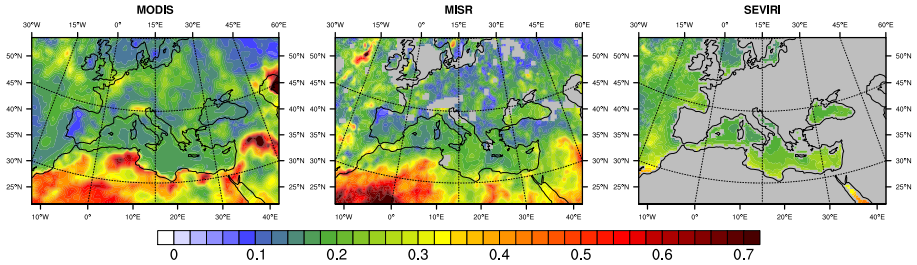

Figure 5. Total AOD (500 nm) obtained from the MODIS, MISR and SEVIRI (sea only) sensors for the June–July 2013 period.

ACPD
15, 19615–19727, 2015

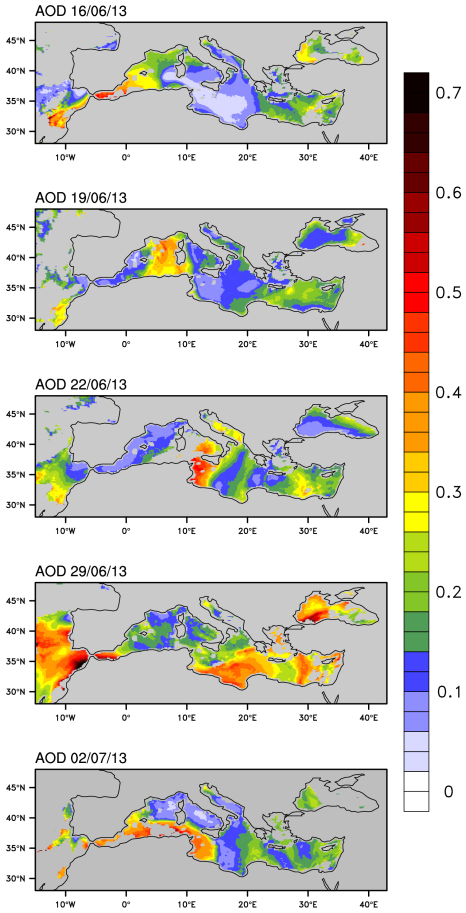

Figure 6. AOD MSG/SEVIRI observations for five different days during the SOP-1a experiment (16, 19, 22, 29 June and 3 July).

ACPD
15, 19615–19727, 2015

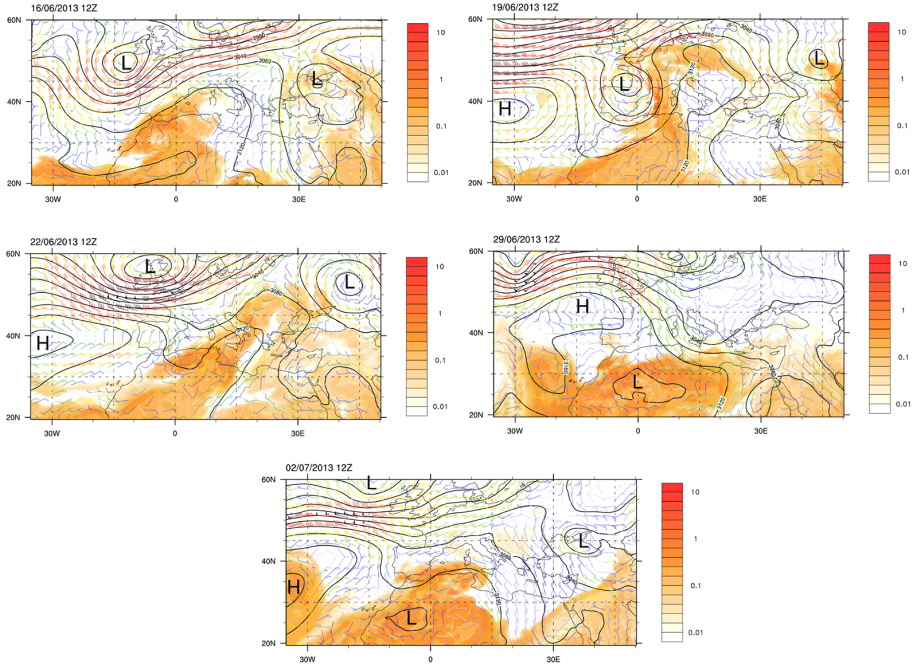

Figure 7. Geopotential at 700 hPa, mass dust concentration (in mg m^{-3}), and wind intensity at 700 hPa for the 6, 19, 22, 29 June and 2 July at 12:00 UTC, simulated from the ALADIN model.

ACPD
15, 19615–19727, 2015

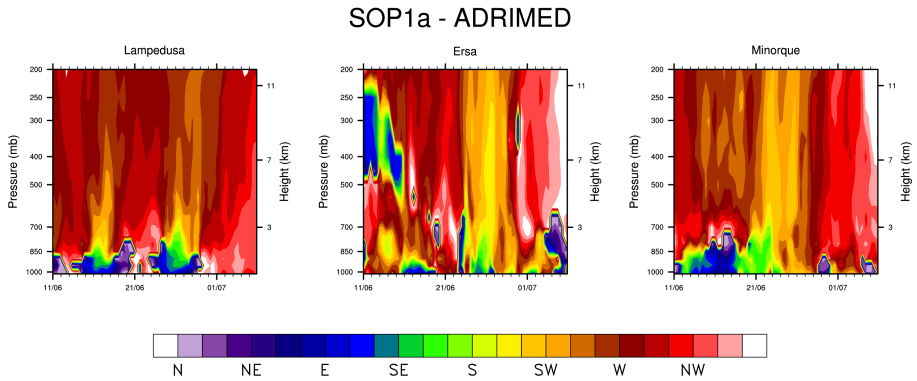

Figure 8. Wind profiles between 1000 and 200 hPa during the SOP-1a experiment for three different sites (Ersa, Lampedusa and Minorca) simulated from the ALADIN model.

ACPD
15, 19615–19727, 2015

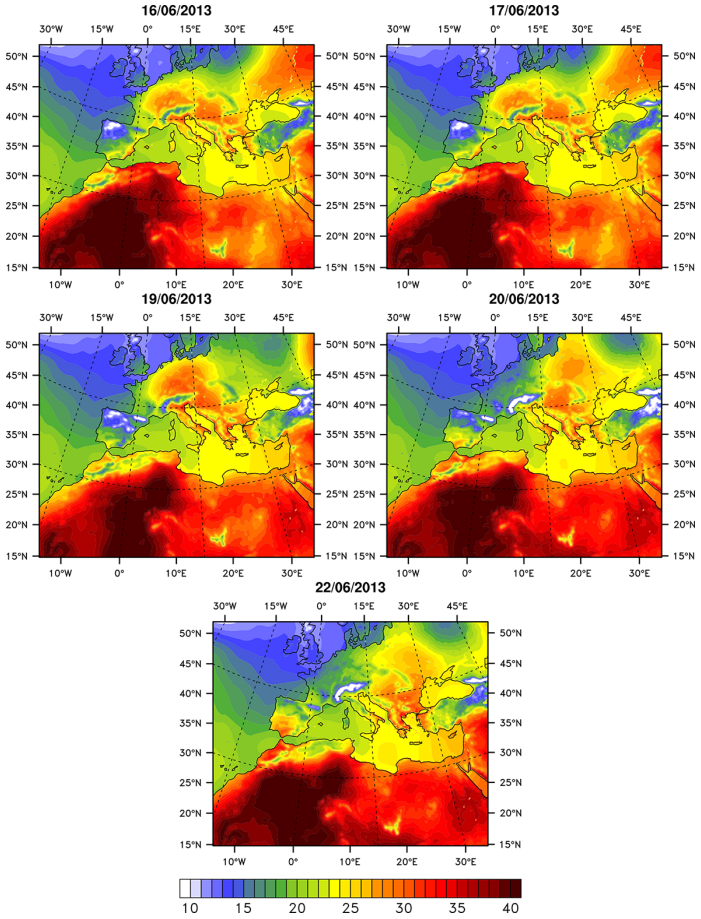

Figure 9. Surface Temperature (at 12:00 UTC) obtained from NCEP re-analysis for the 16, 17, 19, 20 and 22 June.

ACPD
15, 19615–19727, 2015

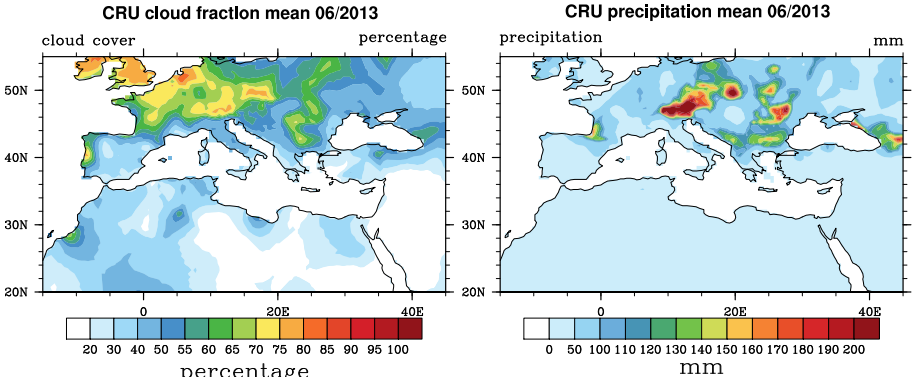

Figure 10. Monthly cloud cover and precipitation (over land only) derived from the Climate Research Unit (CRU) data for June 2013.

ACPD
15, 19615–19727, 2015

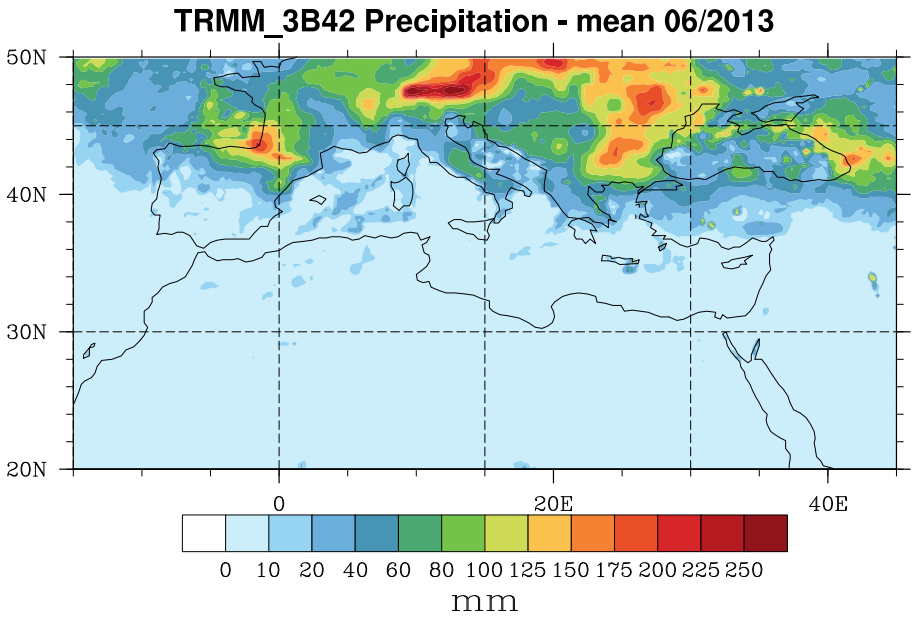

Figure 11. Same figure as 10 but for the Tropical Rainfall Measuring Mission (TRMM) precipitation observations.

ACPD
15, 19615–19727, 2015

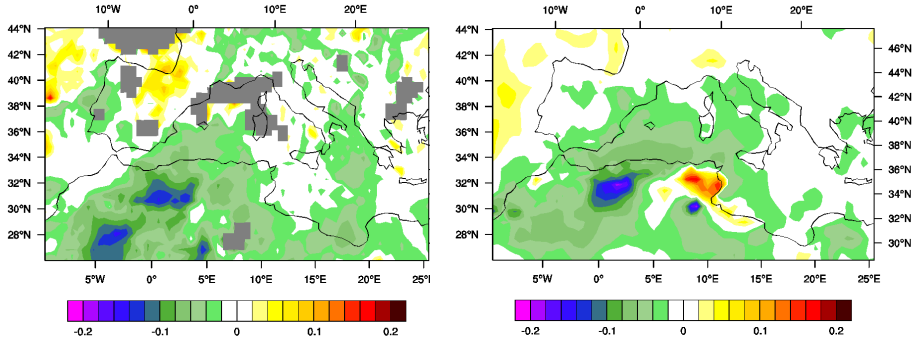

MISR observations MODIS observations

Figure 12. AOD anomaly for summer 2013 estimated from the MODIS and MISR sensor data.

ACPD
15, 19615–19727, 2015

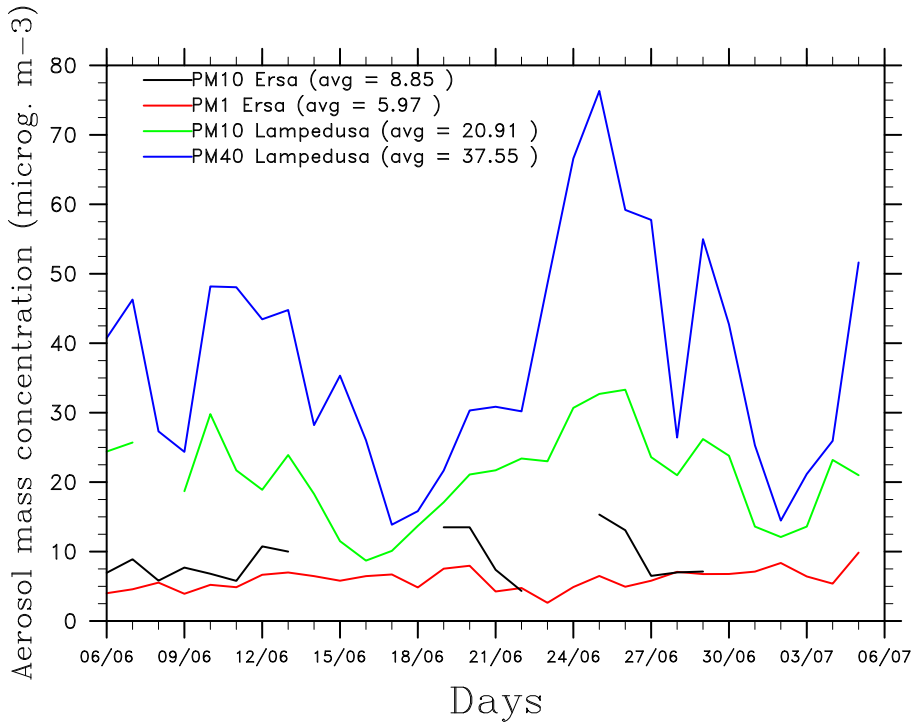

Figure 13. Time-series of daily PM mass concentrations estimated at the Lampedusa (PM_{40} and PM_{10}) and Ersa (PM_1 and PM_{10}) super-stations.

ACPD
15, 19615–19727, 2015

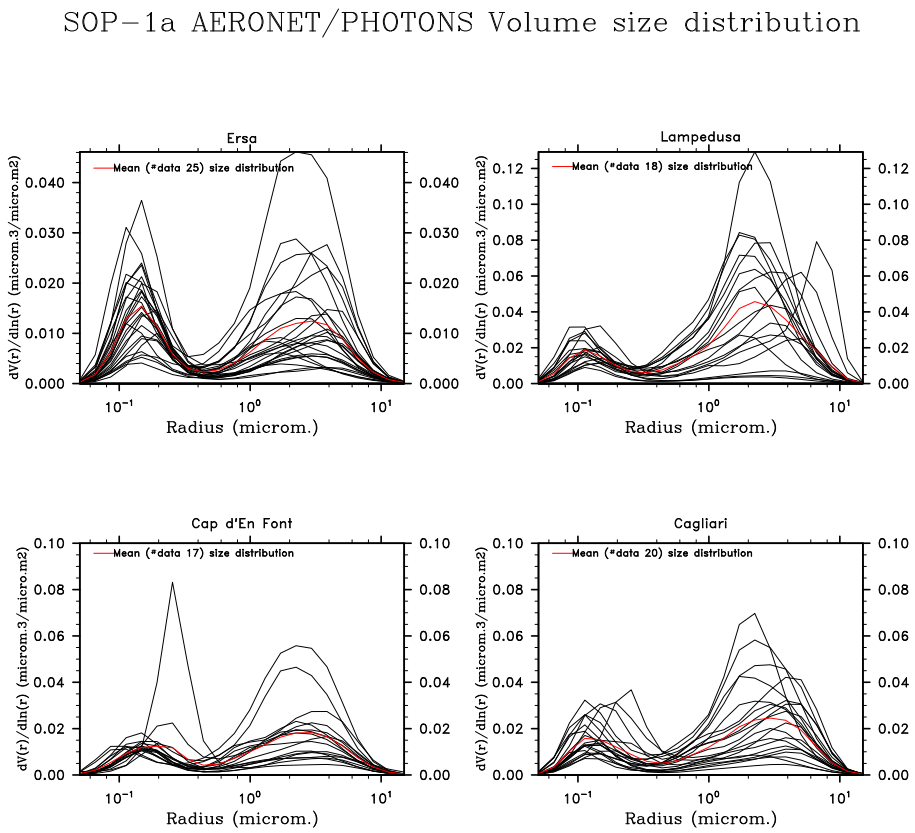

Figure 14. AERONET/PHOTONS volume size distribution derived at four different stations: Ersa, Lampedusa, Cagliari and Cap d'En Font (the red curve represents the mean of observations). The characteristics of the volume size distribution are provided in Table 6.

ACPD
15, 19615–19727, 2015

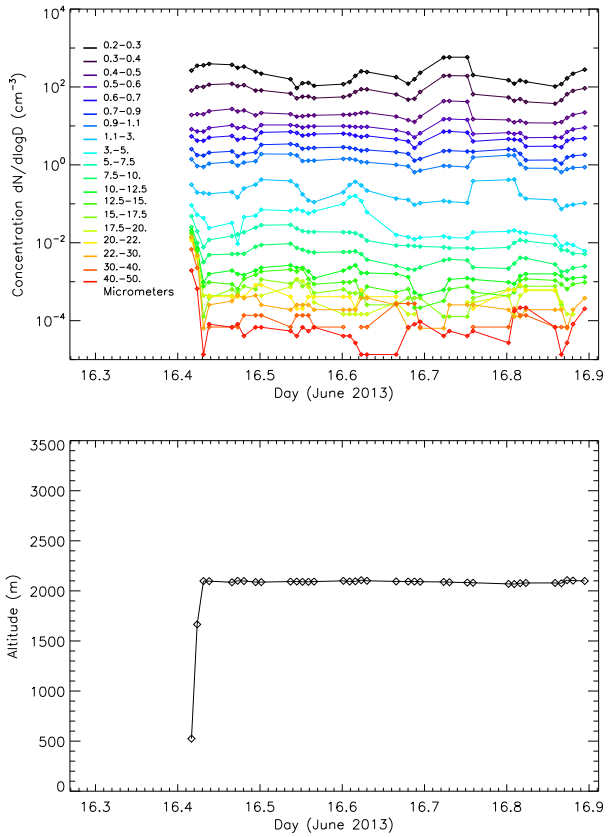

Figure 15. Particle size distribution measured with a LOAC during the ~ 12 h flight of the BPCL balloon B74 drifting from Minorca Island towards Marseille (see trajectory in Fig. 4). The first and last 20 min correspond to the ascending and descending phases of the quasi-Lagrangian flight which occurred at a constant altitude of 2091 ± 10 m.

ACPD
15, 19615–19727, 2015

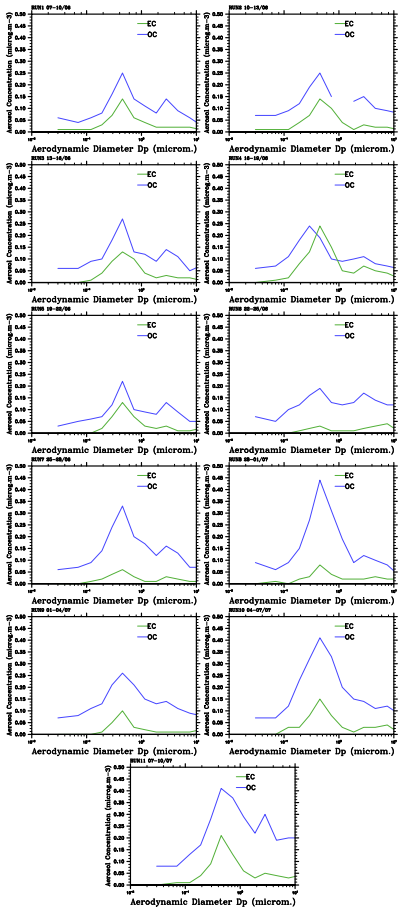

Figure 16. EC and OC (48 h-mean) aerosol mass size distributions obtained at Ersa from the impactor DEKATI instrument for all the SOP-1a period.

ACPD
15, 19615–19727, 2015

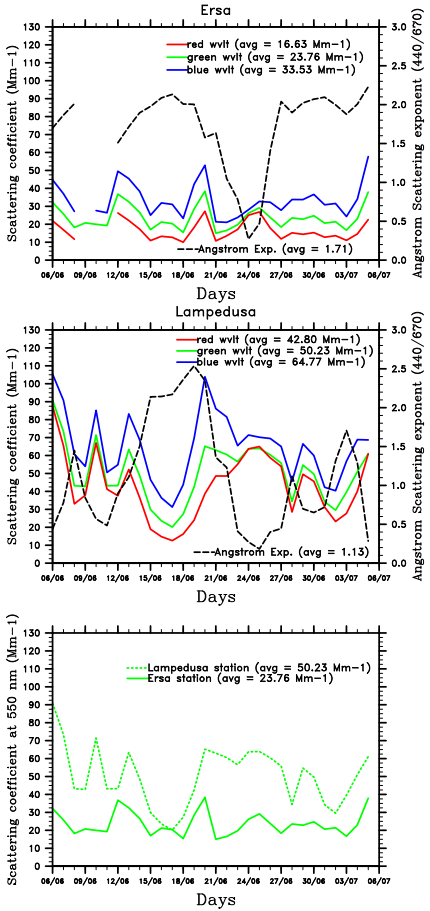

Figure 17. Time-series of daily scattering coefficient (in Mm^{-1}) estimated in the Ersa and Lampedusa stations. The daily Angström Exponent (AE), calculated between 440 and 670 nm, is also reported.

ACPD
15, 19615–19727, 2015

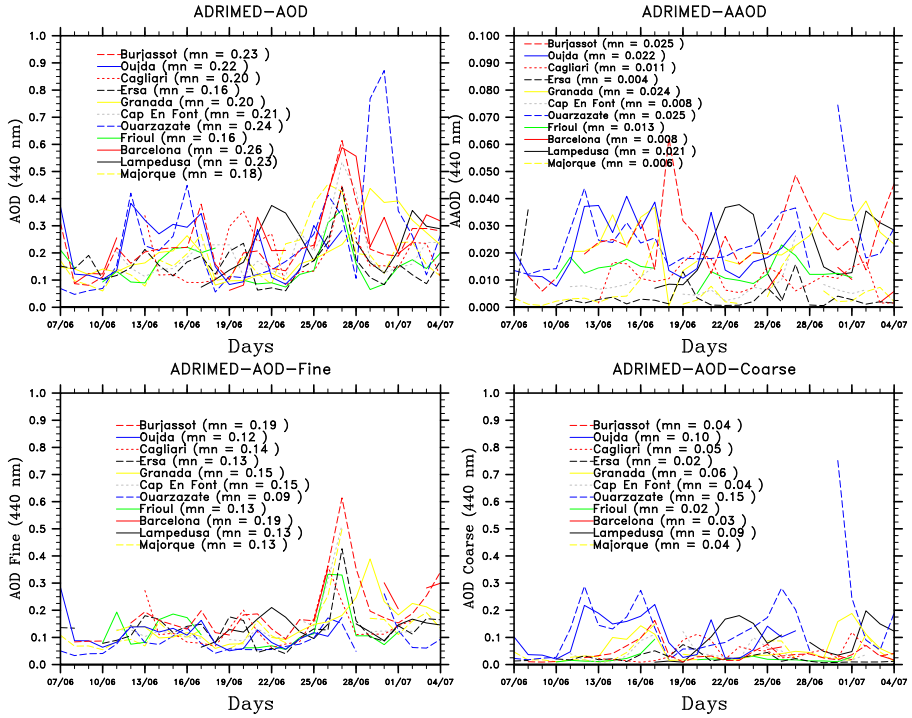

Figure 18. AERONET/PHOTONS observations of the total extinction AOD, AOD Fine (AODf), AOD Coarse (AODc) and Absorbing AOD (AAOD), at 440 nm obtained for the whole SOP-1a period.

ACPD
15, 19615–19727, 2015

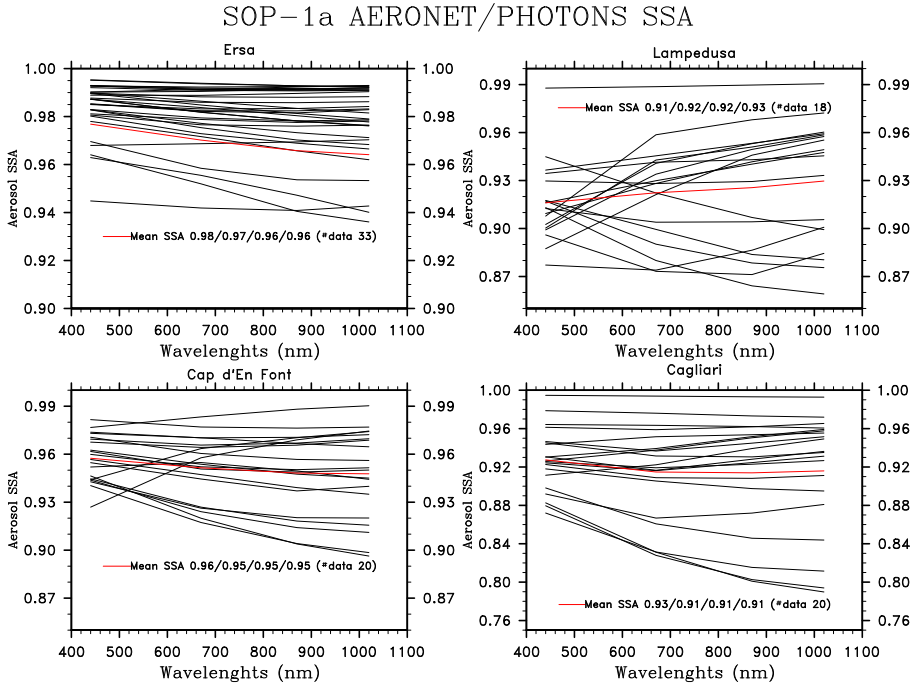

Figure 19. AERONET/PHOTONS observations of the total single scattering albedo (SSA) at 440, 670, 880 and 1020 nm obtained for the whole SOP-1a period (the red curve represents the mean of observations).

ACPD
15, 19615–19727, 2015

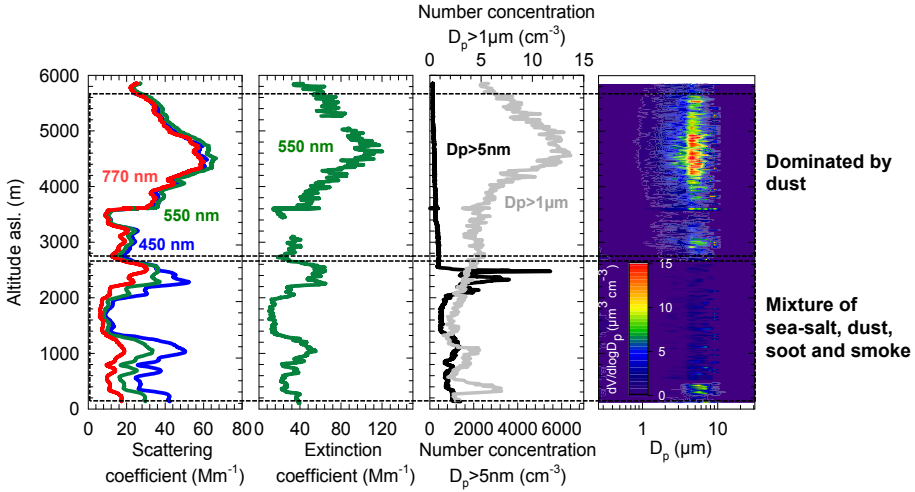

Figure 20. Optical (scattering and extinction coefficients) and physical (number concentration and volume size distribution) aerosol properties estimated along the vertical onboard the ATR-42 aircraft for the flights 35–36 on 22 June over the Lampedusa station.

ACPD
15, 19615–19727, 2015

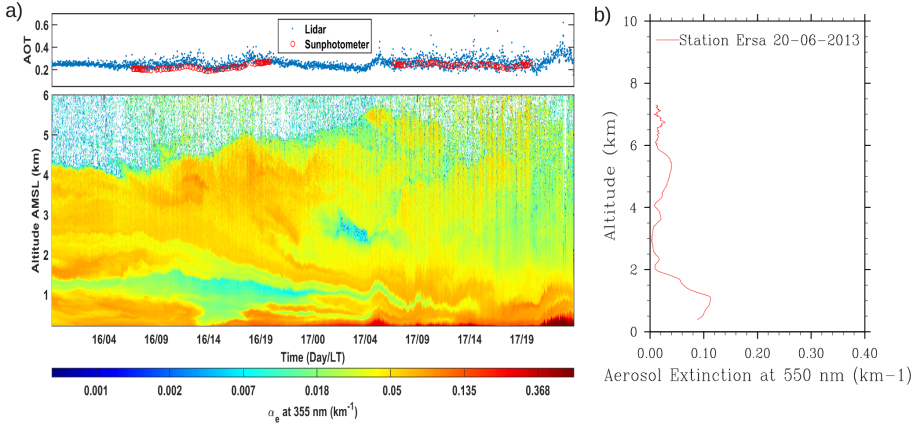

Figure 21. Minorca and Ersa lidar observations obtained during the dust plume of 16 to 17 June transported over the western Mediterranean basin.

ACPD
15, 19615–19727, 2015

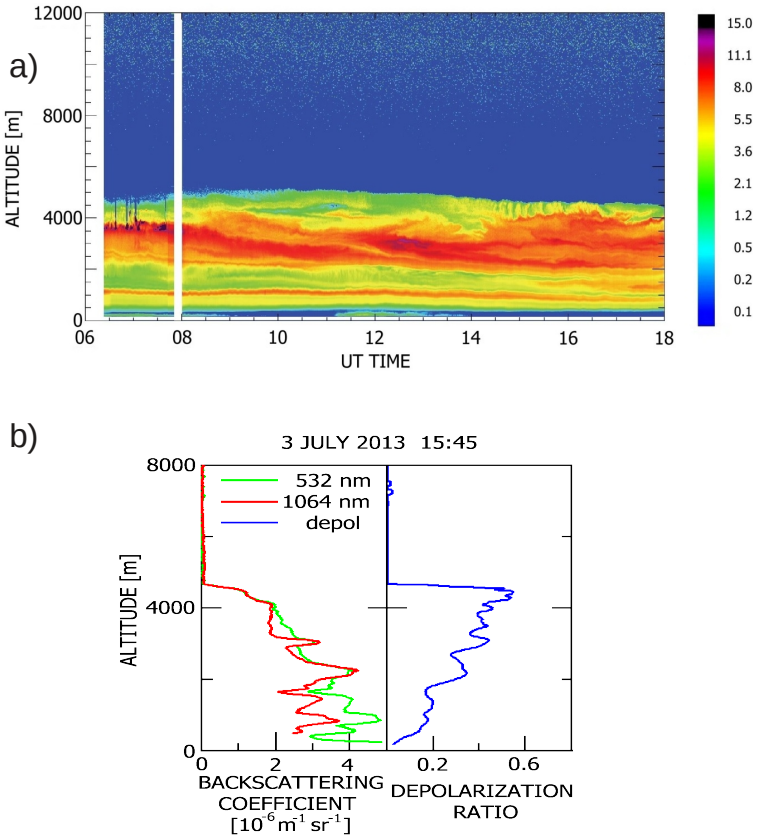

Figure 22. (a) Time evolution of the vertical profile of the aerosol backscattering coefficient at 1064 nm at Lampedusa on 3 July 2013. The color scale is in units of 10–7 m^{-1} sr^{-1}. **(b)** Vertical profile of aerosol backscattering coefficient at two wavelengths and of aerosol depolarization ratio at 355 nm measured at Lampedusa on 3 July 2013 at 15:45 UT.

ACPD
15, 19615–19727, 2015

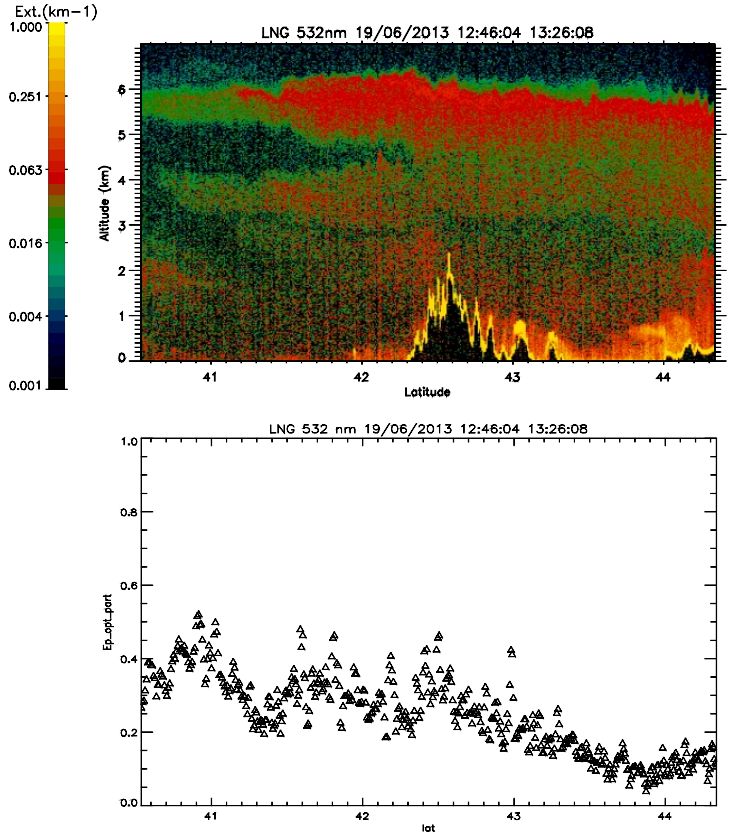

Figure 23. Observations of aerosol extinction coefficient (top, in km^{-1} at 532 nm) and aerosol optical depth (bottom) obtained from the lidar LNG system onboard the F-20 aircraft during the 19 June that corresponds to the flight (12:46 to 13:26) from Cagliari to the Gulf of Genoa.

ACPD
15, 19615–19727, 2015

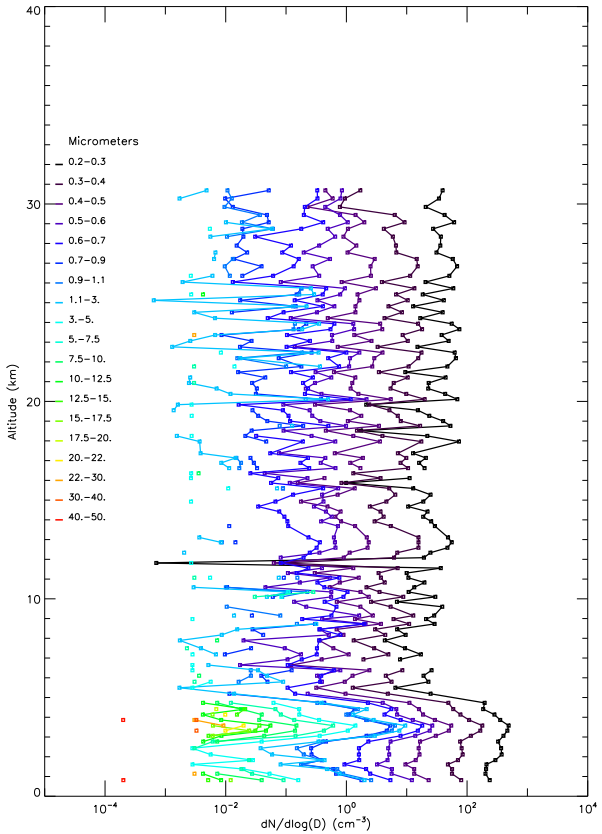

Figure 24. Particle concentrations as a function of size and altitude in the troposphere and lower stratosphere from the LOAC flight under the meteorological balloon BLD9 launched from Minorca at the end of a dust event on 19 June 2013, 10:12 UT (Table 4; see the daytime averaged aerosol optical depth over the sea in Fig. 6).

ACPD
15, 19615–19727, 2015

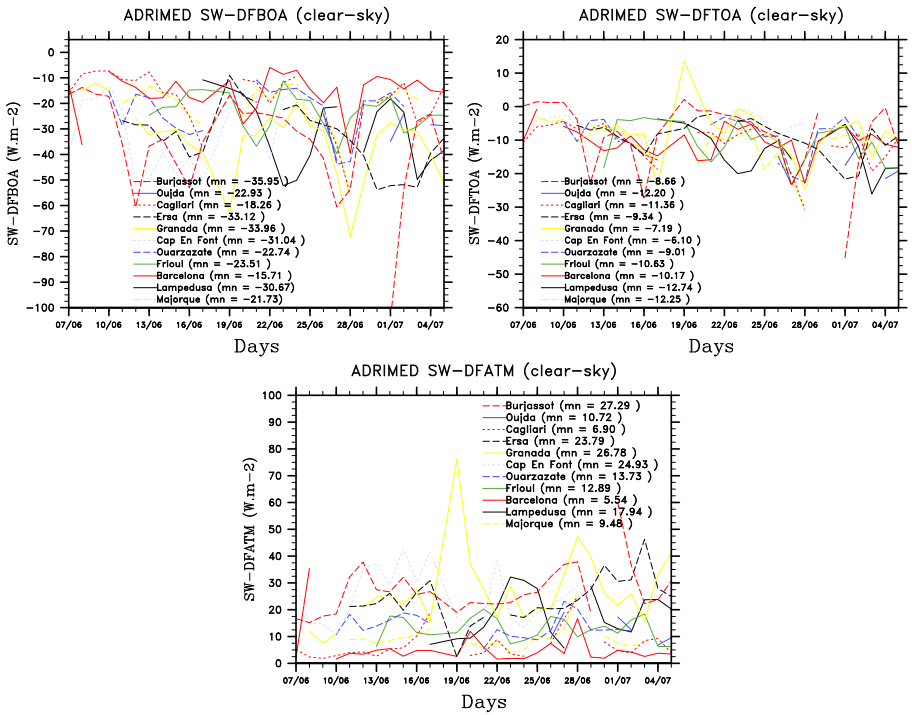

Figure 25. 1-D (clear-sky) instantaneous (shortwave only) DRF calculations (in $W\,m^{-2}$) based on AERONET/PHOTONS dataset for the different stations listed in Table 2 (BOA, TOA and ATM refer to bottom of the atmosphere, top of atmopshere and atmospheric forcings).

ACPD
15, 19615–19727, 2015

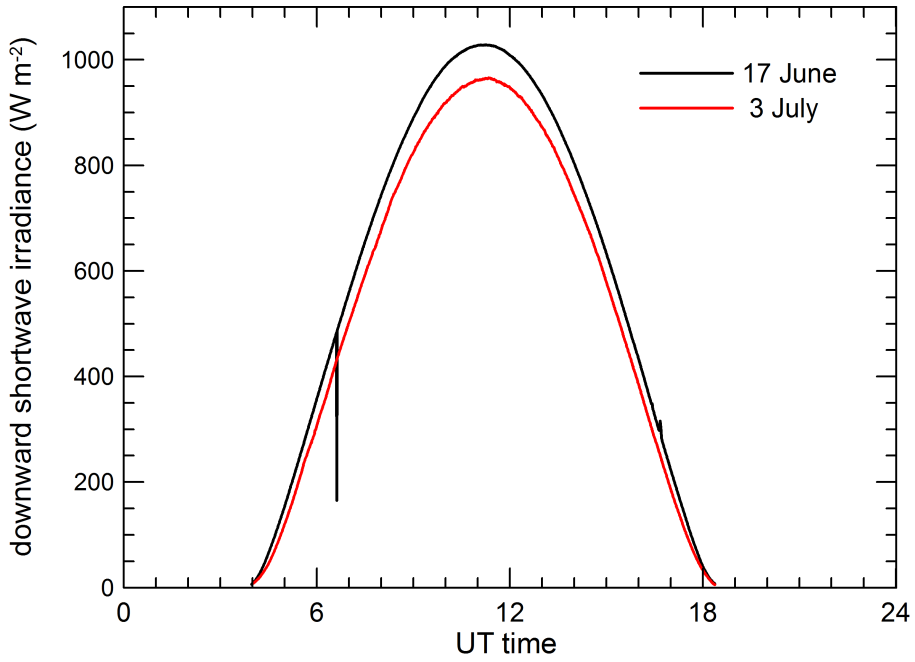

Figure 26. Time evolution of the downward solar irradiance observed at Lampedusa on 17 June and on 3 July 2013.

ACPD
15, 19615–19727, 2015

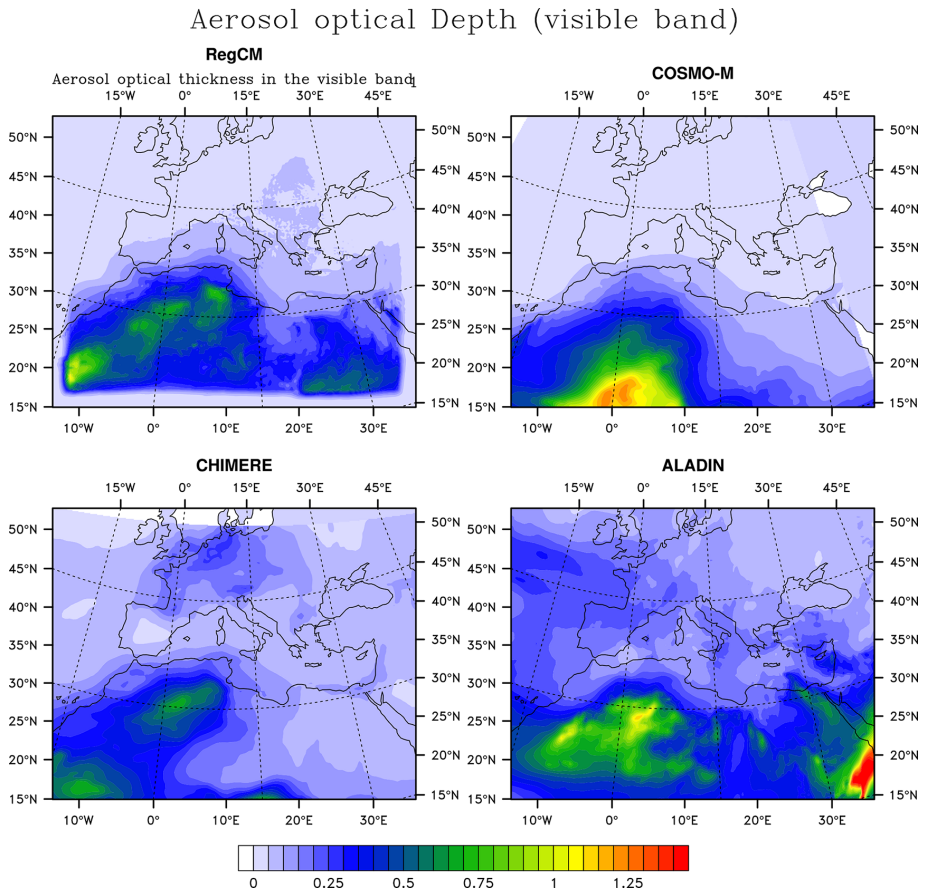

Figure 27. AOD averaged for the 15 to 25 June 2013 period from the meso-scale COSMO-MUSCAT **(a)**, CTM-CHIMERE **(b)** models and the two regional climate models; CNRM-RCSM **(c)** and RegCM **(d)**. Details about the model configurations are provided in Table 8.

ACPD
15, 19615–19727, 2015

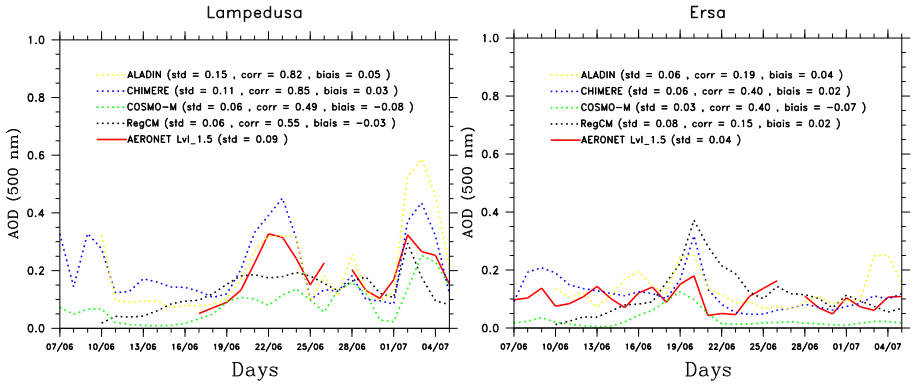

Figure 28. Times-series of AOD comparisons between AERONET/PHOTONS observations and COSMO-MUSCAT, CHIMERE, CNRM-RCSM and RegCM model ouputs over the two stations of Ersa and Lampedusa.

ACPD
15, 19615–19727, 2015

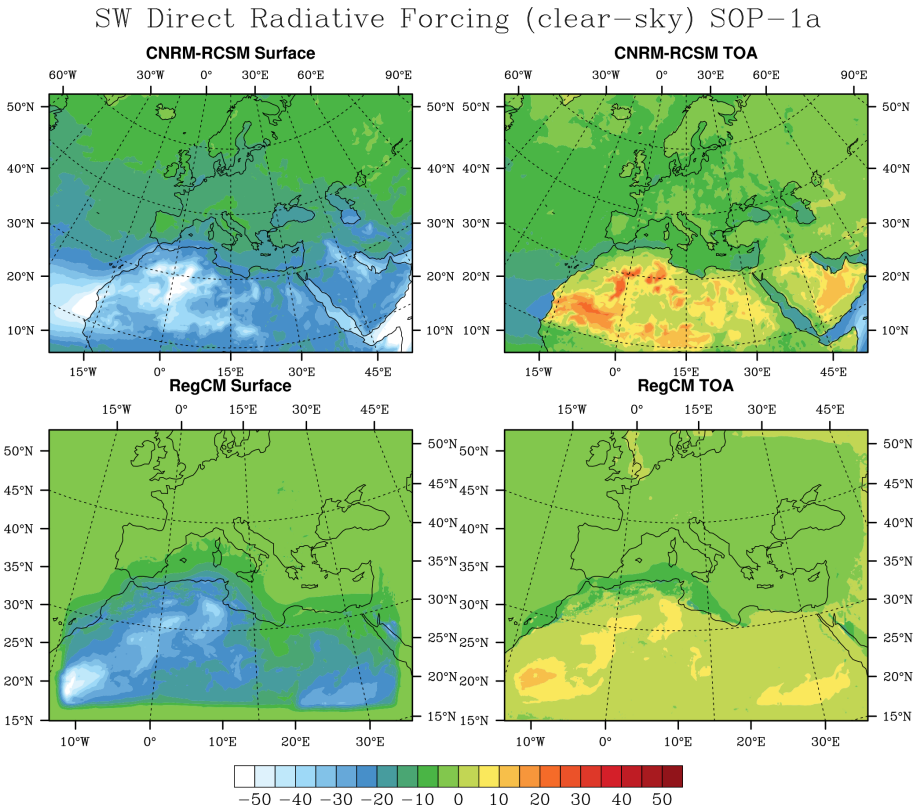

Figure 29. Averaged surface and TOA SW DRF simulated in clear-sky conditions and over the SOP-1a period by the CNRM-RCSM and RegCM models.

ACPD
15, 19615–19727, 2015